Summer 6-2014

PbS QUANTUM DOT-BASED HETROJUNCTION SOLAR CELLS

Sawsan Khader Dagher

Recommended Citation

Dagher, Sawsan Khader, "PbS QUANTUM DOT-BASED HETROJUNCTION SOLAR CELLS" (2014). *Dissertations*. 27.
https://scholarworks.uaeu.ac.ae/all_dissertations/27

United Arab Emirates University

College Of Engineering

PbS QUANTUM DOT-BASED HETROJUNCTION SOLAR CELLS

Sawsan Khader Dagher

This dissertation is submitted in partial fulfillment of the requirements for the Degree of Doctor of Philosophy

Under the direction of Professor Yousef Haik

June 2014

DECLARATION OF ORIGINAL WORK

I, Sawsan Khader Dagher, the undersigned, a graduate student at the United Arab Emirates University (UAEU) and the author of the dissertation titled “PbS Quantum Dot-Based Hetrojunction Solar Cells”, hereby solemnly declare that this dissertation is an original work done and prepared by me under the guidance of Professor Yousef Haik, in the College of Engineering at UAEU. This work has not been previously formed as the basis for the award of any degree, diploma or similar title at this or any other university. The materials borrowed from other sources and included in my dissertation have been properly acknowledged.

Student’s Signature……………………………… Date…………………………

PhD Examining Committee:

1) Advisor (Committee chair): Prof. Yousef Haik

Title: Professor

Department: Mechanical Engineering

Institution: UAEU

Signature……………………………………Date………………………………

2) Member: Prof. Nacir Tit

Title: Professor

Department: Physics

Institution: UAEU

Signature……………………………….….Date……………..……………..

3) Member: Dr. Ahmad Ayesh

Title: Associate Professor

Department: Physics

Institution: UAEU

Signature……………………………….….Date……………..……………..

4) External Examiner: Prof. Mohamed Henini

Title: Professor

Department: Physics & Astronomy

Institution: University of Nottingham

Signature……………………………….….Date……………..……………..

Accepted by

Dean of the College……………………………………………………......…..........

Signature………………………………… Date……………..……………....

Dean of the College of Graduate Studies…………………………………….…………

Signature………………………………… Date……………..……...........

ABSTRACT

This study investigates the influence of nanoparticles (NPs) size on their optical properties, and the effect of combination of lead sulfide (PbS) quantum dots (QDs), with n-type and p-type NPs, on the photogenerated charge carriers transport across the heterojunction solar cell structure. PbS QDs, of a range of sizes, were synthesized using a co-precipitation process. In this study, p-type NPs, which are poly [3,4-ethylenedioxythiophene] –poly [styrenesulfonate] (PEDOT: PSS), copper oxide (CuO) and graphene oxide (GO); and n-type NPs which are zinc oxide (ZnO), titanium dioxide (TiO_2), cadmium sulfide (CdS) and bismuth sulfide (Bi_2S_3), were synthesized and characterized by SEM and UV-visible spectrophotometers. The NPs with enhanced optical properties were utilized in heterojunction solar cell structures via spin coating, chemical bath deposition and SILAR cycle methods.

The morphology and the theoretical band energy diagram for each cell were examined. The photovoltaic performance of the cells was measured in the dark and under 1 sun illumination (irradiation of 100 mW/cm^2). This yielded cells with efficiencies from 0.388% up to 5.04%. The solar cell with FTO/ZnO/TiO_2/CdS/PbS/PEDOT:PSS/Au structure and optimum layers' thickness exhibited a short-circuit current of 24.2 mA/cm^2, an open circuit voltage of 544 mV, a fill factor of 38.2 % and a power conversion efficiency of 5.04% with good stability. This is related to the uniform surface morphology throughout every cell layer without voids, pinholes or cracks. Furthermore, the gradual band energy levels alignment of n-type and p-type QDs (CdS/PbS), as well as the high hole

mobility of PEDOT:PSS and the high electron affinity of ZnO and TiO_2 are other contributory factors influencing efficiency enhancement.

ملخص

هدفت هذه الدراسة الى بناء خلايا شمسية باستخدام الجسيمات النانوية. تم فحص تأثير حجم الجسيمات النانوية على خصائصها البصرية، وتأثير مزيج من جسيمات نانوية مكونة من أشباه موصلات سالبة وأخرى موجبة، مع جسيمات كبريتيد الرصاص النانوية (PbS)، على نقل الشحنات عبر بنية الخلية الشمسية. في هذه الدراسة، الجسيمات النانوية المكونة من أشباه الموصلات السالبة هي : بوليمر موصل (PEDOT:PSS)، أكسيد النحاس (CuO)، و أكسيد الجرافين (GO). و أشباه الموصلات الموجبة هي: أكسيد الزنك (ZnO)، ثاني أكسيد التيتانيوم (TiO_2)، كبريتيد الكادميوم (CdS)، وكبريتيد البزموث (Bi_2S_3). تم تجهيزها مخبريا باستخدام عدة طرق كيميائية، و فحص خصائصها الضوئية بالاضافة الى حجم وشكل الجسيمات، باستخدام المجهرالإلكتروني الماسح و مقياس الطيف الضوئي.

الجسيمات النانوية ذات الخصائص الضوئية المحسنة، استخدمت في بناء عدة تراكيب من الخلايا الشمسية. تم قياس أداء كل من الخلايا الشمسية في الظلام وتحت الإضاءة بواسطة جهاز محاكاة الشمس (1كيلو واط/متر^2). حققت هذه الخلايا كفاءات من 0.388٪ إلى 5.04٪. الخلية الشمسية ذات التركيب: FTO /ZnO /TiO_2 /CdS /PbS /PEDOT:PSS /Au أعطت أفضل النتائج مع استقرار جيد؛ نتج عنها جهد دائرة مفتوحة قيمته 544 فولت، كثافة تيار دائرة مغلقة قداره 24.2 ميلي أمبير/سم^2، و كفاءة تحويل طاقة مقدارها 5.04٪. يعود تحسن الفعالية في هذه الخلية الى تجانس السطح في جميع طبقات الخلية، دون وجود فراغات ، ثقوب أو شقوق. وكذلك التوافق في مستويات الطاقة للمواد المستخدمة في بناء طبقات الخلية.

ACKNOWLEDGMENTS

I would like to express my great appreciation to those who contributed directly or indirectly to my dissertation during the completion of this study.

I am sincerely grateful to my supervisor Professor Yousef Haik for his continuous support, guidance, encouragement and fruitful discussions throughout this research.

I appreciate the kind coopration and assistance of my co-advisors Professor Nacir Tit and Dr.Ahmad Ayesh whose assistance with theoretical, practical and logistical issues proved invaluable throughout the process of preparing this dissertation.

I would like to thank the technical staff in the laboratories at the Mechanical Engineering Department and the Physics Department for their support on technical issues. I also appreciate the encouragement of all my friends who inspired me throughout my studies.

Finally, I appreciate the support of my family, with special thanks to my husband Khalid for his understanding and unconditional support throughout this research.

DEDICATION

With much appreciation;

I dedicate this dissertation to my parents who have been a source of encouragement and inspiration to me.

I also dedicate this dissertation to my husband who supported me each step of the way.

TABLE OF CONTENTS

LIST OF TABLES

LIST OF FIGURES

LIST OF ABBREVIATIONS

SCs	Solar cells
QDs	Quantum dots
QDSCs	Quantum dot solar cells
QDSSCs	Quantum dot sensitized solar cells
NPs	Nanoparticles
E_g	Bandgap energy
VB	Valance band
CB	Conduction band
SILAR	Successive ionic layer adsorption and reaction.
PV	Photovoltaic
TCE	Transparent conductive electrode
ETL	Electron transport layer
AL	Active layer
HTL	Hole transport layer
ME	Metal electrode
AM	Air mass coefficient
V_{OC}	Open-circuit voltage
J_{SC}	Short-circuit current density
FF	Fill factor

PCE	Power conversion efficiency
ITO	Indium tin oxide
FTO	Fluorine doped tin oxide
DMF	N,N-dimethyl formamide
PEDOT:PSS	Poly[3,4-ethylenedioxythiophene]-poly[styrenesulfonate]
GO	Graphene oxide
OA	Oleic acid
EDT	1,2-ethanedithiol
QC	Quantum confinement
PL	Photoluminescence

CHAPTER ONE

INTRODUCTION

Due to the increasing environmental harm caused by fossil fuels and the economic concerns regarding future stock depletion, there are moves towards encouraging renewable energy of all types. Solar energy is a free, abundant, reliable, sustainable and clean renewable energy source. It involves no environment pollution, especially when compared to fossil fuels. The sun supplies the Earth's surface with about 1.2 x 10^{17} W of solar power. This means that sufficient energy is supplied to satisfy the entire energy demand for a year in less than one hour [1]. Despite intensive research efforts over the past few decades photovoltaic cells remain costly and comparatively inefficient to be considered as a competitive primary energy source. In order to achieve high efficiency and low production costs for solar cells (SCs), several types of SCs have been examined. Of these, four main categories of SCs are currently available:

(i) Multijunction solar cells: These cells are made out of several ultra-thin films grown on top of each other, in which, each pair of layers consists of a solar cell by itself. The ultra-thin films are made of semiconductor materials that are lattice-matched with each other to form multiple p-n junctions. Each material absorbs visible light of a certain range of wavelengths from the solar spectrum. Triple junction SCs, which are based on gallium arsenide (GaAs), achieved the greatest efficiency to date (44%) [2]. Despite of the high efficiency achieved by multijunction SCs, their use is mostly limited to space applications, due to their high material costs and complex structure. Additionally, multijunction SCs onlybecome practical under 400 sun illuminations so light concentrators are required [3].

(ii) Crystalline silicon solar cells: Silicon is the most widespread material used for SCs. Typically silicon-based SCs are divided into three groups: monocrystalline, amorphous and polycrystalline. SCs based on monocrystalline silicon have achieved an efficiency rate of 21% [4], which is considered reliable for terrestrial applications. Nevertheless, they are still considered costly due to the use of high temperatures in the manufacturing process.

(iii) Thin-film solar cells: These are made out of one or more thin layers deposited on a variety of substrates, the thickness of each layer varies from a few nanometers to tens of micrometers. The most efficient semiconductor materials used for thin-film technologies are cadmium telluride (CdTe), copper indium gallium selenide (CIGS) and amorphous silicon (a-Si). Scientists at Empa, the Swiss Federal Laboratories for Materials Science and Technology, developed thin film SCs using CIGS on flixible polymer foils giving an efficiency rate of 20.4%, as of January 2013 [5]. First Solar, Inc. (Nasdaq: FSLR) developed SCs using CdTe with an efficiency rate of 17.0%, as of March 2014 [6]. Thin-film technologies have several advantages over previous SCs' due to a decrease in active material thickness, flexibility and consequently a reduction in cost, however, they still have lower efficiency levels than silicon cells.

(iv) Emerging research: Referred to as the third generation of SCs, these are mainly divided into three categories; dye sensitized solar cells (DSSCs) are made by depositing a thin layer of highly porous titanium dioxide (TiO_2) on top of fluoride-doped tin dioxide (SnO_2:F) coated glass, followed by soaking the film in a dye solution such as ruthenium-polypyridine dye. The molecules of the dye are an active layer that absorbs light, so they are called molecular sensitizers. The other electrode is prepared separately using a conductive material such as platinum. The two films are sealed together after injecting a liquid electrolyte, such as iodide electrolyte, between the films. At present, the highest power conversion efficiency (PCE) achieved by DSSCs is 11.4% [7], and a new record of 12.3% was obtained by the co-sensitization of porphyrin dye YD2-o-C8 and the organic dye Y123 [8]. DSSCs do not need complicated equipment to be manufactured. Not only do they need much lower cost materials, but they can also be synthesized into flexible sheets. On the other hand, the conversion efficiency is less than the best thin film SCs.

The second category of third generation SCs is organic SCs in which the active layer consists of a blend of conjugated polymers such as polyphenylene vinylene as electron donors, and fullerene derivatives such as phenyl-C_{61}-butyric acid methyl ester (PCBM) as electron acceptors. These are sandwiched between two electrodes with proper work functions. The last 5 years have seen major improvement in this technology [9-15]. Konarka Power Plastic recorded an efficiency level of 8.3% which was certified by the NREL (National Renewable Energy Laboratory) in 2011 [15]. To date, the highest reported PCE for an organic SCs is 12% (2013) [14]. Organic SCs can be fabricated on glass and plastic substrates with high processability [16], which makes SCs flexible and lightweight. On the other hand, the efficiency, stability and strength of organic SCs are all low compared to inorganic SCs [17].

The last category of the third generation of SCs is quantum dot solar cells (QDSCs), which are based on nanomaterials, and have been reported as promising for the next generation of SCs. Quantum dots (QDs) can be employed in every type of SC to reduce cost and enhance efficiency. Currently QDs have been integrated into four main types of SCs which are: Schottky SCs [18-29], depleted heterojunction SCs [18-23, 30-37], hybrid organic/inorganic SCs [20, 24, 38-43] and quantum dot sensitized SCs [44-48]. Each type of these QDSCs are discussed in detail in section 2.2.

1.1 Quantum Dots (QDs)

Nanostructure materials have many attractive characteristics compared to bulk materials since their physical, mechanical, electrical and optical properties change fundamentally with variations in the dimensions of their structure from bulk to molecular levels. This leads to entirely new applications, especially in electronics, photonics and biology [49-52]. Nanostructures are classified as; (i) two dimensional, such as thin films, quantum plates or quantum wells, (ii) one dimensional, such as quantum wires or quantum rods, (iii) zero dimensional, such as QDs or nanopartiles (NPs). Recently, attention has been paid to QDs which are three dimensionally confined semiconductor nanocrystals. Figure 1.1 represents schematic diagrams of the density of electronic energy states (DOS) as an energy function for the bulk and also for three main nanostructures. Figure 1.1a shows the number of states at each energy level that can be occupied by electrons, that are continuous for the bulk and become descrete as the size and dimensionality are reduced due to the structure approaching the nanoscale. This is as a result of the quantization of generalized momentum caused by confinement (see Figure 1.1d). As QDs are considered zero dimensional relative to the bulk, they are characterized as having extreme confinement effects near band edges. Consequently, discrete energy levels and an increase in bandgap energy (E_g) is evident as the particle size decreases. E_g is the energy difference between the top of the valence band (VB) and the bottom of the conduction band (CB). The relationship between the E_g and the particle size is shown in Figure 1.2.

Nanoparticles (NPs) have strong quantum confinement effects when their size is small enough to meet one of the following conditions; (i) as one dimension of the nanoparticle approaches the de Broglie wavelength of electrons and holes in the bulk semiconductor (λ_e), (λ_h), respectively; (ii) as the nanoparticle's size approaches or becomes smaller than the exciton Bohr radius (R_B). λ_e, λ_h can be calculated by the following equations [53]:

$$\lambda_e = \frac{h}{\sqrt{m_e * kT}} \qquad (1.1a)$$

$$\lambda_h = \frac{h}{\sqrt{m_h * kT}} \qquad (1.1b)$$

Where, m_e and m_h are the effective masses of the electron and hole, respectively, h is Planck’s constant, k is Boltzmann’s constant and T is the absolute temperature.

For most semiconductors λ_e, λ_h are 10–100 nm. For example, Si λ_e = 24 nm, and PbSe λ_e = 40 nm [53].

The Bohr radius (R_B) is the separation distance of the electron-hole pair in a bulk semiconductor. Electron-hole pairs attracted through the coulomb potential are called excitons. Exciton binding energy for most bulk semiconductors is low, thus electrons and holes interact in a weak manner. Conversely, when the nanoparticle's diameter is smaller than R_B, the energy level spacing of the nanoparticle increases, thus electron and hole pairs are confined and consequently interact even at room temperature. Additionally, exciton-exciton interaction energy is also much larger than in the case of bulk materials [54]. R_B can be calculated in the following equation [55]:

$$R_B = \frac{4\pi\varepsilon h^2}{\mu e^2} \qquad (1.2)$$

Where, ε, h, and e are the optical dielectric constant, Planck's constant and the charge of an electron, respectively. μ is the reduced effective mass of the electron and hole. Typically ranges are between 2–100 nm. For example, R_B is 47 nm for PbSe and 4 nm for Si [53].

QDs are preferred for optoelectronic applications due to the dominance of quantum confinement (QC) effects which result in discrete energy levels [56]. This leads to a delocalization of the charge carrier establishing greater electronic coupling between nanocrystals facilitating the charge transport [57]. The mechanism is due to variable-range hopping. Electrons can hop from one localized site to another when receiving energy from a phonon, which enhances the chances of electrons coupling with higher mobility, and leading to vastly increased conductivity [58]. Furthermore, due to slow carrier relaxation, the electrons stay longer before recombining with the holes that facilitate charge transport and dissociation [59]. QDs allow energy level matching between the desired p-type and n-type materials, which are crucial in designing efficient photovoltaic devices [60], and multiexciton generation [61-66] that can improve light-to-current conversion efficiencies of SCs up to 32% [61]. QDs minimize the thickness of the semiconductor materials needed to absorb light and expand the spectrum by increasing the volume to area ratio [61, 64, 65]. Currently many types of QDs have been theoretically and experimentally studied and their potential applications for SCs have been demonstrated.

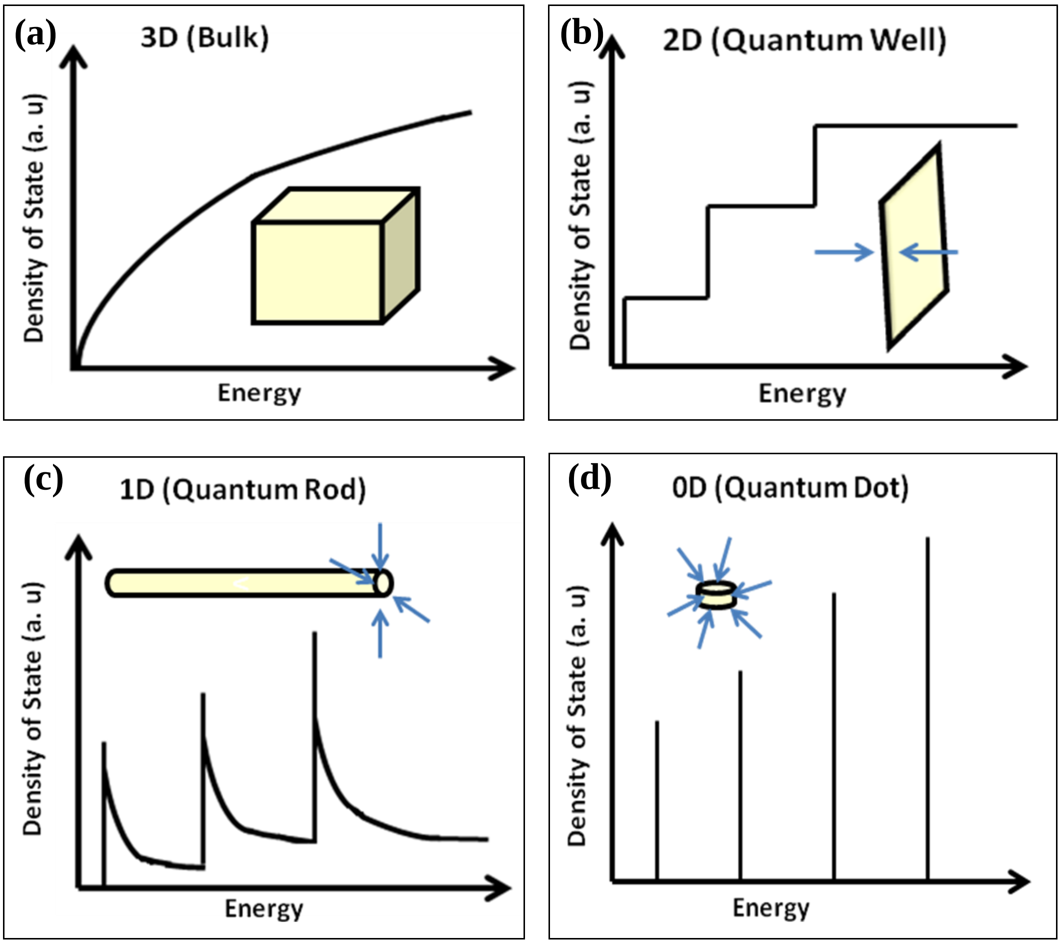

Figure1.1 The density of energy states of structures with different dimensions; (a) bulk materials, (b) quantum wells, (c) quantum rods, (d) quantum dots showing the splitting of energy bands in going from bulk to quantum dots.

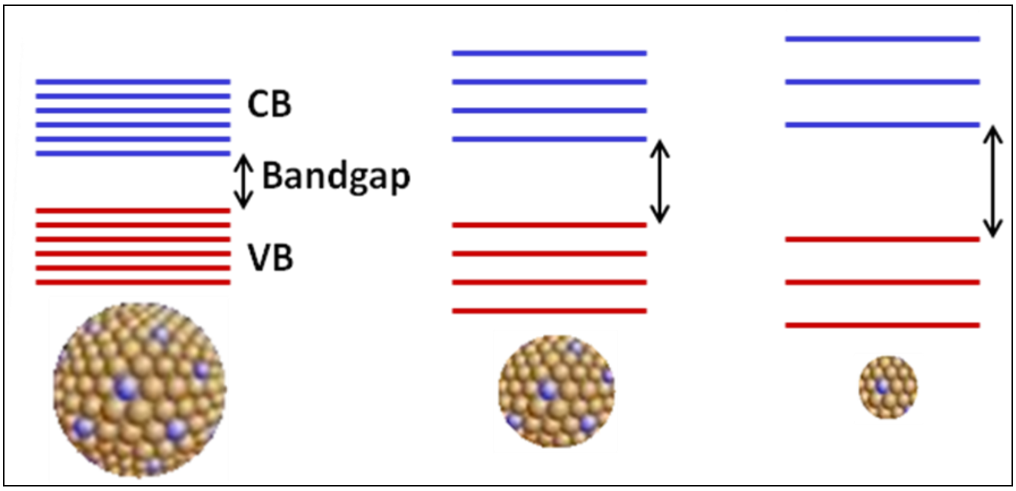

Figure1.2 The relationship between the bandgap and the particle size.

1.2 Objectives

A review of the literature currently available on PbS QDSCs (see section 2.2) shows that absorption of solar photons has to be maximized while maintaining efficient charge extraction at the same time in order to improve the efficiency of QDSCs. As these two parameters have an inverse relationship; enhancement of light absorption requires an increase in the active QDs layer thickness leading to charge recombinations before reaching the separation interface that is due to limited exciton diffusion length (exciton radius and lifetime). Recently, several approaches have been applied to overcome these limitations. Depleted bulk heterojunction QDSCs, based on penetration between p-type and n-type QDs, increases the interfacial area and thus allows for the depletion region tp spread in three dimensions on the active layer. Another approach is using quantum junction solar cells (QJSCs), based on doped PbS QDs, which leads to the gradual decrease in the CB and VB from p to n type materials, thus generating a depletion region for efficient carrier separation and collection. In quantum funnel solar cells (QFSCs) the driving force behind photoelectrons from their point of generation towards the electron acceptor layer is indeed generated by the variation of PbS QDs size. In this study a combination of the concept of depleted heterojunction SCs using wide E_g semiconductors (TiO_2 and ZnO), and an extension of gradual energy level alignment through QJSCs and FJSCs, using n-type and p-type QD active layers (CdS/PbS), as well as the benefits of the high hole mobility of organic semiconductors used as hole transport layers (PEDT: PSS), were investigated to enhance the efficiency of

QDSCs. Furthermore, the two n-type materials (ZnO or TiO_2 (NPs) and CdS (NPs) have not been applied together in any solid (p-n) heterojunction QDSC before, as this structure was mainly used in liquid (p-n) heterojunction QDSCs (QDSSCs). To the best of our knowledge, this kind of SCs structure (ZnO/TiO_2/CdS/ PbS QDs /PEDOT: PSS/Au) has not been previously reported upon.

The overall aim of the research is to contribute to the development of the next generation of nanophotovoltaic devices which will have enhanced conversion efficiency compared to current SCs. This can be achieved by integrating the advantages of several SC types in one solar cell structure. In view of this, the research was undertaken with the following specific objectives:

a. Synthesize a number of n-type and p-type nanoparticles semiconductors with enhanced optical properties for photovoltaic applications.

b. Utilize the synthesized NPs in heterojunction quantum dot solar cell (HJ-QDSC) structures.

c. Study the effect of employing different hole transport layers (HTL) on solar cell performance.

d. Study the effect of employing different electron transport layers (ETL) on solar cell performance.

e. Study the effect of employing different Active layers (AL) on solar cell performance.

f. Study the effect of employing different (AL) thicknesses on solar cell performance.

g. Select the best performing solar cell and investigate its morphology, photovoltaic performance and stability.

1.3 Achievements

a. ZnO, TiO_2, PbS, CdS, Bi_2S_3, and CuO NPs were synthesized with a degree of controllability on the NPs size. Their morphology and optical properties were examined.

b. The NPs with optimum optical and electronic properties were chosen in consideration of their light absorbing qualities and E_g that can match other layers for gradual energy level alignment in every device.

c. Several SCs were prepared and characterized where CuO, reduced GO, and PEDOT: PSS were employed as HTLs. It was found that PEDOT: PSS was the best one for the SC structure as an HTL. The PCE was higher with this configuration.

d. Several SCs were prepared and characterized, where ZnO, TiO_2 and reduced GO were employed as ETLs. It was found that ZnO/TiO_2 together was best in the SC structure as an ETL. The PCE was higher with this configuration.

e. Several SCs were prepared and characterized where PbS combined to CdS or Bi_2S_3 were employed as ALs. It was found that PbS/CdS structure was the best in the SC structure as an AL. The PCE was higher with this configuration. .

f. Several SCs were prepared and characterized where the thickness of PbS and CdS NPs layers were changed by controlling the number of deposit times as they were deposited by spin coating (PbS) and SILAR (CdS). It was found that 6 spin coated repetitions for PbS and 11 SILAR cycles for CdS was the best in the SC structure as an AL, because the PCE was higher.

g. A PCE of 5% was achieved by the cell with structure FTO/ZnO/TiO_2/CdS/PbS/PEDOT:PSS/Au, which was the highest efficiency achieved by HJ-QDSC, based on CdS/PbS with good stability over the testing period (60 days). To the best of our knowledge, the highest efficiency of HJ-QDSC based on CdS/PbS was not more than 3.5%.

1.4 Scope of the Study

The goal of this dissertation is to develop new SCs with significantly increased power conversion efficiency. The main body of the dissertation consists of five chapters. Each chapter is divided mainly into two parts: the first part deals with QDs and the second with QDSCs. Recent developments in categorizing SCs and the features of NPs or QDs for PV applications are introduced in Chapter one. The objectives and findings of the study are summarized at the end of the same chapter.

Chapter two is the literature review. The beginning of chapter two presents several types of QDs which were utilized in the research. Applications such as PV and synthesis methods are shown. In the last part of chapter two, QDSC structures and principles are discussed and basic terms for PV performance are reported. Furthermore, chapter two offers a comprehensive overview of the fast-developing field of QDSCs: several types of QDSCs are covered and the advantages and disadvantages of each configuration are addressed.

Chapter three presents the experimental details for QDSC preparation and characterization. The different methods applied to synthesize and characterize each type of NP are discussed in the first part of chapter three. Whereas the second part of the chapter shows the synthesis process and characterization techniques for several types of heterojunction QDSC where the NP types in the HTL, ETL, or AL are changed and the effects on cell performance of changing the thickness of the AL are elaborated upon.

Chapter four presents the results and discussion. The first part of chapter four shows the characterization of several synthesizd NPs and shows their size, distribution, morphology and optical properties. It provides an extensive discussion with explanations of the results for each type of synthesized NP. Based upon this comparison, the NPs with enhanced optical properties were chosen to form the SC layers. The second part of the chapter displays cell architecture characterization showing the surface morphology of each layer of the solar cell. The third part shows cell performance characterization and compares the results, as well as providing an explanation for the variation in the performance of one cell structure from another.

Chapter five provides conclusions and recommendations for possible avenues to improve QDSC efficiency in the future.

CHAPTER TWO

RECENT DEVELOPMENTS IN QUANTUM DOT SOLAR CELLS

This chapter presents several types of QDs that are utilized in this study for SC synthesis. Their properties and applications, such as photovoltaic uses, are introduced. A comprehensive survey of the fast-developing nature of QDSCs is presented. The structure and principles of several QDSCs are elaborated upon, and the advantages, as well as disadvantages, of each type are discussed.

2.1 Quantum Dots (QDs)

2.1.1 ZnO Nanoparticles

Zinc oxide (ZnO) is one of the most attractive metal oxides since it exhibits multifunctional semiconducting properties that can lead to a wide range of applications. For instance, ZnO has a wurtzite crystal structure with a lack of a symmetrical centre and strong electromechanical coupling that allows for its use in piezoelectric and pyroelectric applications. In addition, it is a non-allergenic, photo-catalytic, chemically stable and antibacterial material [67]. This means it is compatible for biomedical applications and treatment of waste and pollutants via a photodegradation mechanism [68-71].

ZnO has a wide direct bandgap that is transparent to visible light, but opaque to ultraviolet (UV) light. It has a large exciton binding energy of 60 meV that enables the existence of excitonic emissions at room temperature, and it is considered one of the most effective fluorescent materials [72]. In addition, it exhibits high refraction (melting point of 1975ºC) making it suitable for various electrical and optical semiconducting applications [73, 74]. These properties are sensitive to size, composition and the morphology of the particle: for example optical properties can be monitored and improved as the particle size is reduced to the nanoscale as a result of the increasing surface/volume ratio and quantum confinement (QC) effects [75]. An additional advantage of ZnO NPs is that they possess a therapeutic function that can be utilized for targeting drug delivery and bioimaging during the delivery process. Recently, ZnO NPs were encapsulated with a biocompatible polymer and have shown long term fluorescence stability in order to carry tumour targeted drugs and deliver them to subcellular locations [76, 77]. The diversity of applications for ZnO NPs demonstrates the importance of studying their size dependent optical properties.

Native defects in semiconductors can play important roles in either reducing the quality of electronic and optical properties (like DX centers) [78] or enhancing them (like dopants) [79-81]. For instance, our recent findings present evidence of the importance of structural defects in a system like graphenes, which is aimed at gas sensing applications [82]. Of course, the correlation between growth conditions and properties can help to avoid undesired defects and move towards introducing more desired effects. In this study structural defects in ZnO nanoparticles will be shown to enhance optical properties by reducing the bandgap and allowing electronic transitions with photonic emissions of energy within a visible range. More specifically, it is well established that the most predominant structural defects in ZnO NPs are zinc interstitials (Zn_i) and oxygen vacancies (V_O), as their formation energies are relatively small. Numerous investigations agree that Zn_i, V_O and zinc antisites (Zn_O) result in inducing donor states, whereas oxygen interstitials (O_i), zinc vacancies (V_{Zn}) and oxygen antisites (O_{Zn}) result in inducing acceptor states [79]. More recently, Xu, et al [83] reported a combination of experimental and theoretical investigations on the electronic and optical properties of point defects in ZnO nanopillars. Basically, they inspected three main native defects: zinc interstitial 'Zn_i', oxygen vacancy 'V_O' and oxygen interstitial 'O_i' using photoluminescence and theoretically using a CASTEP code: based on density functional theory. They confirmed that Zn_i yields violet emissions, V_O causes green emissions and O_i is the source of yellow emissions.

As far as the yellow emissions are concerned, there is a general agreement between the experimental data [83, 84] and ab initio calculations [83, 85]. This likely originates from two possible sources: the presence of $Zn(OH)_2$ on the surface of the NPs [84] and the electronic transition from conduction band to O_i level [83-85]. Both arevdensity functional theory based and based on pseudo potentials with scissors corrections [83]. Full potential linear muffin-tin orbital [85] methods have shown evidence that previous defects induce deep acceptor states in the gap allowing for the electronic transitions of energy (2.16–2.28 eV) with yellow emissions. Nonetheless, the existence of defects and their densities is very much dependent on formation energy and the method of synthesis. One of the focuses of the present work is to envisage which among these defects are likely to exist in the composition of the ZnO NPs, via inspecting their optical properties. ZnO NPs can be synthesized using various chemical methods such as the wet chemical method, which is commonly used because of its simplicity and low temperature (< 90 º C). ZnO NPs are grown in an alcoholic medium through the reaction of zinc salt, for instance $Zn(NO_3)_2$, $Zn(CH_3COO)_2.2H_2O$, $ZnSO_4$, etc. with a base such as LiOH, KNO_3, K_2SO_4, NH_4OH, $LiNO_3$, NaOH, etc. [75, 86-91].

2.1.2 TiO_2 Nanoparticles

Titanium dioxide (TiO_2) has many attractive chemical, physical, electronic and optical properties which make it suitable for several applications. It is a low cost metal oxide, chemically stable, non-toxic and environmentaly friendly [92, 93], TiO_2 is a naturally n-type semiconducting material due to stoichiometric oxygen deficiency in the film structure; the bulk TiO_2 has a wide direct bandgap, typically 3.2 eV [94], a high refractive index (n) of 2.6, a high dielectric constant and good transmittance in the visible region since it absorbs UV light due to its large bandgap. These extraordinary characteristics allow the use of TiO_2 in a wide range of applications such as; biomaterials [95], pigments [96], photocatalysts [97], gas sensors [98], capacitors or as a gate dielectric in metal-dielectric semiconductor devices. In addition there are many photovoltaic applications, especially in dye sensitized SCs, owing to their good transmittance in the visible region, high refractive index and chemical stability,

The increased surface area and pore volumes result in higher efficiency in photovoltaic applications than in the bulk TiO_2. A variety of methods have been used to synthesize TiO_2 nanostructures, such as spin coating processes [99], the sol gel template method [100], metal organic chemical vapor deposition

(MOCVD) [101], anodic oxidative hydrolysis [102], sonochemical synthesis [103], inverse microemulsion methods [104], efficient molten salt-assisted pyrolysis routes [105] and hydrothermal methods [106]. $TiCl_4$ has often been utilized as a precursor for the preparation of TiO_2 NPs [107-112]. Calcinations or hydrothermal treatments are normally used to improve the crystallinity of the powders. In this study, TiO_2 NPs were prepared on a substrate using $TiCl_4$. Various transition metals were loaded on the TiO_2 surface to enhance the photoelectronic properties of the devices.

ZnO and TiO_2 have similar physical properties and energy band structures, nevertheless ZnO is still preferred as a buffer layer for heterojunction SCs rather than TiO_2, since it has a higher electron affinity than TiO_2 and it has 2–3 times greater electron mobility than TiO_2 [113]. It can also be utilized for all sizes of PbS QDs. Whereas TiO_2 is appropriate for PbS QDs diameters below approximately 4.3 nm to allow for the efficient transfer of electrons from the conduction band the conduction band of TiO_2 [114], as the electron affinity between small sizes of PbS QDs and TiO_2 is reduced.

2.1.3 PbS Quantum Dots (QDs)

Lead sulfide (PbS), one of the lead chalcogenides, has extraordinary optical properties that can be utilized for several applications in photodetection [115], light-emitting diodes, optical switches [116] and solar cells [24, 117]. PbS is a *p*-type semiconductor and has a cubic crystal structure, narrow direct band gap energy (0.41 eV, for bulk at room temperature), a large exciton Bohr radius (18 nm) [118-121], a high absorption coefficient, excellent photosensitivity in the near-infrared (NIR) region, multiple exciton generation processes and solution processability [61, 63, 122-126].

To date, many methods have been developed to fabricate PbS NPs. By controlling the size of the PbS NPs a tunable bandgap from the near-infrared to the visible region is obtained [126, 127]. Bakueva, et al. [128] were the first to successfully synthesize stable and monodispersed PbS QDs with diameters of 4 nm ± 1 nm in aqueous solutions using a mixture of thioglycerol (TGL) and dithioglycerol (DTG) as the stabilizing agent. Currently hydrothermal methods and thermal decomposition are used to synthesis PbS QDs [129]. Solution process solar cells based on colloidal PbS QDs have recently demonstrated great promise in both energy conversion efficiency and device stability [130]. Spin coating [131], drop-casting [132], and ink-jet printing [133-135] methods have demonstrated the ability to fabricate many potential device applications.

2.1.4 Ligand Exchange

A ligand is an ion or molecule (functional group) that binds to a central metal atom to form a coordination complex. The bonding between metal and ligand generally involves a formal donation of one or more of the ligand's electron pairs. The nature of metal-ligand bonding can range from covalent to ionic. Ligands are used to facilitate the synthesis of NPs and allow fine control over their size and dispersity. The native coordinating organic ligand chemically coats the surface of the nonocrystals and thus has a significant role in transporting the charge between the NPs [136, 137], and it affects their optical and electrical properties, due to the large surface-to-volume ratio of these NPs.

Researchers have typically relied on long-chain organic ligands (e.g., oleic acid and trioctylphosphine). To enhance optoelectronic properties, the long insulating original ligands on the surface of the nanocrystals are exchanged or functionalized with new bidentate monovalent shorter ligands, which leads to decreased interparticle spacing, reducing the energy barrier to charge tunneling between NPs. The reduction of the ligand chain length has been shown to improve photoconductivity by improving electron and hole transport and the efficiency of charge separation on photogenerated excitons. The final functional group plays an important role in the passivation of the NP surface and thus in the control of midgap states and shallow traps [57, 138-141]. AnI illustration of the reduction in inter-particle distance through ligand exchange can be seen in Figure 2.1.

Various short molecules are used to passivate PbS QDs and exchange the long ligands with shorter ones, such as 1,2 ethanedithiol (EDT), 1,3-propanedithiol (PRDT), 1,4-butanedithiol (BDT), 1,5-pentanedithiol (PEDT), 1,6-hexanedithiol (HDT), 1,2 benzenedithiol (BZDT), *n*-butylamine, sodium hydrosulfide hydrate (NaSH) and 3-mercaptopropionic acid (MPA) have been used for this purpose, through a layer-by-layer dip or spin-coating exchange process. This achieves a functional PbS NPs based SC [129]. Each type of ligand affects the PbS NP properties: for example, significant enhancement of the mobility-lifetime of charge carriers in MPA-capped PbS NP films, as compared to dithiol-capped films is noticed and leads to an increase in both the diffusion length of charge carriers and the power conversion efficiency of PbS NP based SCs [142]. The current density of tin dioxide (SnO_2) SCs increased 43 times after replacing the long chain oleic acid ligands with short chain *n*-butylamine [143]. It was found that a treatment with hexadecyl trimethyl ammonium chloride (HTAC), tetrabutyl ammonium iodide (TBAI) and tretrabutyl ammonium bromide (CTAB) lead to substituting the long ligand (olic acid) with the shortest inorganic ligand halide anions such as Cl^{1-}, I^{1-} and Br^{1-}, respectively. At the end of the synthesis of PbS NPs, halide anions can effectively passivate the surface traps of PbS NPs, such a passivation can lead to better and more stable device performance. EDT molecules are approximately 0.5 nm in size, *n*-butylamine (0.6 nm), chalcogenide complexes such as $Sn_2S_6^{4-}$ (0.7 nm), and halide anions such as Cl^{1-}, Br^{1-} and I^{1-} come in sizes down to 0.1 nm [144]. Recently Tang, et al. [144] synthesized PbS QDs with a diameter of 5.0. They estimated the average inter-dot spacing of 1.0 nm in the inorganic halide treated films, 2.1 nm in EDT treated films and 1.8 nm in MPA-treated films. To date using the different ligands: organic ligands [37], inorganic ligands [144], and hybrid ligands [21] as a cross-linker and bridge to replace oleic acid NPs achieved power conversion efficiency rates of 5.6%, 6%, and 7% [21, 37, 144], respectively.

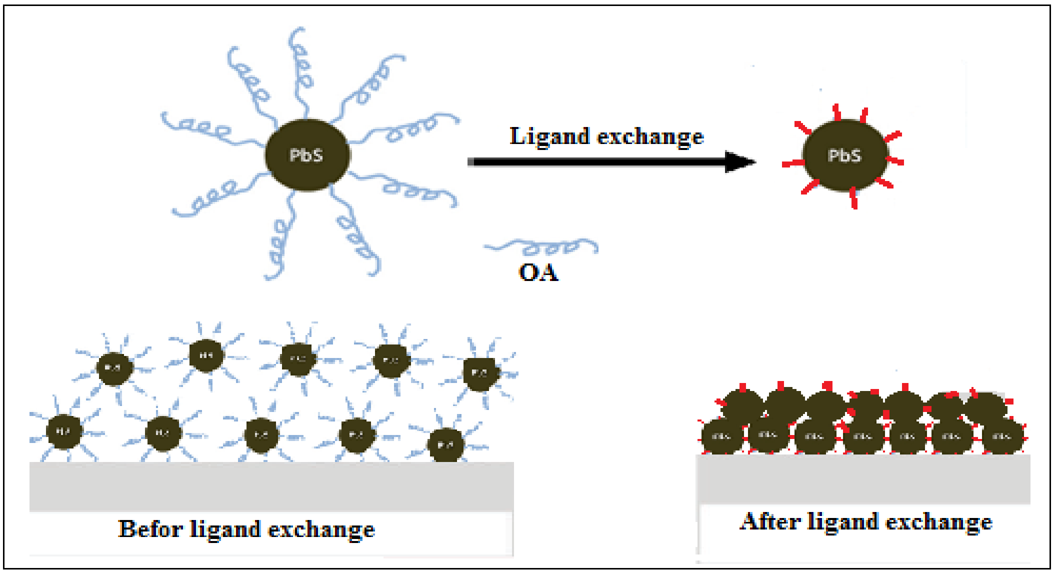

Figure 2.1 Schematic of ligand exchange of organic capping ligands (OA) with smaller organics (EDT or pyridine), inorganics (metal chalcogenide complexes or hydrazine), or ions (halide anions; Cl, Br, or I). Ligand exchange is performed with nanocrystals dispersed in a solvent (top) or as deposited film (bottom).

2.1.5 CuO Nanoparticles

Copper oxide (CuO) is an attractive p-type metal oxide semiconductor that has unique electrical, optical and catalytic properties [145]. CuO is widely used in electrochemical cells [146], gas sensors [147-149], magnetic storage media [150, 151], photovoltaic cells [152], light emitters [153], thermoelectric materials [154, 155], heat transfer nanofluids and for catalysis [156-158]. Using CuO NPs with narrow size distribution for these applications would further promote the chemical reactivity of the NPs because as the surface-to-volume ratio of the particle increases, the number of reactive sites increases [159-163]. Thus, CuO NPs exhibit improved electronic and optical properties compared to their bulk equivalent [49, 164, 165]. As a result, many methods have been developed to synthesize CuO NPs with different sizes as shown in Table 2.1.

Microwave radiation generates heat by interacting with the solution molecules and causing friction between them due to the reorientation of their electric dipoles [166]. This leads to an increase in reaction kinetics, by one to two orders of magnitude, and more efficient volumetric heating when compared to conventional heating. In addition, the microwave-thermal method has many advantages such as: low synthesis temperatures, reduced reaction time, small particle size, narrow particle size distribution, high purity, low power consumption and it is also environmentally friendly [167-169]. In this study CuO NPs were synthesized using a colloid microwave-thermal process that allows the formation of NPs with excellent size control. In addition, variation in optical behavior as a function of CuO NP size has been investigated in this study.

Table 2.1 Synthesis methods of CuO NPs with size range.

Preparation method	Size (nm)
Sonochemical synthesis	10 nm to several microns [170]
Spinning disk reactor	20-30 nm [171]
Thermal decomposition	15-30 nm [172]
Solid state reaction	15-20 nm [173, 174]
Microemulsion system	5-25 nm [175]
Precipitation pyrolysis	11-35 nm [176]
Sol-gel techniques	7-9 nm [177] and 1-10 nm [178]
Alcohothermal decomposition of copper acetate	3-9 nm [179] and 6 nm [180]
Electrochemical synthesis	4 nm [181]
Precipitation synthesis	4 nm [182]
Colloid-thermal synthesis	3 and 5 nm [183]
Microwave irradiation	3-5 nm [165]

2.1.6 CdS Nanoparticles

Cadmium sulfide (CdS) is one of the most essential II–VI binary group n-type semiconductors [184]. It has properties that are suitable for optical and photoelectric applications such as thin-film transistors [185], diodes, photoresistors, phosphors and photovoltaic devices making it particularly useful for SCs [186-189]. CdS has a direct bandgap of 2.42 eV that results in superior visible light absorption [190], good optical transmittance, high absorption coefficients, a high electron affinity, low resistivity and easy ohmic contact [191-194]. In addition, it is used as window layer for heterojunction solar cells due to its good chemical stability, a low cost deposition technique [195], good uniformity in order to avoid electrical short circuit, high conductivity at more than 10^{16} carriers/cm^3 [196], and high transparency in the visible spectral region [197]. It has two common crystalline phases of hexagonal wurtzite and cubic zinc blend [198-200]. The bulk wurtzite structure is a thermodynamically stable phase which exists under normal conditions (such as atmospheric pressure and room temperature) [201].

CdS NPs have been successfully synthesized using different materials as a source of cadmium ions ($Cd(NO_3)_2$), $CdCl_2$, $Cd(CH_3CO_2)_2$ or CdO) and as a source of sulfide-ions (thiosulfate, thioacetamide, or thiourea). A wide range of deposition methods have been reported including; spray pyrolysis [202], radio frequency sputtering [203, 204], vacuum evaporation [205], metal organic chemical vapor deposition [206], chemical bath deposition [207, 208] and successive ionic layer adsorption and reaction (SILAR) [209]. The SILAR technique was used to deposit CdS NPs for device fabrication.

2.1.7 Bi_2S_3 Particles

Bismuth sulfide Bi_2S_3 is one of the most important V-VI n-type semiconductors that have applications in photoelectrochemical cells (PECs) [210, 211] lithium ion batteries, gas sensors [212], optoelectronic devices, IR spectroscopy photodetectors in the visible wavelength region, solar cells and thermoelectric devices [213]. Bi_2S_3 has an E_g in the range of 1.3-1.5 eV [214, 215], lies in visible solar energy spectrum which makes it useful for solar energy conversion devices [216] as it is very close to the optimal gap (1.4 eV) for a solar absorber [217] and it has a a high absorption coefficient (α) of ~ 105 cm^{-1} (at λ = 600 nm) [218]. These features make Bi_2S_3 a promising candidate for solar absorbers. In addition, the source materials for Bi and S ions are abundant and thus readily available at low cost**.**

Various reports deal with the deposition of Bi_2S_3 thin films using different methods such as chemical bath deposition [219-221], spray pyrolysis [222-224], solution-gas interface techniques [225] and electrode positioning [226, 227] using different sulphide ion releasing source such as thiosulfate, thioacetamide and thiourea [228, 229]. However, very few reports are available on the deposition of Bi_2S_3 thin films via the successive ionic layer adsorption and reaction method (SILAR) [216, 230, 231]. The SILAR method for preparation of thin films is attractive, easy to control in terms of the overall growth rate, cost effective and less time consuming compared to other methods [232]. It is based on the immersion of substrates on separately placed cationic and anionic precursors and rinsing between every immersion with ion exchange water to avoid homogeneous perception [233]. It depends on the attractive force between the ions and the surface of the substrate. In the present study we have synthesized Bi_2S_3 thin films using the SILAR technique**.**

2.1.8 Reduced Graphene Oxide (GO)

Graphene oxide (GO) is an attractive nanomaterial that has a range of reactive oxygen functional groups such as: oxygen, epoxide rings (bridging oxygen atoms), carbonyl (=CO), hydroxyl (-OH), phenol groups [234, 235]. GO properties can be controlled entirely by monitoring the amount of its functional groups and consequently changing its electrical, mechanical and thermal properties according to the required application. GO is used in polymer composites, energy-related materials, sensors, paper-like materials, field-effect transistors and biomedical applications.

Graphene or GO are two structures with completely different properties. One of them can lead to the production of the other and has the ability to produce a wide range of intermediate materials inbetween. Graphene is a two-dimensional atomic-scale hexagonal honey-comb lattice of carbon atoms. It is the most recently discovered carbon-based allotropic form, after fullerenes and carbon nanotubes [236, 237]. It has extremely high electric and thermal conductivity, as well as excellent mechanical and optical properties [238]. Graphene can be obtained by the mechanical exfoliation of graphite, but only giving a low yield. Alternative approaches toward its large scale production involve the utilization of either chemical vapor deposition [239, 240] or a reduction of graphene oxide (GO) [241-243]. GO is electrically insulated owing to the decrease in the number of double bonds between carbon atoms, and thus a decrease in the conjugation length and a disruption of graphitic networks. Sp^2 hybridization in carbon atoms partially gives way to sp^3 hybridization, thus converting a conductive material (graphene) into an insulator (GO).

GO can be partially reduced by chemical [244, 245], thermal [245], and ultraviolet-assisted [246] or electrochemical routes [247]. generating reduced graphene oxide (RGO). RGO is a semiconductor of variable bandgap energy depending on the extent of the reduction that ranges between the insulator GO and the conducting graphene. RGO has several electronic and optical applications. Among them are their uses in solar cells. The employment of RGO in SCs has taken several forms. It can be used alone or in combination with other functional materials such as electrocatalysts on counter electrodes to provide an alternative component against costly platinum NPs [248]. It has also been used as a means to enhance conductivity either in filling electrolytes or in nanostructure metal oxide semiconductor photoanodes [249, 250]. In most applications related to SCs, graphene-type materials are introduced by their GO form and then they are reduced to give RGO. The reason for this is that GO is easily dispersed in aqueous media as well as in polar organic solvents, facilitating either its deposition onto substrates or mixing with other substances. This is not possible with RGO or, even worse, with pristine graphene, which are not dispersable in any medium [251]. Figure 2.2 shows pictures of as-prepared GO dispersed in water and 13 organic solvents through ultrasonication for 1 hour; also Figure 2.2 shows GO dispersions after three weeks, where they precipitate in most of the solvents except water, ethylene glycol, dimethyl formamide (DMF), N-methylformamide (NMF) and tetrahydrofuran (THF).

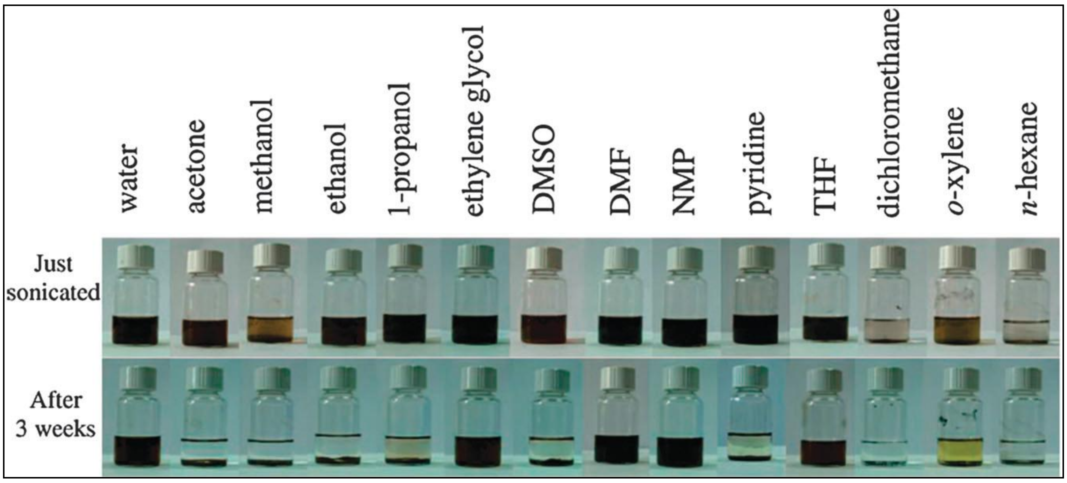

Figure 2.2 Photographs of as-prepared GO dispersed in water and 13 organic solvents through ultrasonication; (Top) dispersions immediately after sonication; (Bottom) dispersions 3 weeks after sonication (from ref. [251]).

2.1.9 Poly [3, 4-ethylenedioxythiophene] -Poly [styrenesulfonate] (PEDOT: PSS)

Currently, a variety of semiconducting polymers are available for applications such as printing electronic circuits, organic SCs, organic light-emitting diodes, supercapacitors, actuators, electrochromism, chemical and bio-sensors, flexible transparent displays, electromagnetic shielding and as an alternative to the transparent conductor indium tin oxide. The most common semiconducting polymers used in SCs can be classified as: (i) derivatives of phenylene vinylene backbone – its chemical structure is represented in Figure 2.3a – such as; poly[2-methoxy,5-(20-ethyl-hexyloxy)-p-phenylenevinylene)] MEH-PPV) with bandgap energy (E_g) of 2.4 eV [252]. (ii) Derivatives of the thiophene chain (its chemical structure is represented in Figure 2.3b) such as; [Poly(3-hexylthiophene)] (P3HT) with E_g of 2.1 eV [253, 254], [poly (4,8-bis(octyloxy) benzo(1,2-b:4,5-b) dithiophene-2,6-diyl) (2-(dodecyloxy) carbonyl)thieno(3,4-b) thiophenediyl)] (PTB1) with E_g of 1.62 eV, poly[2,5-bis(3-

alkylthiophen-2-yl)thieno[3,2-b]thiophene)] (PBTTT) with E_g of 1.5 eV [255, 256], poly[5,7-bis(4-decanyl-2-thienyl)thieno [3,4-b] diathiazole-thiophene-2,5)] (PDDTT) with E_g of 1.1 eV [257], and poly[2,5-(7,7-dioctyl)-cyclopentadithiophene] (PDOCPDT) with E_g of 1.8 eV [253, 258]. (iii) Derivatives of benzothiadiazole backbone (its chemical structure is represented in Figure 2.3c) such as; [poly[(4,40-bis(2-ethylhexyl)dithieno[3,2-b:2,3-d]silole)-2,6-diylalt-(2,1,3-benzothiadiazole)-4,7-diyl] (PSBTBT) with E_g of 1.45 eV [259]. In addition to conducting polymers that contain both thiophene and benzothiadiazole groups such as: [poly[2,5-(7,7-ioctyl)-cyclopentadithiophene], poly[N-9-hepta-decanyl-2,7-carbazole-alt-5,5-(4,7-di-2-thienyl-2,1,3-benzothiadiazole)] (PCDTBT) with E_g of 1.9 eV [260], and poly[2,6-(4,4-bis-(2-ethyhexyl)-4H-cyclopenta[2,1-b;3,4-b]-dithiophene)-alt-4,7-(2,1,3 benzothiadiazole)] (PCPDTBT) with E_g of 1.73 eV [261].

Semiconductor polymers offer two types of carriers, electrons and holes, which transfer through hopping mechanisms rather than through band-like transport, due to their tangled chains of conjugated polymers, wide range of carrier mobility, etc. The previously mentioned semiconductor polymers have been reported with electron mobility ranges from 10^{-4} to 10^{-9} cm^2/Vs [262, 263] while hole mobility is typically higher in the order of (10^{-1} to 10^{-7}) cm^2/Vs [262, 264, 265]. To compare, the electron and hole mobility in crystalline silicon is 1500 and 475 cm^2/Vs, respectively [266].

Poly (3,4-ethylenedioxythiophene) (PEDOT) belongs to the thiophene derivative group and has excellent optical and electrical properties as well as high conductivity and is considered as the most chemically stable conducting polymer currently available [267, 268]. However, PEDOT is an insoluble material which limits its use in many applications, so usually it is synthesized in the presence of other water soluble semiconducting polymers, typically poly (4-styrenesulfonate) (PSS) so an aqueous dispersion can be obtained that can be cast into thin films. In the films the polycationic PEDOT chains are incorporated into a polyanionic PSS matrix to compensate for the charges. Poly (3, 4-ethylenedioxythiophene: poly (4-styrenesulfonate) [PEDOT:PSS] has several superior properties as low temperatures, excellent stability, large area processing, low costs and flexibility. However, the efficiency of this material is limited by its low carrier mobility [269]. The hole mobility is calculated using a general formula for conductivity (σ) [270].

$$\sigma = q\,(n.\,\mu_n + p.\mu_p) \qquad (2.1)$$

Where q is the electron charge = $1.6\text{x}10^{-19}$, n is the concentration of electrons, μ_n is electron mobility, p is the concentration of holes, and μ_p is hole mobility. In case of PEDOT: PSS, only holes contribute to the transport of the charge. Injected free electrons will immediately recombine at oxidized PEDOT sites; hence the transport of electrons does not contribute to the overall current. The hole mobility in PEDOT:PSS can be calculated as approximately $\mu_p = 20$ cm²/Vs for the given conductivity and the estimated hole density for the most widely utilized polymer for organic light emitting diodes and photovoltaic cells [271].

PEDOT:PSS including thin films deposited from an aqueous PEDOT:PSS dispersion have been utilized in a wide range of applications such as a hole conducting layers [267, 272] of photovoltaic (PV) charges [273], light-emitting diodes (LEDs) [274], memories [275], sensors [276], as active material for electrochromic devices [277], field-effect transistors [278], circuits in general [279], in antistatic coatings [280] and particularly in bulk heterojunction organic SCs due to its high transparency, high working functions, smooth morphology and good conductivity. So, the holes are easily collected via the PEDOT:PSS layer from the highest occupied molecular orbital (HOMO) of the organic layer [280]. A range of work functions has been reported from 4.7 to 5.4 eV [281-283] and it has been found that this level can be tuned to minimize the hole injection barrier at the anode [284] in organic LEDs [285] and PV cells [286].

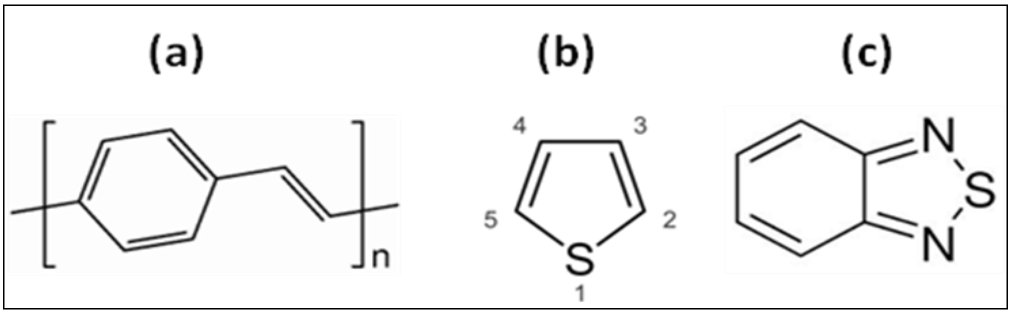

Figure 2.3 (a) Polyphenylene vinylene chemical structure, (b) Thiophene molecule skeletal formula of the five member aromatic heterocyclic with four carbons to one sulfur atom, the numbering convention for derivatives, (c) Benzothiadiazole chemical structure.

2.2 Quantum Dot Solar Cells

2.2.1 Solar Cell Work Principle

Two different PV types are available, depending on the semiconductors used in the solar cell structure. The first SC type is based on bulk inorganic semiconductors such as silicon and works in two steps: it absorbs photons when exposed to light and excites electrons to higher energy states thus creating mobile electrons and holes. These charge carriers are swept across the device under the effect of a built-in electric field generating a flow of electrons through a load that can then be used immediately or can be stored for later consumption. The second SC type, based on organic semiconductors or QDs, works in three concecutive steps: it absorbs photons to create electron–hole pairs known as excitons, so dissociation of the charges is required before collection at the electrodes as an extra step. Exciton dissociation is believed to occur at interfaces between materials with different electron affinities and ionization potentials, where the electron is accepted by the material with the larger electron affinity and the hole by the material with lower ionization potential. The E_g is therefore of great importance in SCs as it limits the maximum amount of light that can theoretically be absorbed, and thereby the maximum electric current that can be achieved. The E_g can be approximated by equation (2.2) [287]:

$$E_\lambda = h \cdot v = h \cdot c / \lambda \qquad (2.2)$$

Where E is the energy, λ is the wavelength, h is Planck's constant, v is the frequency and c is speed of light in vacuum.

In a preferred structure, the solar cell involves a trilayer structure where the photovoltaic active nanomaterial layer is sandwiched between an electron blocking layer of p-type material and a hole blocking layer of n-type material. Figure 2.4a shows a schematic structure for a typical quantum dot solar cell which, according to our study, consists of: (i) a glass or plastic substrate, (ii) a bottom transparent conductive electrode (TCE) layer made of a material such as indium tin oxide coated on the substrate, (iii) an ultrathin buffer electron transport layer (ETL) made of n-type material introduced between the active layer film and the bottom electrode to facilitate suppression of electron- hole recombination, (iv) an active layer (AL) which is a light absorbing nanomaterial film consist of n-type semiconductor material selected from n-type QDs and a p-type material selected from p-type QDs as a blend or two layers, (v) an interfacial ultrathin buffer hole transport layer (HTL) made of p-type material introduced between the active layer film and the top electrode to facilitate passivation of the interface and inhibition of electron-hole recombination and (vi) a top metal electrode (ME). The solar cell structure allows efficient exciton dissociation at the interface of the layers due to the electron affinity differences between the constituent semiconducting materials, and consequently charge separation and transport to the opposite electrodes.

The n-type material is selected from n-type nanocrystals made of semiconductors such as: Bi_2S_3, FeS_2 (pyrite), FeS, ZnO, TiO_2, copper sulfide, PbS, PbSe, PbTe, CdSe, CdS, Si, Ge, copper zinc tin sulfide (CZTS), and copper indium gallium diselenide (CIGS). On the other hand, the p-type material is selected from PbS, PbSe, PbTe, Cu_2O, CZTS, CIGS, Si, Ge, copper sulfide, FeS_2 and FeS. The n-type material in the hole blocking layer preferably has a conduction band at least as large as that of the n-type material in the active layer and a valence band at the most as large as that of both the p-type and n-type materials in the active layer. The p-type material in the electron blocking layer preferably has a valence band (VB) at the most as large as that of the p-type material in the active layer and a conduction band (CB) at the most as large as that of both the p-type and n-type materials in the active layer as shown in Figure 2.4b.

A number of techniques for photon to electricity conversion have been attempted using different materials in an effort to improve efficiency and reduce costs. This ranges from single and multijunction SCs then passing through thin film technology and ends with organic and inorganic cells utilizing QDs within SCs as an active layer. SC efficiency can be estimated through measuring several parameters as shown in the next section.

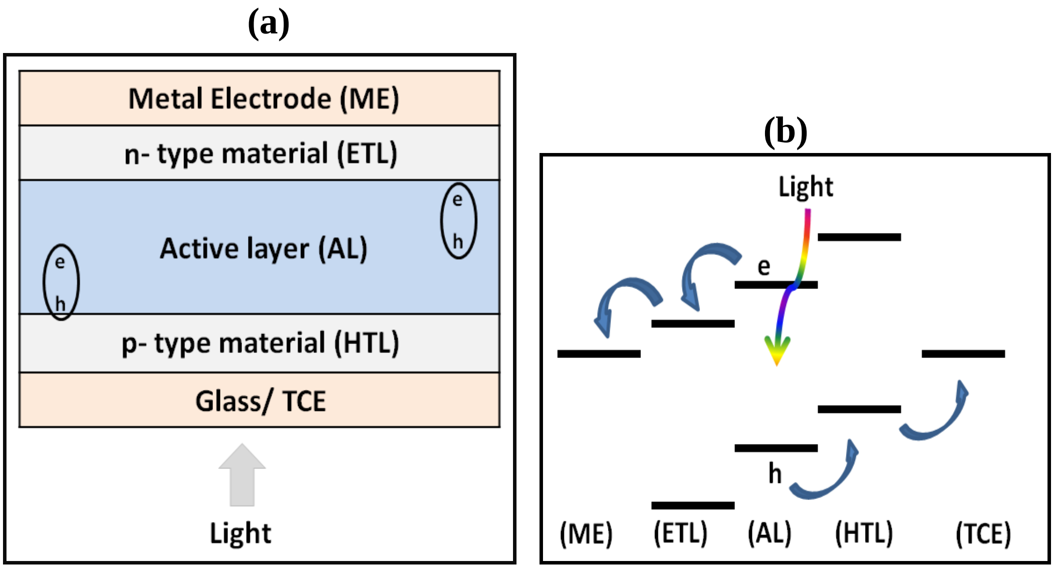

Figure 2.4. (a) Schematic structure of a typical solar cell. (b) Energy level diagrams for a typical solar cell.

2.2.2 Basic Terms for Photovoltaic Performance

Without illumination, a solar cell has the same electrical characteristics as a large diode. A diode is a two terminal device, having two active electrodes, between which a semiconductor allows the transfer of current in one direction as shown in Figure 2.5a. The current through an actual diode (as with solar cell in the dark) as a function of voltage is expressed in equation 2.3 [319,320]:

$$I = I_0 \left(e^{\frac{qV}{nkT}} - 1 \right) \qquad (2.3)$$

Where: I is the net current flowing through the diode; I_0 is the dark saturation current, which is the diode leakage current density in the absence of light; V is the applied voltage across the terminals of the diode; q is absolute value of electron charge; k is Boltzmann's constant; T is absolute temperature (K); and n is ideality factor, a number between 1 and 2 which typically increases as the current decreases. At 300 K and n=1, kT/q = 25.85 mV that is the ‘thermal voltage’.

When the cell is illuminated it begins to generate power as shown in Figure 2.5b. Illuminating a cell adds to the normal ‘dark’ currents in the cell so the general equation for an ideal solar cell becomes [288-290]:

$$I = I_L - I_0 \left[\exp\left(\frac{qV}{nkT} \right) \right] \qquad (2.4)$$

Where: I is the cell output current, I_L is the light generated current, V is the voltage across the cell terminals, T is the temperature, q and k are constants, n is the ideality factor.

The most standard measurement for SCs is the current density (J) versus voltage (V), which measures the current density that can be drawn out of the cell as a function of voltage applied to the cell. A typical J (V) curve for a solar cell in the dark and then under illumination is shown in Figure 2.6. There are several other cell characteristics which can be measured from the J (V) curve.

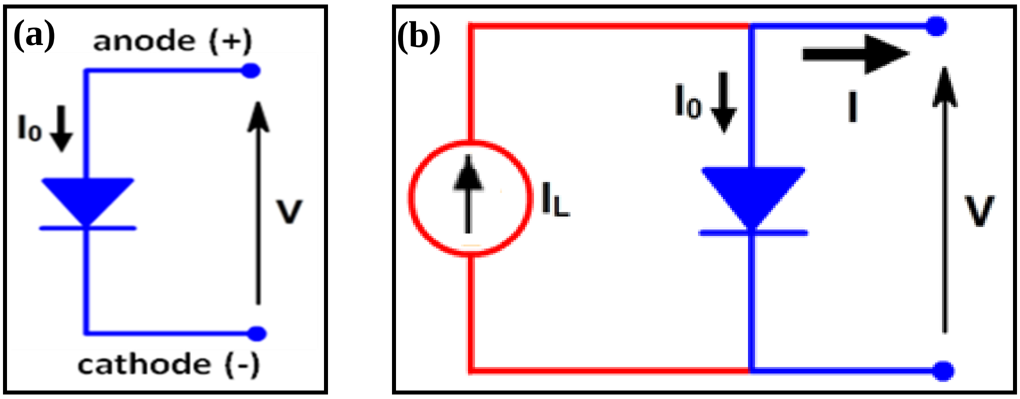

Figure 2.5 Electrical circuit diagram of an ideal photovoltaic cell; (a) without illumination, (b) with illumination.

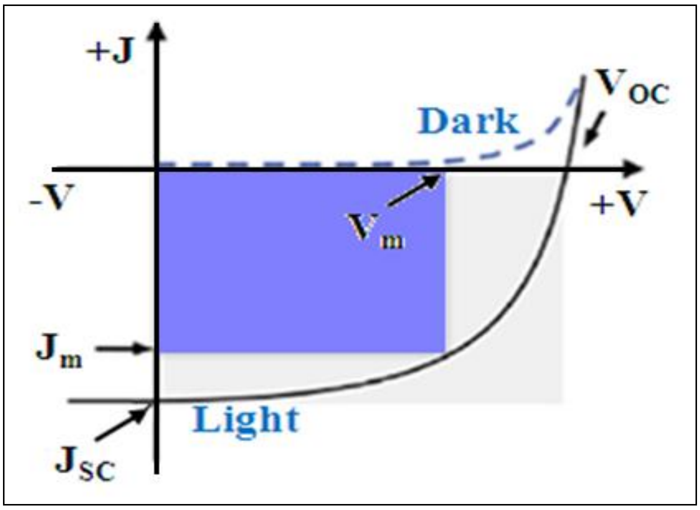

Figure 2.6 J (V) curve. The intersection with the x- and y-axis is called the open circuit voltage (V_{OC}) and the short circuit current (J_{SC}) respectively. The point where the product of J·V is of greatest magnitude is called the maximum power point (P_{MAX})

Air mass coefficient (AM): The sunlight incident angle affects the light intensity on the Earth’s surface. Moreover, the atmosphere alters the sun’s radiation by absorbing and reflecting selected wavelengths. AM is commonly used to characterize the performance of SCs under standard conditions. AM is defined as the ratio of the path length of the sun rays through the atmosphere (L) when the sun is at a given angle (z), called the zenith angle, to the shortest possible path length when the sun is vertical on the Earth’s surface at sea level (L_0), that is referred to as zenith path length, the air mass coefficient is [291]:

$$AM = \frac{L}{L_o} \approx \frac{1}{\cos z} \qquad (2.5)$$

Figure 2.7 shows several cases of atmospheric effects on solar intensity, and describes the parameters in formula (2.5). AM0 denotes the spectrum outside the atmosphere, used to characterize SCs in space power applications such as communications satellites. AM1 denotes the spectrum after passing through the atmosphere perpendicular to sea level (z=0°), used to characterize SCs in equatorial and tropical regions. 1.5 AM denotes the spectrum after passing through the atmosphere at a zenith angle of z=48.2°. Actually sunlight passes through 1.5 AM at most locations on the Earth, more than one air mass before reaching the Earth’s surface. Therefore SCs are generally characterized with a normalized spectrum, called AM 1.5 radiation, of 1000 W/m^2 or 1 sun irradiance at 25 ^{o}C. AM2 corresponds to a solar zenith angle of z=60° and AM3 (z=70°) used to characterize SCs at high latitudes such as in northern Europe or in wintertime.

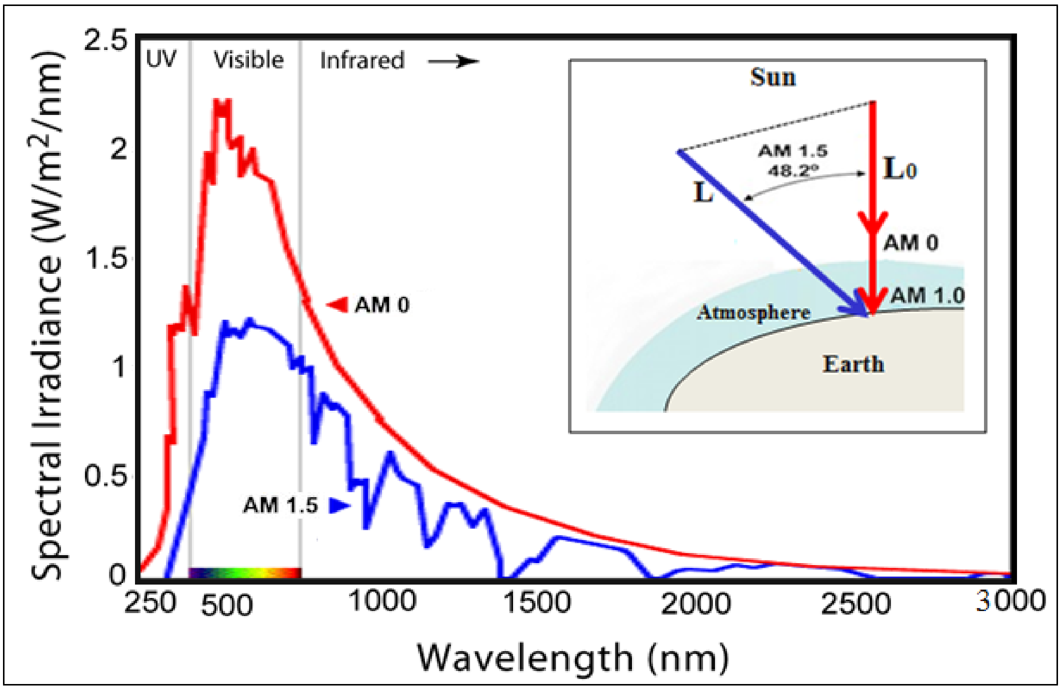

Figure 2.7 Solar irradiance spectrum at the outer edge of the atmosphere (0 am) and at the surface of the earth (1.5 am). The inset is schematic diagram of the origin of the different AM light spectra. http://www.energyharvestingjournal.com

(ii) Open-circuit voltage (V_{OC}): This is the maximum voltage provided by an illuminated photovoltaic device when no external load is connected. This occurs when the cell's net output current is zero. V_{OC} is calculated by the equation (2.6) [288]:

$$V_{OC} = \frac{nkT}{q} \ln\left(\frac{I_L}{I_0} + 1\right) \qquad (2.6)$$

Where kT/q is the thermal voltage I_0 is the dark saturation current, I_L is the light generated current, V is the voltage across the cell terminals, T is the temperature, q and k = 300 K are constants, $n = 1$ is the ideality factor,

The above equation shows that V_{OC} depends on the saturation current of solar cells and light-generated current. The saturation current (I_0) depends on recombination in the solar cells. V_{OC} is then a measure of the amount of recombination in the device. Silicon SCs with high quality single crystalline materials have a V_{OC} of up to 730 mV under one sun and AM1.5 conditions, while commercial devices of multicrystalline silicon typically have a V_{OC} around 600mV.

(iii) Short-circuit current (I_{SC}): This is the maximum current that flows in a PV device when illuminated and its electrodes are connected at zero voltage across the solar cell (see Figure 2.6). I_{SC} depends on the area of the solar cell. To remove the dependence of the solar cell area, it is more common to list the short-circuit current density (J_{SC} in mA/cm^2) rather than the I_{SC}. I_{SC} from a solar cell is directly dependent on the light intensity and the spectrum of the incident light. For most solar cell measurements, the spectrum is standardized to the AM1.5 spectrum.

(iv) Maximum power point (P_{Max}): (J_M, V_M) on the J(V) curve is the point where maximum power is produced. Power (P) is the product of current and voltage (P = IV) and is illustrated in Figure 2.6 as the area of the rectangle formed between a point on the J(V) curve and the axes. The maximum power point is the point on the J(V) curve where the area of the resulting rectangle is largest [288].

$$P_{Max} = J_M \, x \, V_M \qquad (2.7)$$

(v) Fill factor (FF): The ratio of the actual power a solar cell can supply to the maximum predicted by the product of its short-circuit current and its open-circuit voltage [288]:

$$FF = \frac{P_{Max}}{J_{SC}V_{OC}} \qquad (2.8)$$

(vi) Power conversion efficiency (PCE or η): The ratio of power output to power input. In other words, PCE measures the amount of power produced by a solar cell relative to the power available in the incident solar radiation (P_{in}). Here P_{in} is the sum over all wavelengths and is generally fixed at 1000 W/m^2 at 25 ºC when solar simulators are used [288].

$$PCE = \frac{P_{Max}}{P_{in}} \quad \text{Or} \quad PCE = \frac{FFJ_{SC}V_{OC}}{P_{in}} \qquad (2.9)$$

J_{SC} and V_{oc} vary in opposite directions, thus with increasing $E_{g,}$ V_{OC} increases and J_{SC} decreases.

(vii) Quantum efficiency (QE): This refers to the percentage of photons that are converted into electric current when the cell is operating under short circuit conditions. External quantum efficiency (EQE) is the fraction of incident photons that are converted to electrical current, while internal quantum efficiency (IQE) is the fraction of absorbed photons that are converted to electrical current.

(viii) Characteristic resistance (R_{CH}): This is the output resistance of the solar cell at its maximum power point. R_{CH} can be given as an approximation as in equation (2.10a or b) [292]:

$$R_{CH} = \frac{V_{MP}}{I_{MP}} \qquad (2.10a)$$

$$R_{CH} = \frac{V_{OC}}{I_{SC}} \qquad (2.10b)$$

$$R'(\Omega cm^2) = \frac{V}{J} \qquad (2.10c)$$

The area-normalized resistance results from replacing current with current density as in Ohm's law and shown in equation 2.10c. To eliminate the effect of the cell area on the resistance value, a common unit for resistance (Ωcm^2) is used when comparing the resistance of different SCs.

Figure 2.8 shows the circuit diagram of a real solar cell model including the parasitic series and shunt resistances. The series resistance in a solar cell has three causes: firstly, the movement of current through the emitter and base of the solar cell; secondly, the contact resistance between the metal contact and the semiconductor; and finally the resistance of the top and rear metal contacts. The main impact of series resistance is to reduce the fill factor. Low shunt resistance is typically due to manufacturing defects, rather than poor solar cell design, and causes power loss in SCs by providing an alternate current path for the light-generated current. Such a diversion reduces the amount of current flowing through the solar cell junction and reduces the voltage from the solar cell. In the presence of both series and shunt resistances, the equation of the solar cell is given as [319]:

$$I = I_L - I_0 \exp\left[\frac{q(V + IR_S)}{nkT}\right] - \frac{V + IR_S}{R_{SH}} \qquad (2.11)$$

Where: I is the cell output current, I_L is the light generated current, I_0 is dark saturation current, V is the voltage across the cell terminals, T is the temperature, q and k are constants, n is the ideality factor, R_S is the cell series resistance and

R_{SH} is the cell shunt resistance. Like all other semiconductor devices, SCs are sensitive to temperature. The increase in temperature reduces the E_g of a semiconductor and thereby affects most of the semiconductor’s material parameters. A decrease in the E_g of a semiconductor with increasing temperature can be viewed as an increase in the energy of the electrons in the material. Lower energy is therefore needed to break the bond. Thus increasing the temperature reduces the bandgap resulting in reduced V_{OC} and increased I_{SC}.

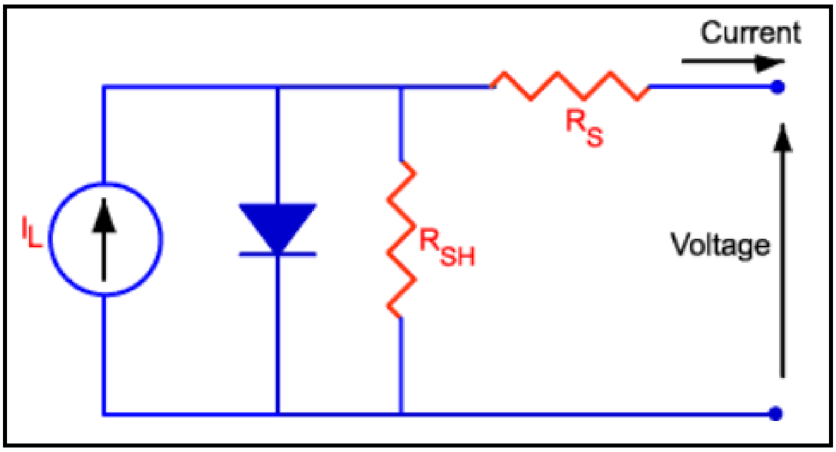

Figure 2.8 Circuit diagram of a photovoltaic cell model including the parasitic series and shunt resistances.

2.2.3 Quantum Dot Solar Cells Configurations

QDs have been reported as promising third generation SCs [54, 293-297]. QDs can be employed in all SCs to reduce cost, enhance absorption and efficiency by controlling the size of the QDs, since several properties can change due to any decrease in the size of the NPs (see section 1.1) [60, 298]. The major confinement effect is an increase in the E_g as the NP size decreases as the CB edge shifts upwards while the VB edge shifts downwards. This leads not only to an absorption of light with higher energy from the solar spectrum, but also to an increase in the driving force for electron and hole injection into the surrounding phases, resulting in direct effects on solar cell performance. QDs have been integrated in different types of SCs such as: Schottky SCs [299, 300], depleted heterojunction SCs [301, 302], hybrid organic/inorganic SCs [303-305] and quantum dot sensitized SCs [306-308]. The structure of different types of QDSCs and their PV performance are explored for the sake of comparison. In addition, the advantages and disadvantages of each structure are discussed.

(i) Schottky solar cells

The Schottky cell is a simple device in which a thin layer (~100 nm) of light absorbing QD is applied between transparent conduction electrodes (TCE), typically indium tin oxide (ITO) and a metal electrode. The photogenerated carriers in the device are separated by a Schottky barrier at the evaporated metal contact. Typical metals used are molybdenum, platinum, silver, gold, aluminum, chromium or tungsten, and the semiconductor would be n-type silicon or p-type QDs. Electrons from the QD thin films are injected into the metal thin film, while presenting a barrier for the hole, thus reducing the possibility of electrons being transmitted back to TCE.

Achieving high efficiency in these cells requires carrier extraction before recombination, accordingly the mobility of each carrier has to exceed $\phi_{built\text{-}in}/d^2$, where the $\phi_{built\text{-}in}$ is the built-in potential, and d is the device thickness. The barrier height of the built-in potential can be estimated by equation (2.12) [299, 300]:

$$q\,\phi_{built\text{-}in} = E_g - q\,(\phi_m - \chi) \qquad (2.12)$$

Where E_g is the bandgap of the QDs, q is the charge of an electron, ϕ_m is the work function of the metal and χ the electron affinity of the QDs.

Charge transfer between the metallic contact and the QDs generates band bending in the QD layer together with a Schottky barrier that makes the contact selective. Notable photocurrents have been achieved [309]. Sketches of the Schottky solar cell based on colloidal QDs, and its equilibrium energy-band diagrams are shown in Figure 2.9.

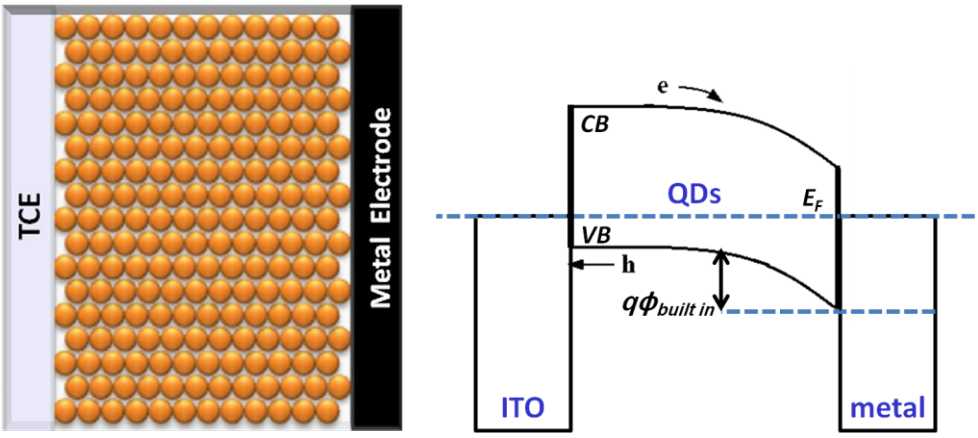

Figure 2.9 Sketches illustrating the Schottky solar cell based on colloidal QDs. Energy-band diagram for the Schottky solar cell.

The advantages of Schottky SCs are: (i) they can be fabricated easily and cheaply as compared to p–n junction SCs, (ii) Schottky SCs are expected to give a better spectral response in the shorter wavelength region due to the near surface depletion regions. Schottky devices also have shown certain disadvantages: many minority carriers (here electrons) must travel the entire film before reaching their destination electrode and are therefore more exposed to recombination processes. The V_{OC} is often limited by Fermi level pinning due to defect states at the metal/QDs interface. Such effects are important in PV as they lead to low V_{OC} devices [310].

One of the most efficient Schottky SCs composed of cadmium telluride (CdTe) nanorods can produce a power conversion efficiency of about 5.3%, J_{SC} ~21.6 mA/cm^2, an V_{OC} ~540 mV and a FF ~45.5%. This is among the highest efficiency reported for this type of device [300].

Table 2.2 summarizes the photovoltaic performance of the best Schottky SCs based on PbS colloidal QD. The table shows that all the high performance cells are composed of PbS colloidal QDs sandwiched between glass/ ITO on one side and Al or Ag the mostly used metals on the other with ultrathin layers of LiF (1-4 nm) deposited just beneath the metal layer. The variation in cell performance results from the different ligands which are used with PbS colloidal QDs in addition to a difference in thickness of the PbS colloidal QDs layers. The most common PCE is 4% [301] where a benzenedithiol (BDT) ligand is used to replace oleic acid, cross links and bridges to the QDs. The thickness of the PbS colloidal QDs layer is in the range of 100 to120 nm, the thickness of LiF layer is 1 nm in order to provide a good lattice match with Ag, and there is 120 nm of Ag on the top. Since the Al and Ag devices were built using identical colloidal QD films, it can be concluded that the loss of device performance is dominated by degradation at the Schottky contact. Ag is less reactive than Al [299] and results in a more stable Schottky contact with PbS QD films.

Table 2.2 Summary of device architecture and photovoltaic performance of PbS QDs based Schottky solar cells.

Structure	Ligand	PCE (%)	Jsc (mA/cm^2)	Voc (V)	FF (%)	Ref.
ITO/PbS/LiF/Al	1,4-BDT	4	14.45	0.46	60	[18]
ITO/PbS/LiF/Al/Ag (3.7) nm	TMPMDTC	3.6	14	0.51	51	[19]
ITO/PbS /LiF/Al (4.5 nm)	1,3- (BDT)	3.8	12.1	0.54	59	[20]
ITO/PbS /Al	*n*-butylamine	1.8	12.3	0.33		[21]
ITO/PbS/LiF/Al/ Ag	EDT	1.72	7.8	0.47	55	[22]
ITO/PbS/LiF/Al/Ag (3 nm)	EDT	2.15	8.57	0.46	54.5	[23]
ITO/PbS QD/Mg/Ag		0.68	7.2	0.25	38	[24]
ITO/PbS/LiF/Al		3.8	11.3	0.57	58	[21]
ITO/PbS/Al		1.8	12.3	0.33	44	[26]
ITO/PbS/LiF/Al		2.2	8.6	0.46	55	[27]
ITO/PbS/LiF/Al		3.9	11.4	0.55	64	[28]
ITO/ZnO/PbS/Au (3.7 nm)	MPA	2.25	8.85	0.52	0.49	[29]

Where BDT is benzenedithiol in acetonitrile, TMPMDTC: *N*-2, 4, 6-trimethylphenyl-*N*-methyldithiocarbamate, EDT is 1, 2- ethanedithiol, and MPA is mercaptopropionic acid. The numbers below the cells structures such as (3.7nm, 4.5nm) denote the PbS NPs size.

(ii) Depleted heterojunction solar cells

Depleted heterojunction solar cells consist of a p-type QDs layer sandwiched between an n-type wide bandgap semiconductor (electron transporting) such as TiO_2 or ZnO layers and a metal electrode. Carrier separation takes place at the QDs/ n-type nanostructure oxide interface. In such structures electrons flow toward the TiO_2 or ZnO layer rather than the evaporated metal contact, back electron transfer from ZnO to QDs is suppressed by the built-in field of the depletion region, thus creating an inverted polarity. Moreover, hole transfer to the evaporated metal contact and back electron transfer to QDs is prohibited which allows efficient carrier separation at the QDs/ZnO interface [302]. Sketches of depleted heterojunction solar cells based on colloidal QDs, and its equilibrium energy-band diagrams are shown in Figure 1.10.

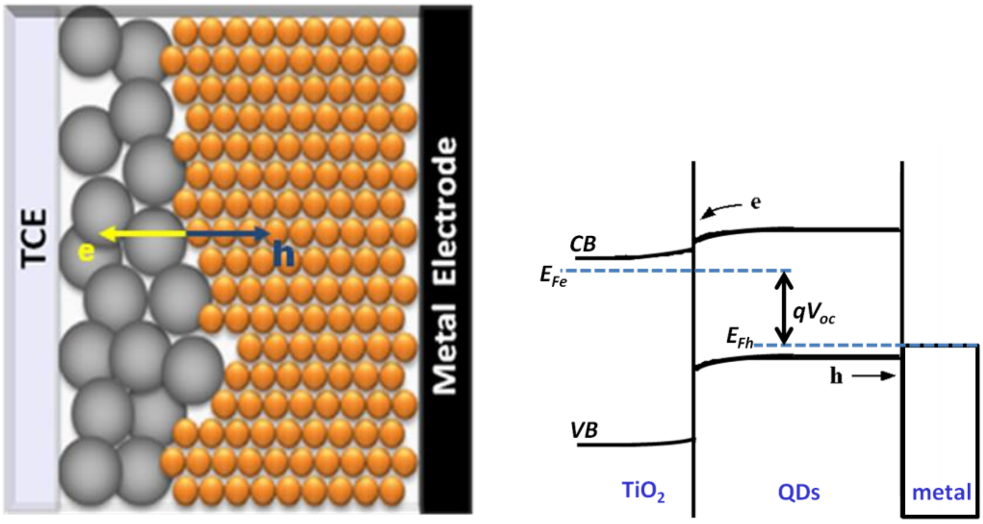

Figure 2 10 Sketches illustrating the depleted heterojunction cell solar cell based on colloidal QDs. Energy-band diagrams for the depleted heterojunction solar cell (right).

Schottky SCs show a depletion layer that arises from charge transfer from the electron accepting contact to the p-type QDs film. Since metals have a very high free electron density (~10^{22} cm^{-3}), there is a negligible depletion region on the metal side of the Schottky junction. Depleted heterojunction SCs overcome this limitation because the n-type wide bandgap semiconductor (TiO_2) electrode is partially depleted in view of its much lower carrier density (~10^{16} cm^{-3}). Also depleted heterojunction design benefits from minority carrier separation due to the placement of the junction on the illumination side. Although the photocurrents achieved in this case are smaller than for Schottky cells, improved open circuit voltages are obtained [22].

Table 2.3 summarizes the photovoltaic performance of the best depleted heterojunction SCs based on PbS colloidal QDs. The table shows that all the high performance cells are composed of PbS colloidal QDs sandwiched between a TiO_2 layer that is deposited on glass/fluorine doped tin oxide (FTO) on one side with Au the most used metal on the other. Sometimes ultrathin layers of MoO_3 or NiO (10 nm) are deposited just beneath the metal layer. Table 2.3 shows that variation in cell performance results from the different ligands which are used with PbS QDs in addition to a difference in the size of PbS NPs. As well as the shape, size or doping with other metal oxides of TiO_2 or ZnO, NPs have a major effect on cell performance. Cells with FTO/TiO_2/PbS/Au architecture reached a PCE of more than 5% where MPA in methanol is used with 3.7 nm PbS NPs. With an increase in the size of the NPs, a decrease in PCE is observed and is related to a decrease of the $V_{OC.}$ With such a decrease in bandgap the V_{OC} will decrease, since the V_{OC} is proportional to the bandgap of the active NP layers in this type of depleted heterojunction SC [30, 31]. An obvious enhancement of the PCE is noticed by utilizing other metal oxides such as ZnO, SiO_2, and Nb_2O_5 to TiO_2 [31] and using TBAII for ligand exchange since the OA chain is substituted by iodide ions with a high PCE [24]. An additional 6% PCE improvement is achieved by utilizing ZnO nanowires in the cell structure and using CTAB for ligand exchange of PS QDs [32]. The most common PCE is 7.4% with FTO/ZnO/TiO_2/PbS/MoO_3/Au solar cell structure, which is the highest reported efficiency rate among all the QD SCs to date, where PbS colloidal QDs are treated with two types of ligand: inorganic and organic; including halide anions (Cl) which are used as very short ligands to replace oleic acid, and MPA in methanol which is used to cross link and bridge the QDs [21].

Table 2.3 Summary of device architecture and photovoltaic performance of PbS CQD based depleted heterojunction solar cell.

Structure	Ligand	PCE (%)	J_{SC} (mA/cm^2)	V_{OC} (V)	FF (%)	Ref.
FTO/TiO_2/PbS/ Au 3.7 nm	MPA	5.1	16.2	0.51	58	[30]
FTO/TiO_2/PbS/ Au 4.3nm	MPA	2.1	13.2	0.45	35	[30]
FTO/TiO_2/PbS/ Au 5.5 nm		0.93	11.3	0.38	21	[30]
FTO/TiO_2 /PbS/MoO_3 /Au/Ag	MPA	6.3	19.9	0.604	52.8	[31]
ZnO-TiO_2/PbS/MoO_3 /Au/Ag	MPA	5.1	17.2	0.65	48.5	[31]
SiO_2-TiO_2/PbS/MoO_3/ Au/ Ag	MPA	5.36	16.9	0.609	51.9	[31]
Nb_2O_5-TiO_2/PbS/ MoO_3 /Au/ Ag	MPA	5.4	18.0	0.610	50.0	[31]
Al_2O_3-TiO_2/PbS/ MoO_3/ Au/ Ag	MPA	2.75	16.4	0.601	30.8	[31]
(FTO)/planar ZnO/PbS QD/Au	CTAB	1.4%	7.53	0.396	45.9	[32]
FTO/ZnO nanowires /PbSQD/Au	CTAB	6.076	34.47	0.361	48.8	[32]
ITO/ZnO/PbS QD/ MoO_3/Au		3.5		0.59		[18]
ITO /ZnO/PbS QD/(NiO solution)		2.5				[19]
ITO/ZnO/PbS QD/ (NiO 10 nm sputtered)		5.3		0.72		[19]
ITO/ZnO nanowires/ PbS QD/ MoO_3/Au	BDT in aceton-etrile	4.4	24.3	0.49	36.3	[20]
FTO/ ZnO /TiO_2/PbS/ MoO_3/Au/Ag	Halide anions, MPA	7.4	21.8	590	58	[21]
ITO/TiO_2/PbS QD/ MoO_3/Au	Halide, MPA	3.25	14.03	0.53		[22]
ITO/TiO_2/PbS/ Au		3.13	20.7	0.456	33.2	[23]
ITO/ZnO/PbS/Au		3.0	8.9	0.59	56	[33]

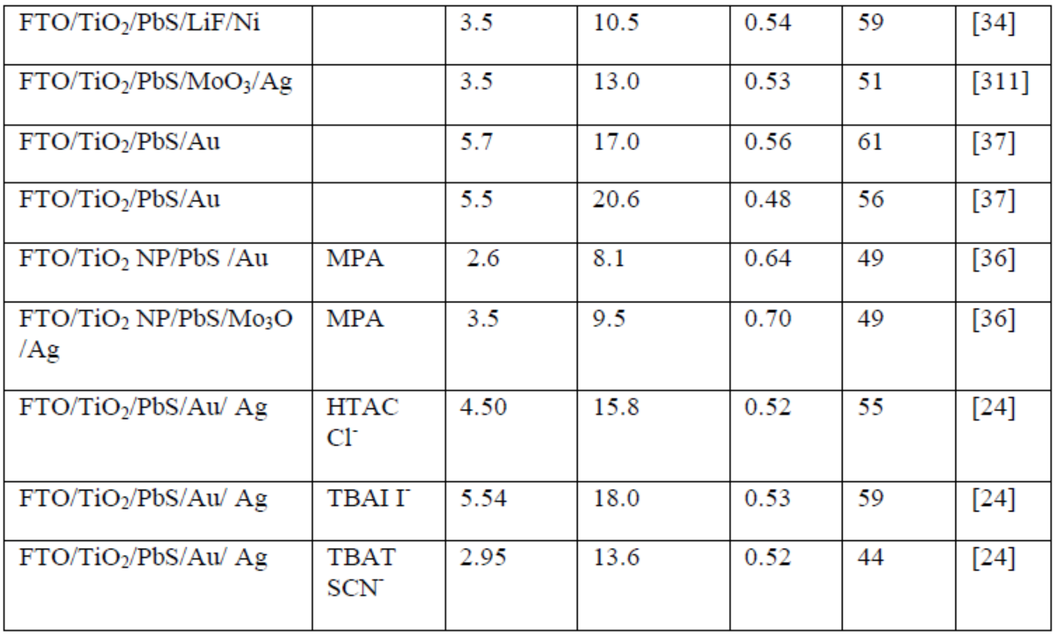

FTO/TiO_2/PbS/LiF/Ni		3.5	10.5	0.54	59	[34]
FTO/TiO_2/PbS/MoO_3/Ag		3.5	13.0	0.53	51	[311]
FTO/TiO_2/PbS/Au		5.7	17.0	0.56	61	[37]
FTO/TiO_2/PbS/Au		5.5	20.6	0.48	56	[37]
FTO/TiO_2 NP/PbS /Au	MPA	2.6	8.1	0.64	49	[36]
FTO/TiO_2 NP/PbS/Mo_3O /Ag	MPA	3.5	9.5	0.70	49	[36]
FTO/TiO_2/PbS/Au/ Ag	HTAC Cl^-	4.50	15.8	0.52	55	[24]
FTO/TiO_2/PbS/Au/ Ag	TBAI I^-	5.54	18.0	0.53	59	[24]
FTO/TiO_2/PbS/Au/ Ag	TBAT SCN^-	2.95	13.6	0.52	44	[24]

Where MPA is 3-mercaptopropionic acid, HTAC is hexadecyltrimethyl ammonium chloride, TBAI is tetrabutyl ammonium iodide, and Nb_2O_5 is Niobium ethoxide. TBAT-SCN is tetrabutylammonium thiocyanate salt dissolved in anhydrous methanol to treat the oleic acid capped PbS QDs layer, this step produced halide-passivated PbS QDs film.

(iii) Hybrid organic/inorganic solar cells

Hybrid SCs are conceptually similar to organic SCs since p-type and n-type organic semiconductors are sandwiched between two electrodes. The only difference is that the organic electron accepting material of PCBM (or other fullerene derivatives) is replaced by inorganic NPs. This could be in the form of QDs and organic semiconductors deposited on top of each other or the QDs dispersed in an organic semiconductor matrix. Also there are more complex nanostructures like nanorods, nanowires or tetrapods, mixed with a polymers such as cadmium selenide (CdSe), cadmium sulfide (CdS), cadmium telluride (CdTe), lead selenide (PbSe) and lead sulfide (PbS) QDs that act as both electron transporting phases and light absorbers (together with the polymer). The greatest efficiency is 3.2%, based upon a PCPDTBT polymer donor and a CdSe NP as theacceptor. This device exhibited a J_{SC} of 10.1 mA/cm^2, a V_{OC} of 0.68 V and an FF of 51% [42]. Sketches of hybrid organic/inorganic solar cells based on colloidal QDs and the equilibrium energy-band diagram are shown in Figure 2.11.

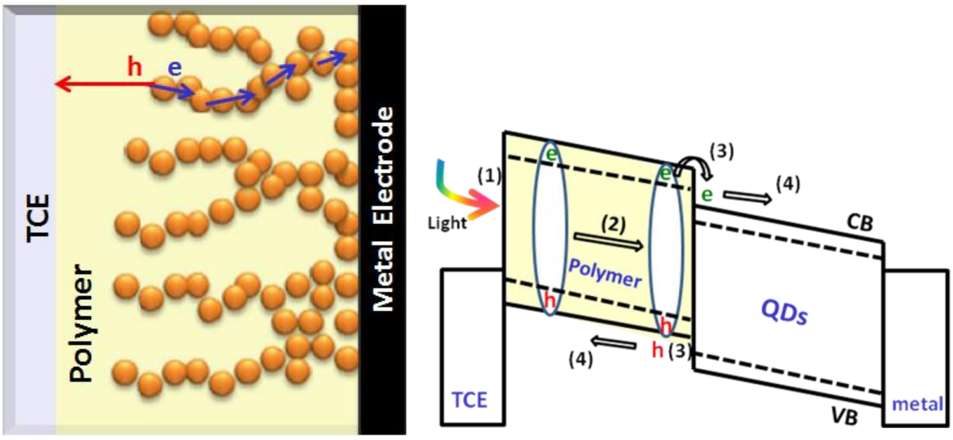

Figure 2.11 Sketches illustrating the hybrid bulk heterojunction solar cell based on colloidal QDs. Energy-band diagrams for the hybrid bulk heterojunction solar cell.

The advantage of hybrid systems is getting the benefits of both organic and inorganic semiconductors in one device. Very thin films of organic semiconductors can be used in hybrid SCs because they possess very high light absorption coefficients and simple processing [311], employing inorganic NPs as acceptor materials with organic semiconductors adds a number of advantages to hybrid SCs which are: (i) the enhancement of environmental stability [312]; (ii) a high contribution of light absorption due to the NPs large surface area [42, 313, 314] as well as the benefits of quantum confinement effects [315]. (iii) High charge carrier mobility leading to the faster transfer rate of photoinduced charge carriers to organic semiconductors. This transfer rate has been observed in the order of picoseconds [316]. (iv) Utilizing inorganic nanostructures such as nanotubes with shapes that are aligned vertically on the substrate within the organic semiconductor matrix, leading to efficient excitonic dissociation and electron transport [317].

Although the above-mentioned advantages associated with inorganic NPs exist, currently the performance of hybrid SCs is lower than organic SCs. Thus the interface between the QDs and organic semiconductor has to be enhanced. Also the surface morphology has to be improved to assist a continuous pathway for transporting the charge [318].

Table 2.4 summarizes the photovoltaic performance of the best hybrid organic/inorganic SC architecture based on PbS colloidal QDs reported to date. The table shows that the highest PCE (3.7 %) is achieved by a combination of PbS QDs with PCBM when LiF buffer layers are deposited just beneath the Al electrode to stop the migration of Al atoms into the device [41].

Table 2.4 Summary of device architecture and photovoltaic performance of PbS QD based hybrid solar cell.

Structure	Ligand	PCE (%)	J_{SC} (mA/cm^2)	V_{OC} (V)	FF (%)	Ref.
ITO/PbS/PCBM/Mg/ Ag	Butylamine, EDT	1.68	14.0	0.24	50	[24]
ITO/PbSQD/ PCBM/Mg/Ag	EDT	1.3	4.2	0.47	62	[24]
graphene/PEDOT:PEG (PC) / ZnO nanowires/ PbS QD/ MoO_3/Au	BDT	3.8	22.5	0.49	34.4	[20]
graphene /RG-1200 /ZnO NW/ PbS QD/ MoO_3/Au	BDT	3.3	18.5	0.54	33.3	[20]
Au/P3HT/PbS/ITO		0.02	0.13	0.4	38	[38]
ITO/PbS/C60/LiF/Al		2.2	10.5	0.4	52	[39]
ITO/PEDOT:PSS/PbS/ $PDTPQ_x$/Al		0.55	4.2	0.38	34	[40]
ITO/PbS/PCBM/LiF/ Al		3.7	10	0.59	63	[41]
FTO/TiO_2/PbS/P_3HT/ PEDOT:PSS/Au	EDT	2.0	8.9	0.53	42.8	[43]

Where PEDOT:PEG (PC) is poly (3,4-ethylenedioxythiophene): poly(ethylene glycol) (PEDOT:PEG) doped with perchlorate (PC) in nitromethane, and NW for nanowire. RG-1200 is organic conductive ink of sulfonated poly(thiophene-3-[2-(2-methoxyethoxy)- ethoxy]-2,5-diyl) in ethylene glycol monobutyl ether/water (3:2). BDT is 1, 3-benzenedithiol [20].

(iv) Quantum dot sensitized solar cells (QDSSCs)

QDSSCs are conceptually similar to dye-sensitized SCs (DSSCs) and first appeared in 1991 [319]. They have similar principles and structure. The only difference between QDSSCs and DSSCs lies in the sensitizer that harvests the sunlight. In DSSCs organic or metal–organic complex dye molecules are utilized while in the case of QDSSCs the dye molecules are replaced by inorganic semiconductor QDs [8, 319-322]. Recently, various QDs have been used for QDSSCs such as CdS [323], CdSe [324], $CuInS_2$ [325], Sb_2S_3 [326, 327] and PbS

[328], where QDs sensitizers attached to a wide bandgap oxide (TiO_2, SnO_2, ZnO, etc.) electrode and absorbs incident light and generates excitons (electron–hole pairs), which are subject to dissociation at the QDs/ wide bandgap oxide interface. The excited electrons are transferred to the wide bandgap oxide nonporous electrode, resulting in oxidation of the QDs. The oxidized QDs accept electrons from redox mediators regenerating the ground state of QD sensitizers. Consequently, the oxidized mediator diffuses to the counter electrode. The injected electrons in the wide bandgap oxide are transported through the external load to the counter electrode, where they are reduced. Sketches of QDSSC based on colloidal QDs, and its equilibrium energy-band diagram are shown in Figure 2.12.

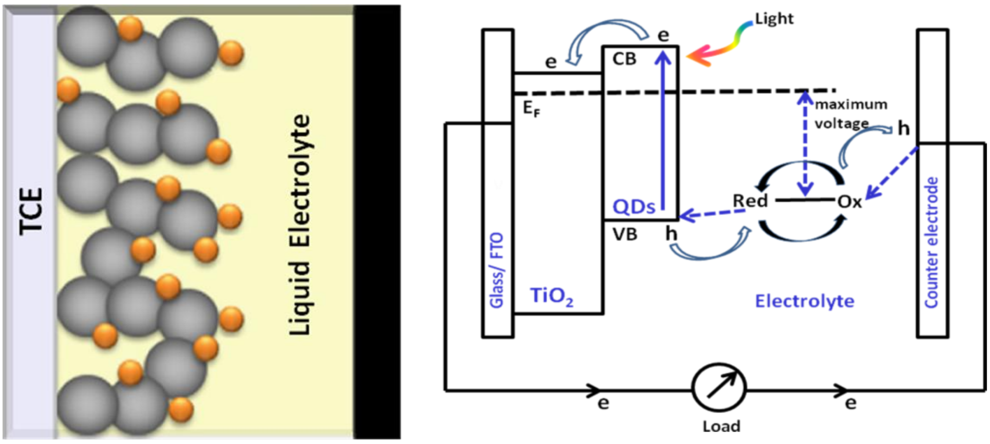

Figure 2.12 Sketches illustrating the QDSSC based on colloidal QDs. Energy-band diagrams for the QDSSC.

QDs have several advantages over conventional dyes: due to tunable size the bandgap of QDs match the solar spectrum. Also their large intrinsic dipole moments can lead to rapid charge separation and a large extinction coefficient, which is known to reduce the 'dark' current and increase overall efficiency. QDs also provide new chances to generate multiple excitons with a single photon. With all the advantages, the best efficiency reported for QDSSCs is 6.5% using perovskite (CH_3NH_3) PbI_3 nanocrystals [329], whereas the first DSSCs exhibited efficiency near to 8 % without particular optimization [319-322]. A recent PCE of 12% has been reported [8].

Table 2.5 summarizes the photovoltaic performance of the best QDSSCs architecture based on PbS colloidal QDs reported to date. In this type of solar cell PbS NPs are applied on the electron acceptor layer mostly using the SILAR method but without applying ligand exchange or cross linker materials. Taking into consideration that PbS QDSSCs performance is still low compared to other semiconductor QDs (CdS, CdSe) due to a lesser injection of electrons to the electron transport layer (wide gap semiconductors) and the instability of PbS in redox electrolytes, etc. [114, 330]. Table 2.5 shows that almost all PbS NP layers are combined with CdS NP layers to improve the cell performance, because ultrathin layers of CdS passivate the PbS layer surface that leads to recombination reduction of photo-injected electrons with the electrolyte and thus enhances the overall performance of the SCs. The greatest PCE obtained for the PbS QDSSC is 4.2%, where the electron acceptor layer is composed of TiO_2. The sensitizer is PbS NPs passivated by CdS NPs, the electrolyte is polysulfide, and the counter electrode is CuS on a brass sheet [44]. Little has been reported on PbS QDSSCs where the electron acceptor layer is ZnO and only recently ZnO nanorods were utilized and shown to exhibit low photovoltaic performance with an efficiency of 2.3 % [46]. Despite the active research on QDSSCs the performance of these devices are still poor compared with DSSCs. The low efficiencies of QDSSCs are often attributed to QDs surface states, which are also called trap states, and may interfere with electron injection from QDs into TiO_2, or back electron transfer that may occur at the solid–liquid interface. Another major concern that limits the PCE is the corrosion of QDs in a liquid electrolyte [308].

Table 2.5 Summary of device architecture and photovoltaic performance of PbS QDs based QDSSC.

Structure	PCE (%)	J_{SC} (mA/cm^2)	V_{OC} (V)	FF (%)	Ref.
TiO_2/PbS/CdS/polysulfise/CuS	4.2	22.3	0.416	45.3	[44]
FTO/ TiO_2 nanorods /PbS/CdS/ polysulfise/Pt	1.3%	10.40	0.47	27	[45]
FTO/ZnO nanorods/PbS /CdS / CdSe / polysulfide / CuS	2.352	12.2	0.621	31	[46]
FTO/TiO2/PbS/polysulfide /Pt	0.61	4.80	0.474	27	[47]
FTO/TiO_2/PbS/CdS polysulfide /Pt	0.15	1.21	0.347	35	[47]
FTO/TiO_2/ CdS/ PbS/ polysulfide /Pt	2.02	11.5	0.581	30	[47]
FTO/TiO_2/ CdS/ PbS/ polysulfide / Cu_2S/ carbon (Cu_2S/C)	3.82	18.84	0.444	45.7	[48]

(v) Quantum funnels (QF), quantum junction (QJ), and heterojunction (HJ) QD solar cells

These three QDSCs were discovered most recently. Their configurations are considered as a development on previous depleted heterojunction SCs. They aim to enhance the connection between QDs and wide bandgap semiconductors.

A quantum funnels solar cell (QFSC) with a PCE of 2.7% was demonstrated by Sargent, et al [331]. They built their graded device by applying the layer-by-layer technique involving a sequence of layers consisting of QDs selected for different size and thus different E_g and consequently various electron affinities. PbS colloidal QDs with a larger are first deposited onto the TiO_2 layer then QDs of a smaller size are deposited as the upper layers. The PbS QDs sizes were 4.7 nm, 4.5 nm, 4.3 nm, 4.2 nm and 4 nm and their corresponding E_g values were 1.06, 1.15, 1.25, 1.30 and 1.35, respectively. The quantum funnels contribute a driving force for photoelectrons from their point of generation towards the electron acceptor layer.

A quantum junction solar cell (QJSC) with a PCE of 5.4% was demonstrated by the same group [332]. They employed a p-type PbS QDs layer then an n-type PbS QDs layer on top of each other to form a junction in which both the p and n type QDs were made of the same semiconductor material, obtained by different doping leading to a gradual decrease in the CB and VB from the p to n type material. This generated a depletion region for efficient carrier separation and collection. See Table 2.6.

A heterojunction quantum dot solar cell (HJ-QDSC) is the same as QJSC except the p and n type QDs are made of different semiconductor materials. Several n-type materials such as CdS and Bi_2S_3 have been combined to PbS QDs in a core shell structure [333]. Two planar layers on top of each other [334, 335], or as bulk, where the n type material is employed as vertically oriented nanotubes, or nanorods, provided electrons with a direct pathway to the electrode. The two p- and n- type materials are blended and dispersed in a solution then utilized for a SC [336]. Table 2.6 shows the highest PCE achieved by HJSC at 4.8% which resulted from a blend combination of PbS: Bi_2S_3 in HJ-QDSC as the active light absorbing layer. This is the highest PCE from this combination to date [335]. While the highest PCE for a PbS: CdS combination in HJ-QDSC was 3.5% [334].

Table 2. 6 Summary of device architecture and photovoltaic performance of PbS QDs based quantum funnel, quantum junction, and heterojunction solar cells, (QFSC), (QJSC), and (HJSC), respectively:

Structure	Ligand	PCE (%)	Jsc (mA/cm^2)	Voc (V)	FF (%)	Ref.
FTO/ TiO$_2$/ PbS graded/ Au. (QFSC)		2.7	11.2	0.51	47	[331]
ITO/ p-type PbS/ MPMDS n-type PbS/ Al/ Ag. (QJSC)	TMAOH for p-type PbS. TBAI for n-type PbS.	5.4	22.2	0.52	47	[332]
ITO/ PbS QD/CdS/Al/Pt (HJSC)	EDT	3.5	15.3	0.54	42	[334]
ITO/PbS/a-Si/Al (HJSC)		0.7	8.99	0.20	39	[337]
ITO/SnS/PbS/Al (HJSC)		0.37	7.22	0.35	32	[338]
ITO/ PbS QD/ Bi$_2$S$_3$/ Ag (HJSC)		1.46	6.81	0.42	51	[336]
ITO/PbS QD/PbS:Bi$_2$S$_3$/ Bi$_2$S$_3$ NP/Ag (HJSC)	MPMDS and EDT	4.87	24.2	0.40	50	[336]
ITO/CdS/PbS-QD/Au/Pt 2.9 nm (HJSC)	EDT	2.45	12	0.56	36.5	[335]
FTO/TiO$_2$ nanorod arrays /PbS/CdS core shell QDs/MoO$_3$/Au (HJSC)	MPA	2.14	7.58	0.501	56	[333]
FTO/TiO$_2$ nanorod arrays/ PbS/ CdS core shell QDs/ PEDOT:PSS/ Au (HJSC)	MPA	1.05	5.61	0.423	44	[333]
FTO/ TiO$_2$ nanorod arrays/ PbS/ MoO$_3$/ Au (HJSC)	MPA	1.53	7.94	0.497	39	[333]
FTO/TiO$_2$ anorodarrays/ PbS/PEDOT:PSS/Au (HJSC)	MPA	1.16	6.14	0.425	44	[333]
ITO/PEDOT:PSS/PbS/ZnO/Al (3.7 nm) (HJSC)	MPA	4.21	12.9	0.58	55	[339]

Where, EDT is 1,2-ethanedithiol**,** MPA is 3-mercaptopropionic acid**,** MPMDS is 3-mercaptopropyl methyldimethoxysilane, TMAOH is tetramethylammonium hydroxide, TBAI is tetrabutylammonium ioidide

Figure 2.13 shows schematic diagrams for the planar (hetero or quantum) junction solar cell structure based on colloidal QDs, and its equivalent energy-band diagram. Figure 2.14 shows schematic diagrams for the bulk (hetero or quantum) junction solar cell structure based on colloidal QDs, and its equivalent energy-band diagram.

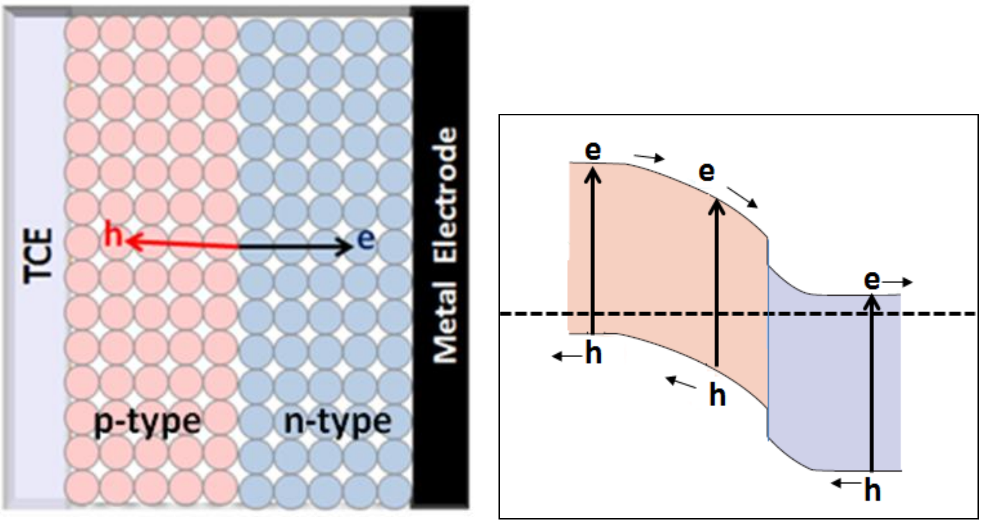

Figure 2.13 Sketches illustrating the planar (hetero or quantum) junction solar cell structure based on colloidal QDs. Energy-band diagrams for the planar (hetero or quantum) junction solar cell structure.

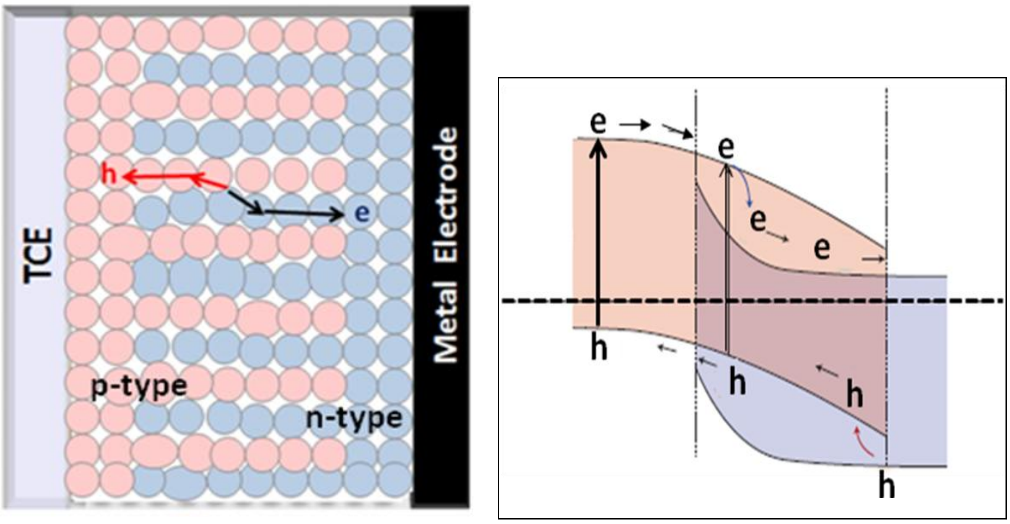

Figure 2.14 Sketches illustrating the bulk (hetero or quantum) junction solar cell structure based on colloidal QDs. Energy-band diagrams for the bulk (hetero or quantum) junction solar cell structure.

CHAPTER THREE

EXPERIMENTS: SYNTHESIS AND CHARACTERIZATION OF QDSCs

This chapter describes materials used and both the synthesis and characterization methods for different types of nanoparticles (NPs) used as composites in QDSC heterojunctions.

3.1 Quantum Dots Synthesis and Characterization

3.1.1 ZnO Nanoparticles (NPs)

ZnO NPs were synthesized using zinc acetate dehydrate [Zn $(CH_3COO)_2.2H_2O$] with 99.9% purity; sodium hydroxide (NaOH) from Sigma-Aldrich (USA); ethanol (C_2H_5OH) from Molar Chemicals Ltd (Hungary); and nitrogen gas (N_2) (UAE) with 99.9% purity. ZnO NPs were produced using a thermal chemical process similar to that described by Chen, et al [340]. A constant concentration of $Zn(CH_3COO)_2.2H_2O$ (1.81 mmol) was used in preparing the samples, while the concentration of NaOH varied from 0.91 to 7.27 mmol. NaOH was dissolved in 100ml of ethanol with rigorous magnetic stirring for 15 min. The precursor solution was then heated to 60° C for 1 hour while stirring producing ZnO NPs dispersed in ethanol. The solution was then allowed to cool to room temperature. The wurtzite structure of ZnO crystals in a general hexagonal lattice structure is shown in Figure 3.1. The chemical reaction for ZnO NP preparation can be described as follows [341]:

$5Zn(H_3COO)_2{\cdot}2H_2O \rightarrow Zn_5(OH)_8(CH_3COO)_2 + 2CH_3COOH$

$Zn_5(OH)_8(CH_3COO)_2 + 2NaOH \rightarrow 5ZnO + 2NaCH_3COO + 5H_2O$

Seven samples of ZnO NPs with different sizes were prepared using the following concentrations of NaOH: 0.91, 1.81, 2.27, 2.72, 3.18, 3.64 and 7.27 mmol. All ZnO NPs dispersed in ethanol were clear and transparent except for the last sample that turned white.

Another approach was used to produce different sizes of ZnO NPs using a microwave reactor (CEM, Discover-SP system, 909156, USA). Microwave irradiation was used instead of conventional thermal heating to shorten the reaction time and reduce the energy costs. $Zn(CH_3COO)_2.2H_2O$ and NaOH were dissolved in ethanol at room temperature using the molar ratios mentioned previously. To complete the reaction and the nucleation process the solution was exposed to microwave radiation for 15 minutes at 60°C at 300W and an operating frequency of 2455 MHz with rigorous magnetic stirring. These were found to be the optimum parameters for investigating the reduction of NP size as a function of NaOH concentration. The resulting NP size was in the range of 10–65nm. Increasing either the microwave power or the duration of irradiation increases the average size of ZnO NPs.

The morphology of ZnO NPs placed on carbon coated copper grids was visualized by a JEOL (JSM-5600, Japan) scanning electron microscope (SEM). The NP size distribution for each sample was characterized by a dynamic light scattering technique using a Zeta sizer from Malvern Instruments (Model

ZEN360, England). The optical properties of the NPs were investigated at room temperature by measuring the ultraviolet–visible (UV-vis) absorption and the photoluminescence (PL) of NPs dispersed in ethanol using a UV-vis spectrophotometer (Shimdzu, UV-2450) and a spectrofluorimeter (Cary Eclipse Fluorescence Spectrophotometer, Varian), respectively. In order to explain the origin of the yellow emissions, the NPs were exposed to UV light at a 365nm wavelength under either ambient air or nitrogen gas (N_2) environments.

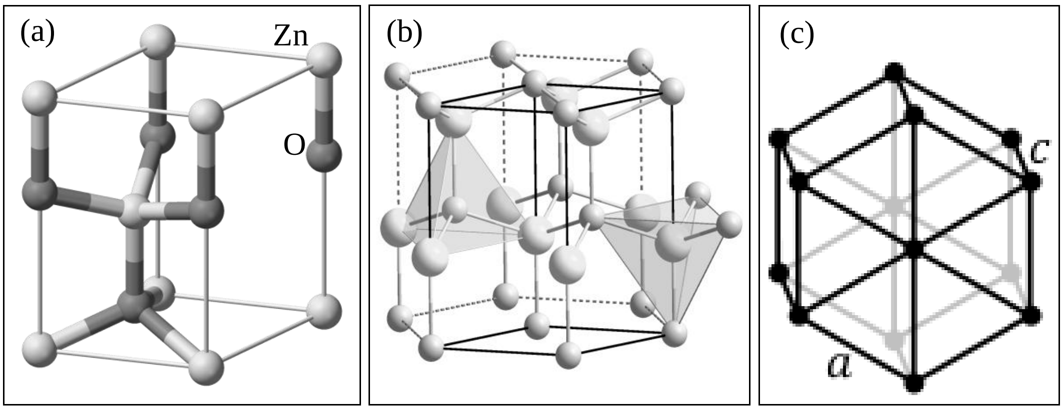

Figure 3.1 Schematic of (a) ZnO wurtzite unit cell (b) ZnO wurtzite structure (c) General hexagonal crystal structure.

3.1.2 TiO_2 Nanoparticles (NPs)

TiO_2 nanopowder rutile form with an NP size of ~ 5nm and 99.7% purity was purchased from Sigma Aldrich (USA). TiO_2 NPs were suspended in ethanol with a concentration of 15mg/1ml, with magnetic stirring for 1 week and sonication for 15 minutes. The resulting TiO_2 NP ethanol suspension was applied to the substrate (see section 3.2.2.) Figure 3.2 shows the tetragonal crystal structure of TiO_2. Each unit cell consists of 15 atoms with 9 titanium atoms and 6 oxygen atoms.

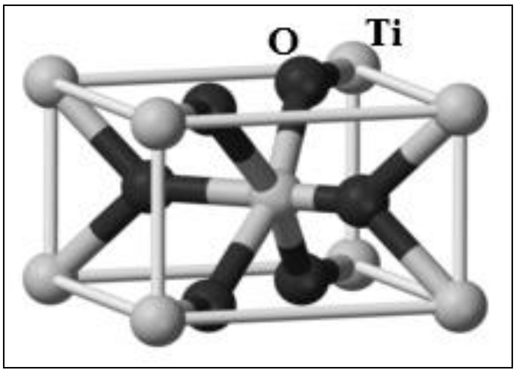

Figure 3.2 Schematic of TiO_2 tetragonal unit cell crystal structure.

3.1.3 PbS Quantum Dots

PbS QDs were synthesized using the following chemicals: lead acetate trihydrate (Pb $(CH_3COO)_2.3H_2O$, 99.9%), oleic acid (OA, technical grade 90%) with the formula $CH_3(CH_2)_7CH=CH(CH_2)_7COOH$, 1-octadecene (ODE, technical grade 90%) and hexamethyldisilal-thiane (TMS). Ethanol (C_2H_5OH) was purchased from Molar Chemicals Ltd (Hungary); acetone (99.8%) was purchased from Panreac (Spain) and n-hexane (95.0%) was purchased from TEDIA (USA).

PbS QDs were prepared as previously reported [334] using a thermal chemical process. In summary, 1.138 g (Pb $(CH_3COO)_2.3H_2O$, 99.9%) was dissolved in a mixture of 2.1 mL of OA and 30 mL of (ODE) at 100°C for 8 hours. Then the solution's temperature was raised to 120°C and at this point a mixture of 0.315mL TMS and 15mL of ODE was injected swiftly into the Pb precursor solution. After stopping the heat the solution was kept on the heating mantle to cool. PbS QDs were extracted by the addition of around 50 ml of acetone to the solution, stirring for 5 minutes and centrifugation at 5000 rpm for 30 minutes to cause precipitatation. They were then purified twice by centrifugation and precipitation: first with ethanol and secondly with acetone.

Finally, they were redispersed in hexane with aconcentration of 10% and saved to be used later, or they can be redispersed in toluene with the same concentration. Figure 3.3 shows the cubic structure of PbS crystals, also called the halite structure, which is related to the sodium chloride (NaCl) cubic crystal structure.

The morphology of the PbS NPs was then visualized using a scanning electron microscope (SEM, JEOL, JSM- 5600, Japan). Samples were prepared on carbon-coated copper grids. The NP size distribution for each sample was characterized by a dynamic light scattering (DLS) technique using a Zeta sizer from Malvern Instruments (Model ZEN360, England). The ultraviolet-visible (UV-Vis) absorption was measured using a UV-Vis spectrophotometer (Shimdzu, UV-2450).

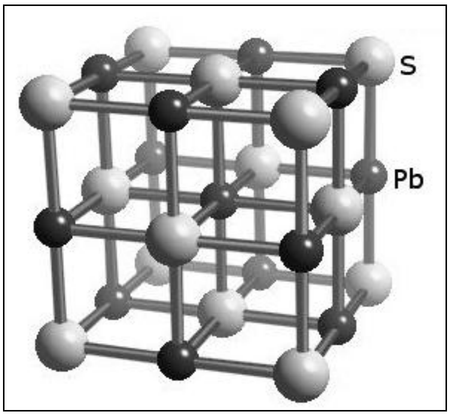

Figure 3.3 Schematic of PbS cubic crystal structure.

3.1.4 CuO Nanoparticles

CuO nanoparticle colloids were synthesized in dimethylformamide $(CH_3)_2NC(O)H$ (DMF) with a purity of 99.0% (Sigma-Aldrich, USA) using a microwave reactor (CEM, Discover-SP system, 909156, USA). The procedure is described as follows: 60mg of copper(II) acetate monohydrate

($Cu(CH_3COO)_2.H_2O$) with a purity of 99.8% (Sigma-Aldrich, USA) was dissolved in 50ml of DMF woth rigorous magnetic stirring for about 3 hours at room temperature. The solution was aged for 24 hours before being exposed to microwave radiation at 45°C at 300W with an operating frequency of 2455 MHz. The solution was kept under rigorous magnetic stirring until the reaction and the nucleation process was complete. The working cycle of the microwave reactor was set as 30 seconds on and 15 seconds off. In order to monitor the particle size, the on/off heating procedure was repeated 36 times and average particle size measurements were taken every 30 seconds. The particle size was found, in general, to decrease as the reaction time increased. Figure 3.4 represents the CuO crystal structure, part of the monoclinic crystal system, where copper atoms are combined with 4 oxygen atoms in an approximately square planar configuration. CuO NP formation can be described according to the following reaction [342, 343]:

$$Cu(CH_3COO)_2.H_2O + (CH_3)_2NC(O)H \rightarrow CuO + CH_3COO_2CHN(CH_3)_2 + H_2O$$

In a typical synthesis of CuO particles**,** a gradual color change from greenish blue to dark brown is noticed and can be inferred as a change in particle size. The gradual changes in the color of the solution during the synthesis stages are shown in Figure 3.5. During the first stage of dissolving $Cu(CH_3COO)_2.H_2O$ in DMF a blue color was noticed. After 3 hours of mixing, the color changed to light green and then became slightly darker after one day. The particle size at this stage was microscale because the reaction was still going on. After repeating the working cycle of the microwave reactor 10 times, the color changed to dark green and the colloidal CuO particles were formed with an average size of about 25nm. With an increase in working cycle times, the color changed to yellowish dark green and the CuO NP average size at this stage was less than 10nm. Repeating the cycle 30 times changed the color to brown and the average NP size was reduced to less than 5 nm.

The morphology and size of the prepared CuO NPs were visualized using a scanning electron microscope (SEM, JEOL, JSM-5600, Japan) and a transmission electron microscope (TEM, FEI, Tecnai G20), respectively. The NP size distribution was determined by a dynamic light scattering (DLS) technique using a Zeta Sizer (Malvern Instruments, Model ZEN360, England). The UV-Visible absorption spectrum was measured using a UV-visible spectrophotometer (Shimdzu, UV-2450). PL measurements were carried out using a spectrofluorimeter (Varian, Cary Eclipse Fluorescence Spectrophotometer).

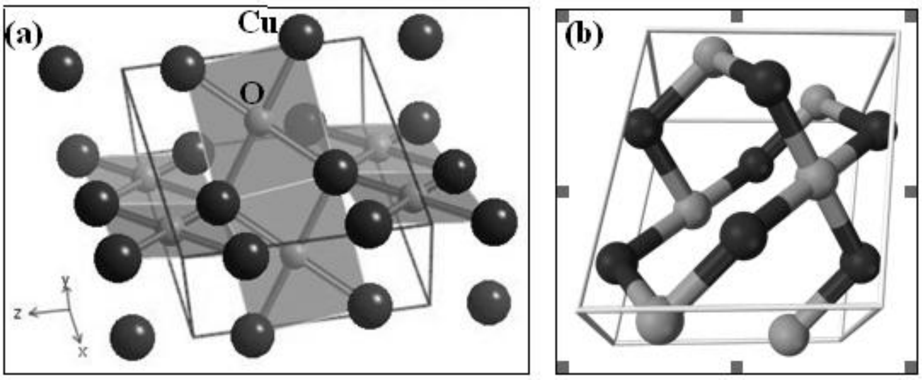

Figure 3.4 Schematic of (a) CuO crystal structure (b) CuO unit cell.

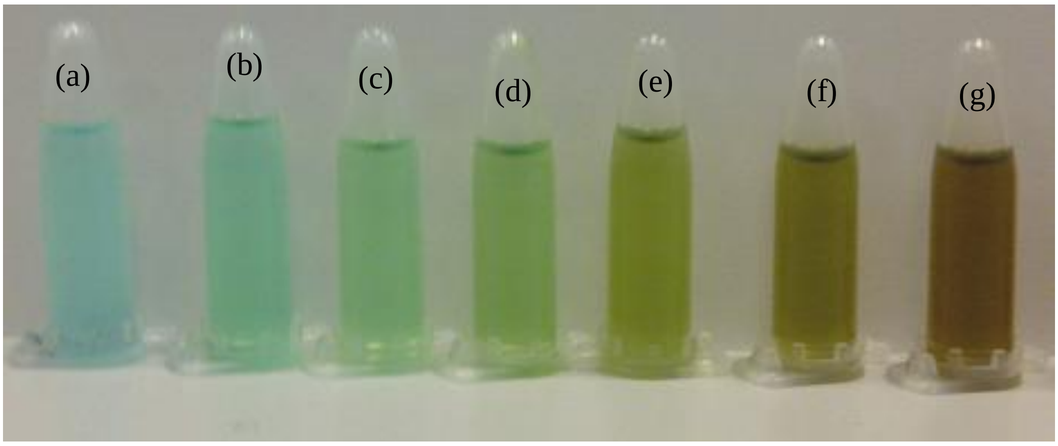

Figure 3.5 Gradual change in solution color during the synthesis stages (a) as precursors dissolved, (b) 3 hour stirring (c) 24 hour aging, (d–g) microwave progress in decreasing CuO NPs size, cycles were repeated 10, 20, 28, 34 times, respectively.

3.1.5 CdS Nanoparticles

The chemicals used to prepare the CdS were cadmium nitrate tetrahydrate ($Cd(NO_3)_2\ 4H_2O$, 98.5%) and sodium sulfide pentahydride ($Na_2S\ 5H_2O$, 98%) which were purchased from Sigma-Aldrich (USA); methanol (99.8%) was purchased from Panreac (Spain). Successive ionic layer adsorption and reaction (SILAR) technique was used to deposit CdS NPs on a substrate. Cadmium (Cd) and sulfur (S) precursors were prepared in advance. 1.54 g ($Cd(NO_3)_2.4H_2O$) and 0.3902 g ($Na_2S.5H_2O$) were each dissolved in 100ml solutions of methanol and distilled water (1:1 v/v). The substrate was dipped into the Cd precursor solution for 1 minute to absorb Cd ions into the substrate which were then rinsed with methanol for 10 seconds to remove loosely bound Cd ions. They were then dipped for another minute into S precursor solution, where S ions reacted with preadsorbed Cd ions to form CdS NPs on the substrate. They were then rinsed again with methanol for 10 seconds to remove unreactive S ions and loosely bound CdS material from the surface of the substrate and to finish the cycle as shown in Figure 3.6. By repeating the cycle many times, the thickness of the CdS NPs layer increased and took on a shiny yellow color.

Other samples of CdS NPs were prepared by mixing the same volume as the two previously prepared Cd and S precursor solutions. The two solutions were mixed via magnetic stirring for 5 minutes at room temperature. A yellow solution was formed, that is evidence of CdS production. CdS NPs were precipitated by centrifugation at 4000rpm for 10 minutes, then washed with distilled water and methanol the first time, and with methanol another two times before being finally dispersed in methanol. Figure 3.7 shows that the crystal structure of CdS is similar to ZnO, which is a hexagonal wartzite structure.

The NP size distribution was determined by a dynamic light scattering (DLS) technique using a Zeta Sizer (Malvern Instruments, Model ZEN360, England). The morphology of the CdS NP layer was visualized by scanning with an electron microscope (SEM, JEOL, JSM- 5600, Japan).

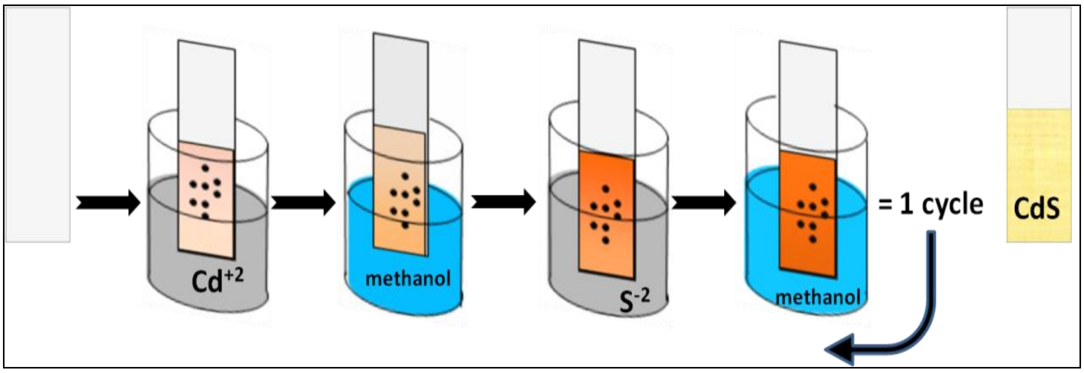

Figure 3.6 Schematic of successive ionic layer adsorption and reaction (SILAR) technique used for deposition of CdS NPs layer.

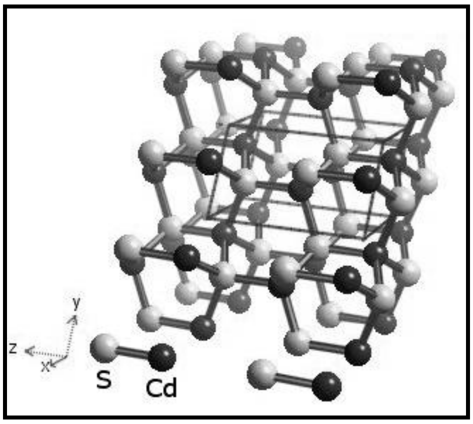

Figure 3.7 Schematic of CdS hexagonal wurtzite crystal structure.

3.1.6 Bi_2S_3 Particles

The chemicals used to prepare Bi_2S_3 were bismuth nitrate tetrahydrate (Bi $(NO_3)_3$ $.4H_2O$, 98.5%) and thioacetamide (CH_3–CS– NH_2, 99%) which were purchased from Sigma-Aldrich (USA). The SILAR technique was used to deposit Bi_2S_3 on the substrate. Bismuth (Bi) and sulfur (S) precursors were prepared in advance: 0.145 g (Bi $(NO_3)_3.4H_2O$) and 0.030 g (CH_3–CS– NH_2) each was dissolved in 100ml of distilled water and kept at 60ºC during the whole SILAR cycle so the reaction can take place. The substrate was dipped into Bi precursor solution for 1 minute to absorb Bi ions into the substrate. It was then rinsed with distilled water for 10 seconds to remove loosely bound Bi ions and then dipped for another minute into S precursor solution, where S ions reacted with preadsorbed Bi ions to form Bi_2S_3 NPs on the substrate. It was then rinsed again with methanol for 10 seconds to remove unreactive S ions and loosely bound Bi_2S_3 material from the surface of the substrate before being dried on a hot plate at 60ºC to finish the cycle as shown in Figure 3.8. By repeating the cycle for a certain number of times, the thickness of the Bi_2S_3 particle layer increased and took on a shiny dark brown color.

Another sample of Bi_2S_3 particles was prepared by mixing the same volume as the two previously prepared Bi and S precursor solutions. The two solutions were mixed with magnetic stirring for 10 minutes at 60ºC. A dark brown solution was formed that is an evidence of Bi_2S_3 production. Bi_2S_3 particles were precipitated by centrifugation at 4000rpm for 10 minutes, then washed with distilled water and methanol the first time before being washed with water two more times and finally dispersed in water. Figure 3.9 shows the orthorhombic crystal structure of Bi_2S_3, each unit cell consist of 4 molecules, with two bismuth atoms and 3 sulfide atoms in each molecule, thus each unit cell consist of 20 atoms.

The particle size distribution was determined by a dynamic light scattering (DLS) technique using a Zeta Sizer (Malvern Instruments, Model ZEN360, England). The morphology of the prepared Bi_2S_3 particle layer was visualized by scanning with an electron microscope (SEM, JEOL, JSM- 5600, Japan).

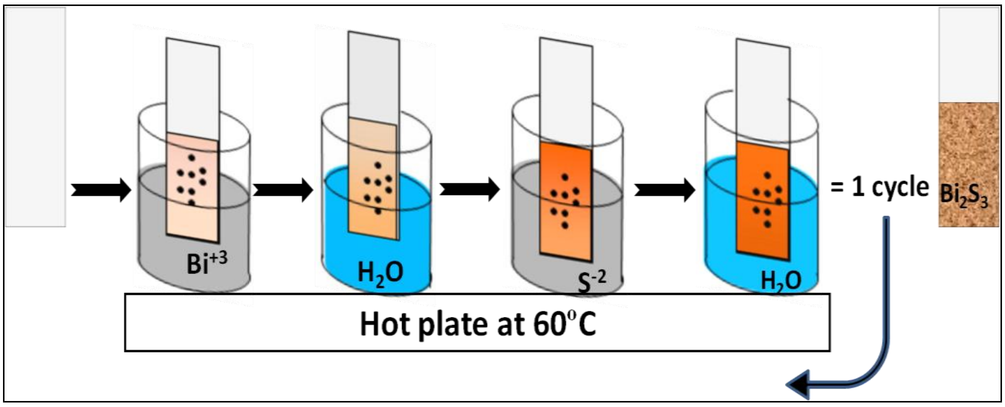

Figure 3.8 Schematic of (SILAR) technique used for deposition of Bi_2S_3 layer.

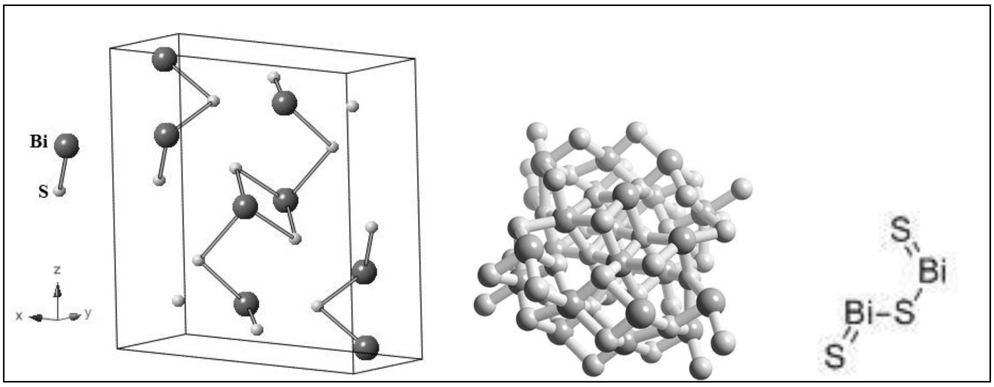

Figure 3.9 Schematic of Bi_2S_3 orthorhombic crystal structure**.**

3.1.7 Reduced GO

Graphene oxide (GO) is a graphene sheet functionalized with oxygen groups in the form of epoxy on the basal plane and other defects that result from oxidation such as hydroxyl groups (OH) that are on the basal plane or at the edges. Carboxyl groups (COOH) at the edges as shown in Figure 3.10 [234, 344]. GO is an insulating material because some of the sp^2 conjugations of the hexagonal graphene lattice were substituted with sp^3 hybridized carbon atoms bonded to oxygen atoms. In order to convert GO from an electrical insulator to a semiconductor, oxygen has to be removed. With an increase in the removal of oxygen atoms GO eventually transforms to a graphene-like semimetal [345] as shown in Figure 3.10.

Reduction of GO can be conducted in several ways such as a chemical process using a hydrazine reagent, which is a toxic chemical reducing agent. In this technique, multiple steps are required and very little reduced GO is produced with a low dispersion concentration [346]. Therefore, the chemical process of GO reduction is inadequate for SC synthesis. Another technique is the solid heating reduction method, where an ultra-high vacuum environment is required while applying heat with a temperatures up to 1050 ºC if under Ar gas, or up to 800 ºC if under H_2 gas [347, 348]. This technique is insufficient for practical applications because the high temperature destroys the solar cell structure.

Therefore, the reduced GO was prepared using a modified method [349] of the thermal chemical process. GO dry platelets was purchased from the Graphene Supermarket, and N,N-dimethyl formamide $(CH_3)_2NC(O)H$, denoted as (DMF), with purity of 99.0% was obtained from Sigma-Aldrich (USA). In summary, 15mg of GO powder was dispersed into a solution of 9ml of DI water and 1ml of DMF. It was magnetically stirred for 48 hours and underwent sonication for 10 minutes, thus a GO aqueous solution was prepared as a coating solution when thermal processing induced a reduction of GO. This will be discussed in SC synthesis section (below). The morphology of the annealed GO layer was visualized by scanning with an electron microscope (SEM, JEOL, JSM-5600, Japan).

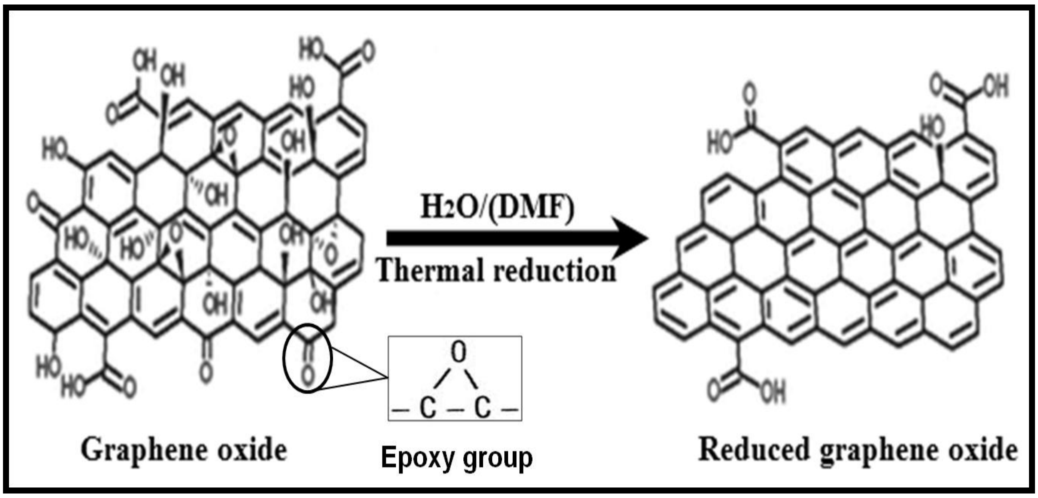

Figure 3.10 Schematic of GO structure (left), and reduced GO by heating (right) [349].

3.1.8 Poly [3,4-ethylenedioxythiophene]-Poly [styrenesulfonate]

Poly[3,4-ethylenedioxythiophene]–poly [styrenesulfonate] (PEDOT:PSS), 1.3 wt % dispersion in H_2O had a PEDOT content of 0.5 wt. % and a PSS content of 0.8 wt. %, with an E_g of 1.6 eV and a conductivity of 1 S/cm. In general, conjugated organic semiconductors are sensitive to higher light energy wavelengths in the presence of oxygen. Therefore, they are applied in a semi-dark glove box with inert gases such as nitrogen or argon, where a yellow filter light can be used. The chemical structure of PEDOT:PSS molecules is represented in Figure 3.11.

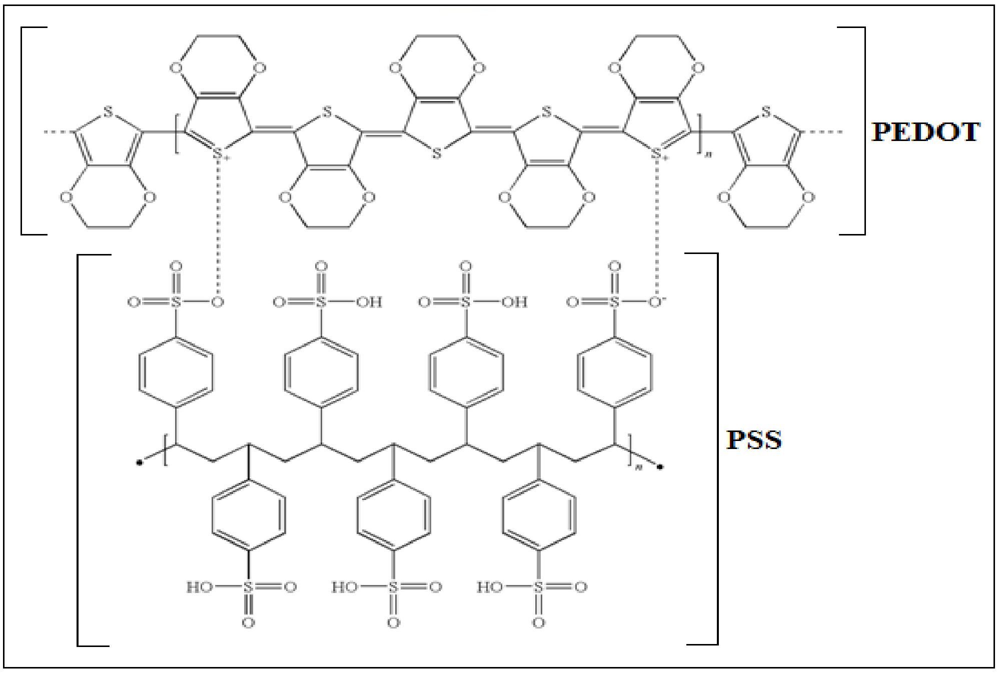

Figure 3.11 Schematic of PEDOT:PSS chemical structure.

3.2 Quantum Dot Solar Cells Fabrication and Characterization

3.2.1 Solar Cell of (ZnO/TiO_2/CdS/PbS/PEDOT:PSS)

Substrate preparation:

The materials used to prepare the n-type substrate were fluorine doped tin oxide (SnO_2/F) which is referred to as (FTO) coated glass and has a thickness of 2.2 mm and a surface resistivity of ~7 Ω/sq. Titanium tetrachloride solution ($TiCl_4$) with a concentration of 1.0M in toluene was purchased from Sigma Aldrich (USA). Toluene (99.8 %) was purchased from TEDIA (USA); methanol (99.8%) and acetone (99.8%) were purchased from Panreac (Spain), and ZnO NPs with an average size of 5.3 nm in water dispersion was synthesized in advance as described in section 3.1.1. To prepare the substrates a slide of FTO coated glass was cut into squares (1cm x 1cm), then cleaned by sonication for 15 minutes in acetone and another 15 minutes in methanol before being finally rinsed in de-ionized water and dried with nitrogen gas (N_2).

The ZnO NPs layer was deposited in a fume hood with good ventilation using a layer-by-layer spin coating deposition method, where a few drops of ZnO water dispersion of 10 mg/ml concentration were added onto the FTO/glass for 30 seconds and spin-coated at 2500 rpm for another 30 seconds each time. The process was repeated twice and the substrates were annealed at 150°C for 30 minutes. In order to form a TiO_2 NP layer, $TiCl_4$ solution was diluted to a 25% concentration in toluene (1ml /4ml), which is yellow. The ZnO substrates were immersed in the $TiCl_4$ solution for 30 minutes and heated at 70°C in an oven.

Then the substrates were taken out of the $TiCl_4$ solution and sintered in an oven or on a hot plate at 520 °C for 30 minutes which partially etches the ZnO. The heated TiO_2 layer looks white, indicating that the sintering process is over. The heating device was left to cool before removing the substrate.

The resulting substrates were used for deposition of the other layers to complete a solar cell structure as shown in the following sections. It is better to use the substrates directly after sintering, otherwise they should be stored in a clean environment and conserved from moisture before heating again at about 450°C before use, to ensure that no moisture or pollutants are left on the TiO_2 (NPs) surface, prior to solar cell fabrication.

CdS (NPs) layer deposition:

A CdS NP layer was deposited using a SILAR cycle technique as described in section 3.1.5. The FTO/ZnO (NPs)/TiO_2 (NPs) substrate was dipped into a Cd precursor solution for 1 minute, rinsed with methanol for 10 seconds, dipped for another minute into S precursor solution and rinsed again with methanol for 10 seconds. Thus one SILAR cycle was completed and CdS NPs were adsorbed in TiO_2 NPs. 11 SILAR cycles were applied and a shiny yellow layer is obtained.

PbS (QDs) layer deposition with ligand exchange:

A PbS QDs layer was applied on top of a CdS NPs layer using the previously synthesized PbS QDs hexane dispersion (see section 3.1.3.) In addition to 1,2-ethanedithiol (EDT, 97%) with the chemical formula $HSCH_2CH_2SH$, acetonitrile (99.9%) was used to perform the ligand exchange.

The PbS QDs layer was deposited in a fume hood with good ventilation using a layer-by-layer spin coating deposition method. EDT/acetonetrile solution was prepared in advance by mixing 0.5 ml EDT with 100ml acetonetrile. First, a few drops of PbS QDs hexane dispersion were added to the surface of the FTO/ ZnO (NPs)/TiO_2 (NPs)/CdS (NPs) structure for 20 seconds each time, and spin-coated at 2500 rpm. During the second step we flood the surface with EDT/acetonetrile solution (0.5:100 v/v) and wait 30 seconds before spinning. In the third step the film is washed with acetonetrile and spun for 3 seconds to dry. Thus one layer of deposition is complete and the PbS QDs are stacked on the CdS NPs. 6 spin-coated layers were applied and a shiny black layer was obtained. Then the device was annealed at 50ºC for 10 minutes. Step 1 was conducted to deposit PbS QDs, whereas steps 2 and 3 were performed to exchange the long ligands, OA which is used in the PbS QDs synthesis process, with the short ligand EDT. The chemical structures of OA and EDT molecules are shown in Figure 3.12. OA molecules are likely to hinder the charge transfer between PbS QDs due to their insulating characteristics. Therefore EDT molecules were applied during the layer-by-layer coating of the PbS QDs to replace the OA molecules. As a result EDT ligand exchange shortens the distance between the PbS QDs, increases carrier mobility, insolubilizes the QDs and reduces the surface oxidation process [350, 351].

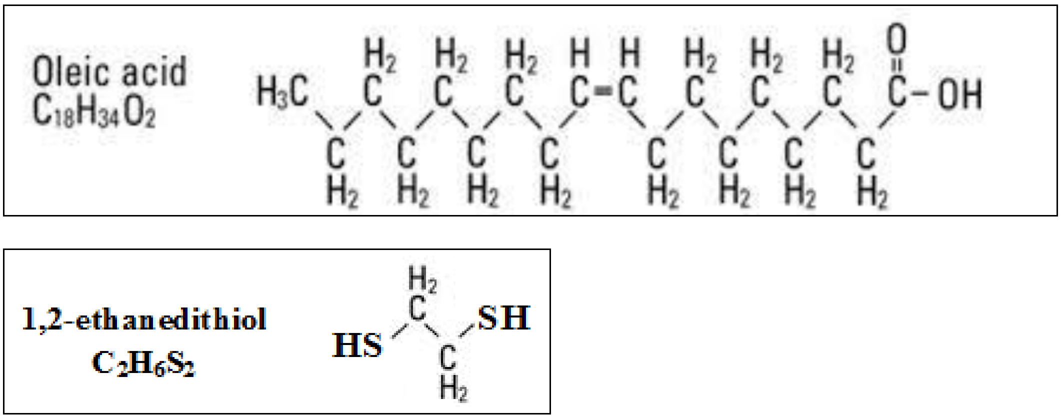

Figure 3.12 Schematic of oleic acid, and 1,2 ethanedithiol chemical structure.

PEDOT:PSS layer deposition:

The PEDOT:PSS solution is without further filtration or dilution. The surface of the PbS QDs layer is flooded with PEDOT:PSS solution for 15 seconds then spin-coated at 2500rpm for 1 minute, after that the device is annealed on a hot plate at 120ºC for 20 minutes to evaporate any residual water. The deposition process and heat treatment are performed in a semi-dark glove box with nitrogen gas.

Metal electrode deposition:

Gold (Au, 99.99%) was purchased from Testbourne Ltd. (England). An Au electrode with ~150nm thickness was deposited on the top of the PEDOT:PSS layer by thermal evaporation in a vacuum using a fine coater (JEOL, JFC-1200, Japan). A shadow mask was used to define a 3x5 array of a 0.785mm^2 circular cell active area.

Solar cell characterization:

- Cell architecture is investigated by visualizing the surface morphology of each layer by scanning with an electron microscope (SEM, JEOL, JSM-5600).

- Cells' PV performance is measured using a solar simulator (Model 71445, New Pot) and Keithley Source Meter (2425) under the illumination of air mass 1.5 global (AM 1.5G) light (100 mW/ cm^2), as shown in Figure 3.13. To insure the accuracy and reduce the error percentage of the results, four similar SCs were synthesized and ten readings were taken for each cell. The average cell efficiency and standard deviations for each cell were calculated.

- The stability of the cells was tested by measuring the PV performance of the cell over a continuous period of 6 weeks under 1sun illumination. The cell was stored in a dark box at room temperature without applying any inert gases and tested in ambient air.

Figure 3.13 The cell under the solar simulator illumination.

Figure 3.14 represents the steps for synthesizing the QDSC with structure (FTO/ZnO/TiO_2/CdS/PbS/PEDOT: PSS/Au). In summary, the ZnO NP water dispersion was spin-coated on the FTO coated glass followed by annealing at 150ºC for 30 minutes then immersion in $TiCl_4$ toluene solution for 30 minutes at 70ºC. This is followed by sintering for another 30 minutes at 520ºC for the formation and calcination of a TiO_2 NPs layer. A CdS NPs layer was deposited using the 11 SILAR method cycles. The PbS QDs layer was deposited by the alternative spin-coating of PbS QDs hexane dispersion and an EDT/ acetonetrile solution for ligand exchange. Then the PEDOT: PSS layer was deposited by spin-coating followed by annealing at 120 ºC for 20 minutes. Finally Au was deposited via thermal evaporation through a shadow mask with circles of 1 ml diameter.

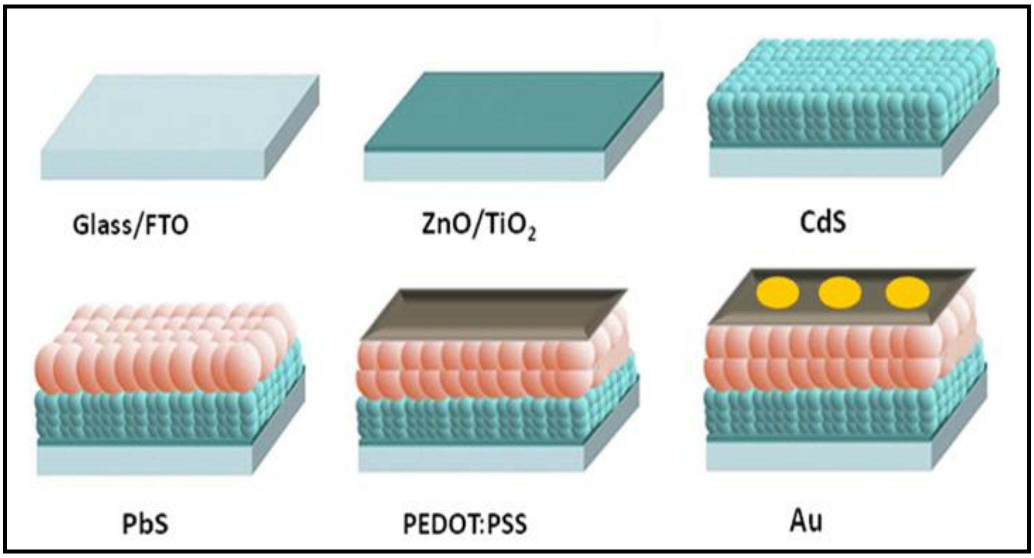

Figure 3.14 Schematic of steps for synthesizing a QDSC.

3.2.2 Employing Different Electron Transport Layers (ETL)

Table 3.1 shows three SCs with various electron transport layers (ETL) that were synthesized using the same procedure described in section 3.2.1 for FTO coated glass preparation, PbS QDs ligand exchange deposition, PEDOT: PSS layer deposition and metal electrode deposition. Except for ETLs changing as: ZnO/TiO_2, TiO_2, and ZnO/TiO_2/GO from cell 1 to cell 3, respectively. Cell 1 has the same structure as shown in section 3.2.1. In cell 2 the TiO_2 NPs layer was deposited on FTO coated glass prior to the CdS NPs deposition. TiO_2 NPs ethanol dispersion was prepared in section 3.1.2 and was spread on the FTO coated glass for 30 seconds and spin-coated at 2500 rpm for 20 seconds to dry before sintering on a hot plate at 450ºC for 30 minutes. Thus, the substrate was ready for CdS NP deposition using 11 SILAR method cycles as described in section 3.2.1. Cell 3 has the same structure as cell 1 and the same synthesis procedure was carried out except for the addition of a GO layer on the FTO/ZnO/TiO_2 substrate before CdS NPs deposition. A few drops of the GO solution were spread on top of the PbS QDs layer for 1 minute then spin-coated at 2500 rpm for 30 seconds followed by heating at 300 ºC for 1 hour on a hot plate in a glove box with an N_2 gas environment in order to reduce the GO layer. Then the PEDOT: PSS layer and Au electrodes were deposited as described previously. The active area of the cells was about 0.785 mm^2. The cell architecture and PV performance were characterized as depicted in section 3.2.1.

Table 3.1 Structure of heterojunction QDSCs with various electron transport layers (ETL)

Cell	Structure	ETL	AL	HTL
1	FTO/ZnO/TiO_2/CdS/PbS/PEDOT:PSS/Au	ZnO/TiO_2	CdS/PbS	PEDOT:PSS
2	FTO/TiO_2/CdS/PbS/PEDOT:PSS/Au	TiO_2	CdS/PbS	PEDOT:PSS
3	FTO/ZnO/TiO_2/GO/CdS/PbS/PEDOT:PSS /Au	ZnO/TiO_2/GO	CdS/PbS	PEDOT:PSS

3.2.3 Employing Different Active Layers (AL)

Table 3.2 shows SCs with various active layers (AL) that were synthesized using the same procedure described in section 3.2.1 for FTO coated glass preparation, PbS QDs ligand exchange deposition, PEDOT: PSS layer deposition and metal electrode deposition. This is except for AL changing as: CdS/PbS, Bi_2S_3/CdS/PbS and Bi_2S_3/PbS from cell 1 to cell 3, respectively. Cell 1 has the same structure as shown in section 3.2.1. Cell 2 has the same structure asf cell 1 and the same synthesis procedure was carried out except for the addition of a Bi_2S_3 layer on the FTO/ZnO/TiO_2 substrate before the CdS NPs deposition. Bi_2S_3 particles were deposited using 11 SILAR method cycles as described in section 3.1.6. Cell 3 has the same structure as cell 1 except a Bi_2S_3 particle layer was applied instead of a CdS NPs layer. Bi_2S_3 particles were deposited using 11 SILAR method cycles. The active area of the cells was about 0.785mm^2. The cell architecture and PV performance were characterized as depicted in section 3.2.1.

Table 3.2 Structure of heterojunction QDSCs with various active layers (AL)

Cell	Structure	ETL	AL	HTL
1	FTO/ZnO/TiO_2/CdS/PbS/PEDOT:PSS/Au	ZnO/TiO_2	CdS/PbS	PEDOT:PSS
2	FTO/ZnO/TiO_2/Bi_2S_3/CdS/PbS/PEDOT:PSS /Au	ZnO/TiO_2	Bi_2S_3/CdS /PbS	PEDOT:PSS
3	FTO/ZnO/TiO_2/Bi_2S_3/PbS/PEDOT:PSS/Au	ZnO/TiO_2	Bi_2S_3/PbS	PEDOT:PSS

3.2.4 Employing Different Hole Transport Layers (HTL)

Table 2.3 shows five SCs with various hole transport layers (HTL) that were synthesized using the same procedure described in section 3.2.1 for substrate preparation, CdS NPs deposition, PbS QDs ligand exchange deposition and metal electrode deposition; except for the HTLs changing as: PEDOT: PSS, GO/PEDOT: PSS, GO, CuO and without HTL from cell 1 to cell 5, respectively. Cell 1 has the same structure as shown in section 3.2.1. In cell 2 a GO NPs layer wase deposited prior to PEDOT: PSS deposition, where a GO solution was prepared in advance as described in section 3.1.6. In summary, 15mg of GO powder was dispersed into a solution of 9ml of DI water and 1ml of DMF using magnetic stirring for 48 hours and sonication for 10 minutes. A few drops of GO solution were spread on top of a PbS QDs layer for 1 minute then spin coated at 2500rpm for 30 seconds followed by heating at 150ºC for 1 hour on a hot plate in a glove box with an N_2 gas environment. Then the PEDOT: PSS layer and Au electrodes were deposited as described previously. Cell 3 has the same structure as cell 2 except for the absence of a PEDOT: PSS layer. In cell 4 a CuO NP was used as an HTL instead of a GO or PEDOT: PSS layer. A CuO NP with an average size of 5nm DMF dispersion was prepared in advance as described in section 3.1.3. A few drops of CuO solution were spread on top of a PbS QDs layer for 1 minute then spin-coated at 2500rpm for 30 seconds, followed by heating at 50ºC for 20 minutes on a hot plate prior to Au electrode deposition. In cell 5 no HTL was applied since the Au layer was deposited directly onto the PbS QDs layer. The active area of each cell was about 0.785mm^2. The cell architecture and photovoltaic performance can be characterized as depicted in section 3.2.1.

Table 3.3 Structure of heterojunction QDSCs with various hole transport layers (HTL).

Cell	Structure	ETL	AL	HTL
1	FTO/ZnO/TiO_2/CdS/PbS/PEDOT:PSS/Au	ZnO/TiO_2	CdS/PbS	PEDOT:PSS
2	FTO/TiO_2/CdS/PbS/ GO/PEDOT:PSS/Au	ZnO/TiO_2	CdS/PbS	GO/PEDOT:PSS
3	FTO/ZnO/TiO_2/ /CdS/PbS/ GO/Au	ZnO/TiO_2	CdS/PbS	GO
4	FTO/ZnO/TiO_2/CdS/PbS/CuO/Au	ZnO/TiO_2	CdS/PbS	CuO
5	FTO/ZnO/TiO_2/CdS/PbS/Au	ZnO/TiO_2	CdS/PbS	None

3.2.5 Employing Different Active Layer Thicknesses

Table 3.4 shows five SCs with different active layer thicknesses that were synthesized using the same procedure as described in section 3.2.1, for substrate preparation, PEDOT: PSS layer deposition and metal electrode deposition. The same techniques were applied for CdS NPs and PbS QDs deposition, except for CdS NPs and PbS QDs layer thicknesses changing: CdS(11)/ PbS(6), CdS(6)/ PbS(6), CdS(0)/ PbS(6), CdS(11)/ Blend(2)/ PbS(4) and CdS(11)/ Blend(4)/ PbS(4) from cell 1 to cell 5, respectively. The number next to the CdS indicates the number of SILAR cycles. The number next to the PbS indicates the numbrt of repetitions of the spin-coating process and the number next to the blend indicates the times a blend layer, which consist of CdS NPs and PbS QDs, was applied. This will be described later in this section.

Cell 1 has the same structure as shown in section 3.2.1. Cell 2 has the same structure as cell 1 except 6 SILAR cycles were applied to deposit CdS NPs instead of 11 cycles. In cell 3 no CdS NPs layer was applied, since 6 spin-coated layers of PbS QDs were deposited directly onto the TiO_2 layer.

Cells 4 and 5 comprise a trilayer structure, where the blend layer of CdS NPs as an n-type material and PbS QDs as a p-type material are sandwiched between CdS and PbS layers. The blend layer was added to enhance the interfacial contact between the CdS NPs and PbS QDs as it is supposed to provide more surface area for charge transfer. The cells with trilayer structure were synthesized as follow: (i) the substrates were prepared and 11 SILAR cycles were applied for CdS NPs deposition as described in section 3.2.1; (ii) a few drops of PbS QDs hexane dispersion were added for 10 seconds and spin-coated at 2500rpm followed by flooding the surface with EDT for 15 minutes then rinsing with acetonetrile; (iii) Cd and S precursor solutions were prepared in advance as described in section 3.1.4. a few drops of Cd precursor solution were added for 1minute then spin-coated at 2500rpm to absorb Cd ions on the surface. Then methanol was added and spin-coated at 2500rpm to remove loosely bound Cd ions. Next a few drops of S precursor solution were added for 1minute then spin-coated at 2500rpm so that S ions could react with pre-absorbed Cd ions to form CdS NPs on the PbS QDs. Methanol was again added and spin-coated at 2500rpm in order to remove unreactive S ions and loosely bound CdS material from the surface to finish one deposition. This CdS NP deposition process was repeated one more time. The two steps (ii) and (iii) indicated the formation of a blend layer (iv); steps (ii) and (iii) were repeated to increase the thickness of the blend layer.

Thus, the steps for blend layer formation were repeated twice; (v) PbS QDs ligand exchange deposition, PEDOT: PSS layer deposition and metal electrode deposition, using the same procedure described in section 3.2.1 except for 4 spin coated layers of PbS QDs instead of 6, were applied. Cell 5 is similar to cell 4 but the thickness of the blend layer was duplicated by repeating steps ii and iii four times instead of twice. The active area of the cells was about 0.785mm^2. The cell architecture and PV performance can be characterized as depicted in section 3.2.1.

Table 3.4 Structure of QDSCs with different AL (CdS/PbS) thickness.

Cell	Structure	CdS	PbS	Blend
1	FTO/ZnO/TiO_2/CdS(11)/PbS(6)/PEDOT:PSS/Au	11	6	0
2	FTO/ZnO/TiO_2/CdS(6)/PbS(6)/PEDOT:PSS/Au	6	6	0
3	FTO/ZnO/TiO_2/ PbS/ PEDOT:PSS /Au	0	6	0
4	FTO/ZnO/TiO_2/CdS(11)/Blend(2)/PbS(4)/PEDOT :PSS/Au	11	4	2
5	FTO/ZnO/TiO_2/CdS(11)/Blend(4)/PbS(4)/PEDOT :PSS/Au	11	4	4

CHAPTER FOUR

RESULTS AND DISCUSSION: PERFORMANCE OF QDSCs

The primary objective of the present study is to enhance the optoelectronic properties of the QDs by bandgap engineering and controlling the particle size utilized in a novel solar cell structure with optimized structure and thickness to enhance solar cell performance. The results are organized such that the charectrization of the synthesized QDs is presented first then the performance of the SCs is presented.

4.1 Quantum Dots Characterization

4.1.1 ZnO Nanoparticles

Morphology and size distribution:

Figure 4.1 represents the size histograms of ZnO NPs dispersed in ethanol produced by different concentrations of NaOH, varying from 0.91 to 7.27mmol as measured by a Zeta sizer. The figure shows that, in general, as NaOH concentration increases, the particle size decreases with a minimum average size of 5.3nm at 3.18mmol. Abnormal increases in NP size are noticed at 7.27mmol. The particle size distribution graphs for all NaOH concentrations are narrow. The results showing average NP size are summarized in Table 4.1. They show that ZnO nanoparticle size can be controlled by controlling NaOH concentration. Figure 4.2 shows an SEM image of ZnO NPs prepared using a 3.62mmol concentration of NaOH. The figure confirms the formation of the nanoparticles. Most of the particles show an approximately spherical shape. The figure depicts an average size of less than 20nm, which is consistent with the size determined using a Zeta sizer. The image reveals that the ZnO NPs are somewhat agglomerated. To delay the agglomeration rate, the particles were washed and re-suspended in another alcohol medium, or in water that can be used for biological applications.

Table 4.3 ZnO NPs average size and their E_g, prepared using different reactant concentrations.

NaOH (mmol)	Size (nm)	NaOH/ $Zn(CH_3COO)_2.2H_2O$ Weight%	UV absorption peak (nm)	E_g (eV)
0.91	65.0	9.13	368	3.36
1.81	12.6	18.26	338	3.67
2.27	10.7	24.69	330	3.76
2.72	8.5	27.39	325	3.81
3.18	5.3	31.96	318	3.90
3.62	14.0	36.53	339	3.66
7.27	1548	73.06	375	3.31

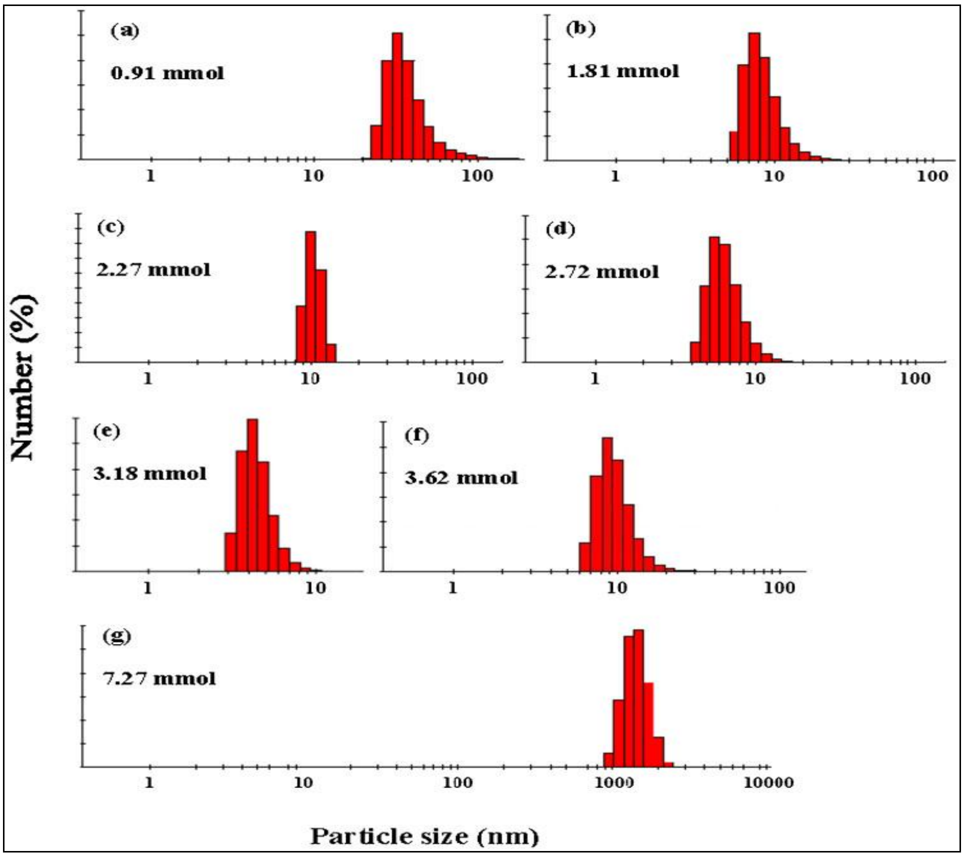

Figure 4.1 Size distribution histograms of ZnO particles dispersed in ethanol, prepared using NaOH concentrations of: (a) 0.91 mmol (b) 1.81 mmol (c) 2.27 mmol (d) 2.72 mmol (e) 3.18 mmol (f) 3.62 mmol (g) 7.27 mmol.

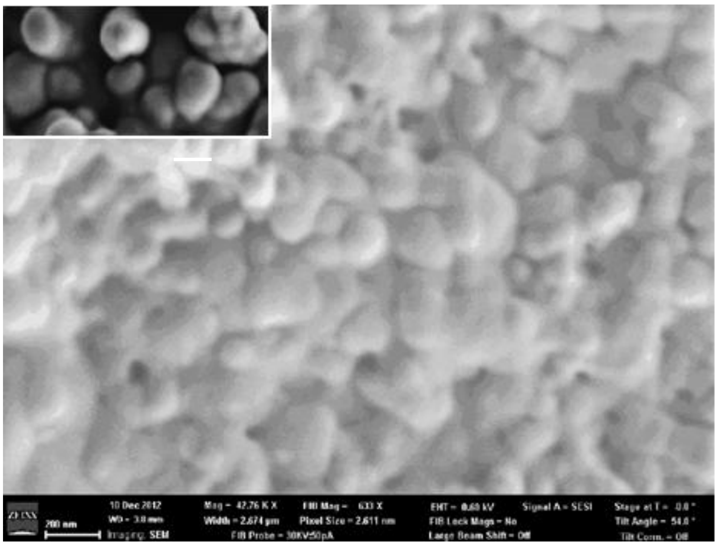

Figure 4.2 SEM image of ZnO NPs prepared using NaOH concentration of 3.62mmol.

UV-Vis absorption spectra

Each material has its own characteristic UV-Vis absorption spectrum which is essentially dependent on the particle size of the material. Figure 4.3 represents the UV-Vis absorption spectra for colloidal ZnO NPs in ethanol. The peak is located at about 210 nm and is noticed for all the spectra and shows evidence for the existence of small sized particles of less than Bohr's radius for ZnO (1.8 nm) [352]. The absorption peaks of 368, 338, 330 and 325nm are noticed for the spectra of nanoparticles with average sizes of 65.0, 12.6, 10.7 and 8.5 nm, respectively. Those peaks can be attributed to the bandgap transition of ZnO nanoparticles, which is known as excitonic absorption; They are blue shifted from excitonic absorption of the bulk ZnO at 375 nm (E_g = 3.31 eV) at room temperature [91, 353]. It is obvious from the black line which crosses all the spectra that the smaller the particles are, the more excitonic absorption blue shift occurs, as depicted in Figure 4.3. This is due to an increase in the particles bandgap due to the increase in structural quality and quantum confinement (QC) effects. The 5.3 nm NPs (Figure 4. 3e) exhibit the lowest excitonic absorption peak at 318nm (highest blue shift). The absorption spectrum in Figure 4f exhibits two excitonic absorption peaks at 228nm that can be attributed to the presence of particles with sizes less than 5.3 nm and another weak peak at 339 nm related to particles of about 14.0 nm in size. In addition, Figure 4f shows an excitonic absorption peak at 375 nm, which is both broad and weak due to large particle size being similar to bulk.

The absorption spectra of the colloidal NPs can be used to estimate the E_g of spherical NPs through the effective mass model equation (4.1) [354]:

$$E_{g(nano)} = E_{g(bulk)} + \frac{h^2}{8em_0r^2}\left(\frac{1}{m_e} + \frac{1}{m_h}\right) - \frac{1.8e^2}{4\pi\varepsilon\varepsilon_0 r} \qquad (4.1)$$

Where $E_{g(nano)}$ and $E_{g(bulk)}$ are the bandgap energies associated with NPs and bulk material, h is Plank's constant, r is the particle radius, m_e is the electron effective mass, m_h is the hole effective mass, m_0 is free electron mass, e is the charge of the electron, ε is the relative dielectric permittivity, and ε_0 is the dielectric permittivity of free space. The coulomb interaction term is included in equation 1, while the polarization term is neglected.

For bulk ZnO: E_g=3.3 eV, h = 6.626x10^{-34} J s, e = 1.602x10^{-19} C, ε_0 = 8.854x10^{-12} $C^2/N/m^2$, m_0 = 9.110x10^{-31} kg, ε = 8.5, m_e = 0.26, m_h= 0.59 [87, 340], where E_g is calculated from:

$$E_g = \frac{h\,c}{\lambda} \qquad (4.2)$$

Here, c = 2.998x10^8 m/s and $\lambda_{(bulk)}$ = 375 nm.

The average ZnO NP size can be calculated through the effective mass model equation (4.1) using the absorption spectrum. The resulting values are accurate for ideal spherical particles of sizes less than 6nm, where E_g enlargement effects are predominant [341]. Equation 4.1 is valid for λ less than 390nm, unless a negative square radical is attained.

The excitonic absorption peak values shown in Figure 4.3 were used to estimate E_g (in equation 4.2) for each nanoparticle size, and the results are shown in Table 4.1. The inverse relationship between particle size and E_g can be concluded from the results. The E_g value from the spectrum in Figure 4.3e was used in equation 4.2 and produced r of 1.5 nm (i.e. particle size = 3.0nm) which is close to the measured size of 5.3nm. The difference between the two values might be due to some elongation in the shape of the particles. In addition, it is well known that DLS technique usually slightly overestimates particle size when compared to other techniques, as the solvent layers linked to the particle surfaces become more dominant as the particle size decreases to the nanoscale [355].

Photoluminescence (PL) Spectra

Figure 4.4 shows the PL spectra of ZnO NPs in ethanol at room temperature. All spectra exhibit broad visible emissions, which are known as deep band emissions in the range of 425 to 725nm. Two visible emission peaks can be observed: the first one is wide and located at around 541 to 555nm, while the second peak is sharp and centered between 683 to 723nm. The origin of the visible emission of ZnO NPs has been investigated by many researchers and attributed to deep level emission bands. The blue fluorescence band (450–495nm) originated from zinc interstitials [356-358]. The green fluorescence band (495–570 nm) can be attributed to the singly ionized oxygen vacancies and zinc interstitials, due to the recombination between photogenerated holes and singly ionized oxygen vacancies [359-364]. However, other researchers attribute green fluorescence bands to the presence of oxygen and zinc vacancies together [365, 366]. The yellow fluorescence band (570–590nm) might be due to oxygen interstitials [84, 85], or is generated by OH groups on the surface [363]. The orange and red fluorescence band (590–750 nm) results from oxygen vacancies and zinc interstitials in ZnO lattices [358-361].

It is noticeable that the spectra in Figures 4.4b, 4.4c, and 4.4f exhibit a red shift and a lack of UV emissions which is known as a near band-edge emission. However, the spectra in Figurs 4.4d and 4.4e exhibit an obvious blue shift, and weak sharp UV emission peaks centered at 366 and 362nm, respectively, which can be attributed to both Zn interstitials and quantum-confinement effects. The near band-edge emission is attributed to emissions originating from the recombination of electrons and holes on ZnO free excitons which are very sensitive to particle size: the smaller the particles, the shorter the wavelength emission. Table 4.2 summarizes the emission wavelengths for different samples of ZnO NPs. Their excitation wavelengths are displayed in Figure 4.4.

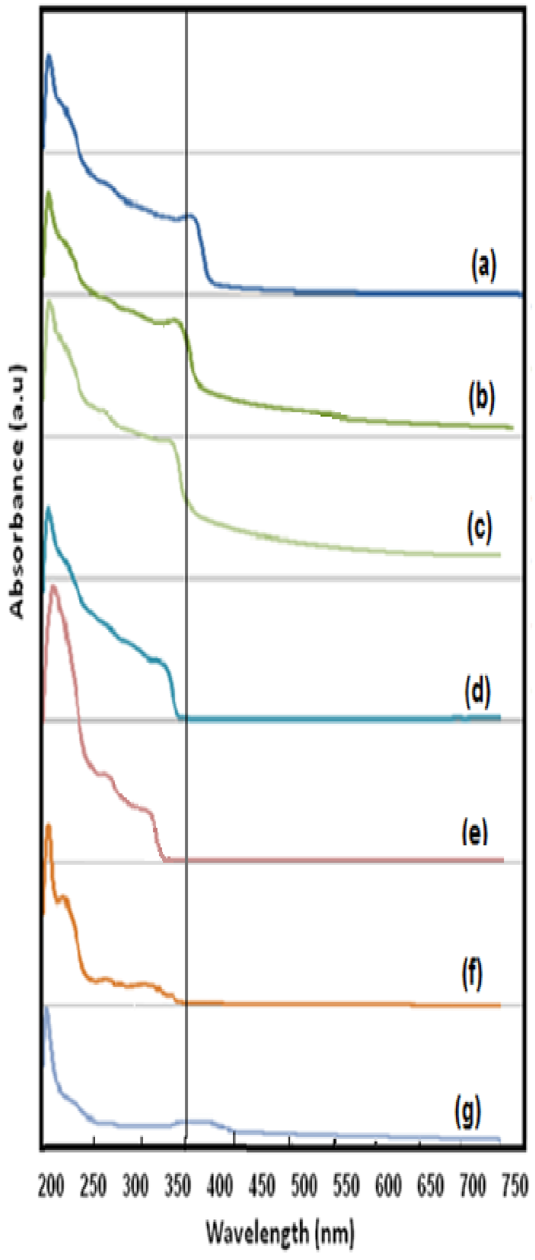

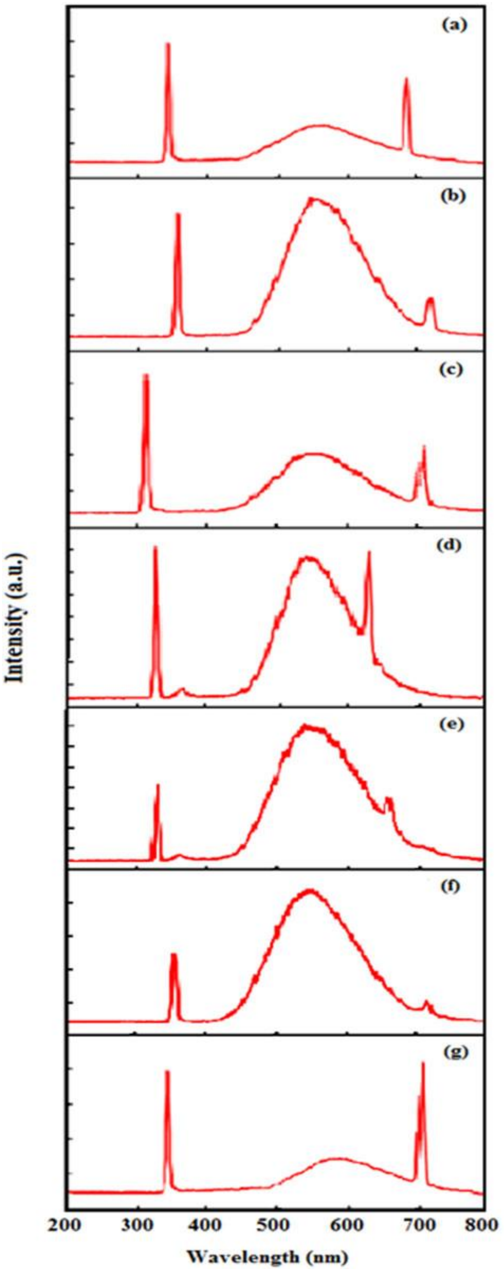

Figure 4.3 UV-vis absorption spectra of ZnO NPs in ethanol with NaOH concentration (a) 0.91mmol, (b) 1.82mmol, (c) 2.27mmol, (d) 2.73mmol, (e) 3.18mmol, (f) 3.64mmol, (g) 7.27mmol.

Figure 4.4 Photoluminescence spectra of ethanol dispersed ZnO NPs at room temperature of size about (a) 65.0nm (b) 12.6nm (c) 10.7nm (d) 8.5nm (e) 5.3nm (f) 14.0nm (g) 1548nm.

Table 4.4 Emission peaks of ZnO NPs with different size.

Size(nm)	Excitation wavelength (nm)	Visible emission first peak center (nm)	Visible emission second peak center (nm)	UV emission peak (nm)
65.0	342	555	683	
12.6	359	552	718	
10.7	315	550	710	
8.5	330	548	647	366
5.3	328	541	654	362
14.0	357	548	714	
1548	350	555	700	

ZnO NPs samples were exposed to UV lamps of 365nm wavelength. Every sample showed clear yellow light emissions with little variation in the degree of color from one sample to another. Figure 4.5 shows the emissions of ZnO NPs of 5.3nm in ethanol at room temperature. As they were prepared in ambient air under visible light the particles appear transparent. The particles exhibit yellow emissions under UV illumination as shown in Figure 4.5b. This, in turn, means that ZnO NPs have defects associated with non-radiative recombination. In order to understand the origin of the visible yellow emission, a beaker of ZnO NPs in ethanol was observed under UV illumination at room temperature under an N_2 environment (Figure 4.5c). It was noticed that the yellow emissions vanished gradually until they completely disappeared. For instance, the visible emission returned to its original state as the sample was exposed to the ambient air as shown in Figure 4.5d.

The yellow emission, shown in Figure 4.5b in the absence of N_2 gas, reveals the existence of some native defects such as oxygen vacancies and zinc vacancies in the ZnO NPs. The former defects are known to introduce deep donor states in the gap, whereas the latter defects can induce shallow accepter states. Consequently, these defects can assist electronic transition with yellow-light emissions. Nitrogen bubbling is expected to produce nitrogen-molecule antisites $(N_2)_O$, which do two things [367]: (i) fill the oxygen vacancies and passivate the dangling bonds and thus eliminate the deep donor states in the gap; and (ii) form double shallow-donor states. Both of these effects stop the yellow emission and activate blue-violet emissions. This latter emission becomes predominant and, in turn, reveals the existence of donor states due to Zn interstitials and acceptor states due to N_2 doping. Finally, by stopping N_2 bubbling and opening the cap to the atmosphere, oxygen dominates the bond to the Zn interstitials and Zn anti-sites. Oxygen has the ability to replace nitrogen, especially as oxygen has greater electronegativity than nitrogen ($\chi_O = 3.44$, $\chi_N = 3.04$ in Pauling units [368]). Then we can go back to the behavior of ZnO NPs with native defects yielding yellow emissions.

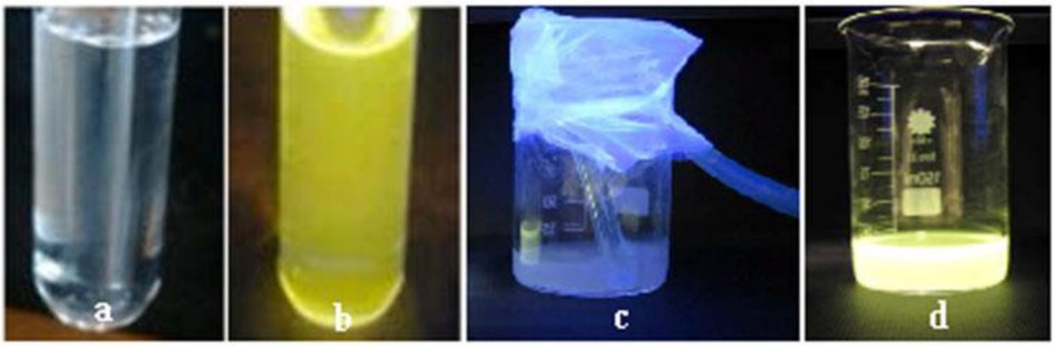

Figure 4.5 ZnO NPs in ethanol (a) under visible light and (b–d) all under UV illumination (365 nm), as prepared, N_2 bubbling, stop N_2 bubbling while opening cap, respectively.

4.1.2 PbS Quantum Dots

Figure 4.6 shows SEM images of PbS QDs agglomerated as crystals on a carbon-coated copper grid. Figure 4.7 shows the size distribution histogram of colloidal PbS QDs hexane dispersion. It is clear that it has a narrow size with a previously reported exciton Bohr radius of PbS (18 nm) [369], so the electron confinement effect was dominant.

Figure 4.8 shows the colloidal PbS QDs absorption within the IR wavelength region, the maximum absorption peak at 912nm can be attributed to the exciton absorption of PbS QDs and the two weak peaks at 720nm and 1020nm correspond to the existence of smaller and larger PbS QDs, respectively. The absorption peaks are blue shifted compared to the bulk PbS because the energy gap (E_g) increases as the particles size decreases due to confinement. The optical bandgap of PbS QDs is calculated from the absorption peak using equation 4.3 [369].

$$(\alpha h\nu)^n = B\,(h\nu - E_g) \qquad (4.3)$$

Where α is the absorption coefficient in cm^{-1}, B is a constant related to the material, $h\nu$ is the photon energy in eV, *h* is Plank's constant ($6.626x10^{-34}$), ν is the frequency of the photon, E_g is the optical bandgap in eV, n is the exponent that can take a value of 2 for a direct transition or 1/2 for an indirect transition.

The absorption coefficient α was calculated from:

$$\alpha d = \ln(1/T) \qquad (4.4)$$

Where d stands for the path length of the wave in cm and was set equal to the cuvette length of 1cm, T is the transmittance which was calculated from the measured absorbance (A_λ) at a certain wavelength of light (λ) using [370]:

$$A_\lambda = -\log_{10}(T) \qquad (4.5)$$

Figure 4.9 represents $(\alpha h\nu)^2$ versus $h\nu$ plots of absorption spectra for the PbS QDs. The energy bandgap for the PbS QDs is estimated by fitting a straight line to the linear portion of the curve. The E_g value should be obtained from the interception of the hν- axis. The Eg value for PbS QDs is 1.36 eV which is much larger than the bulk (0.41 eV) [371]. The increase in the direct bandgap values (a blue shift) of PbS QDs with the decrease in NPs size is associated with the electron confinement effect as a result of the reduction in particle size to the nanoscale.

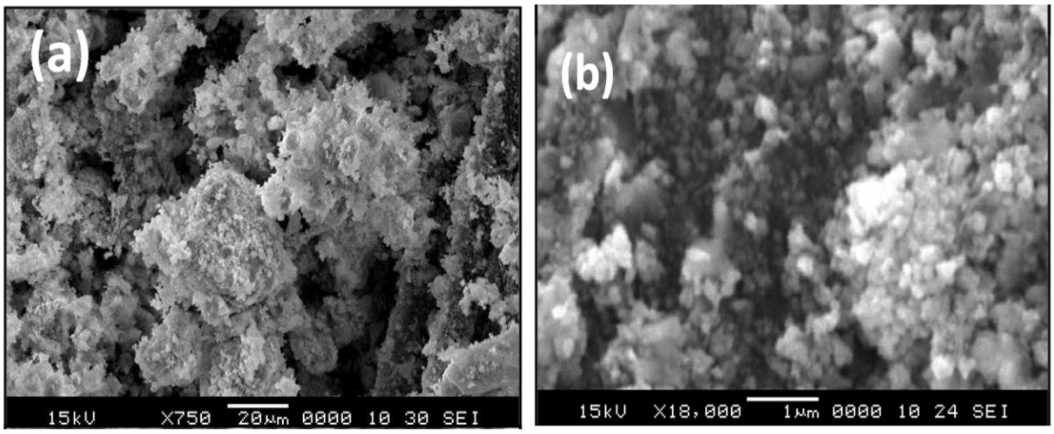

Figure 4.6 SEM images of agglomerates of PbS QDs.

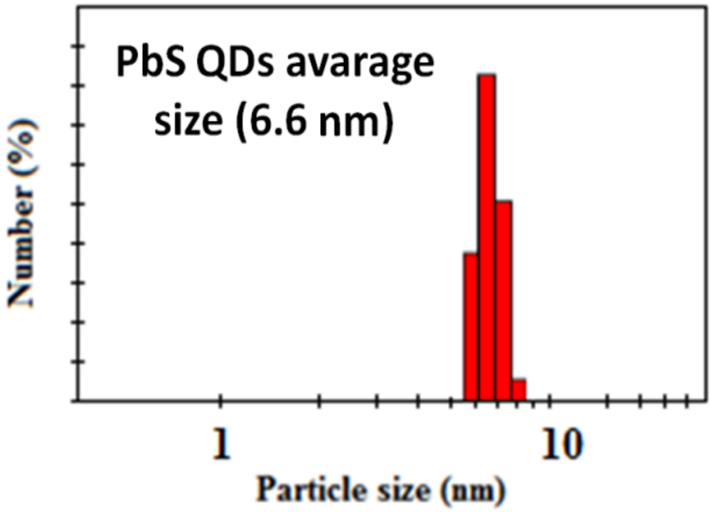

Figure 4.7 Size distribution histograms of colloidal PbS QDs, dispersed in hexane.

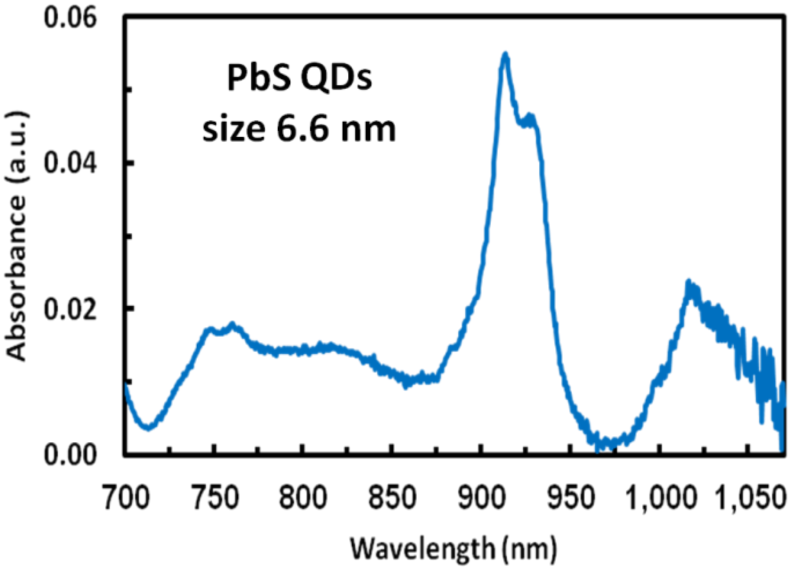

Figure 4.8 UV-Visible absorption spectra of colloidal PbS QDs, dispersed in hexane.

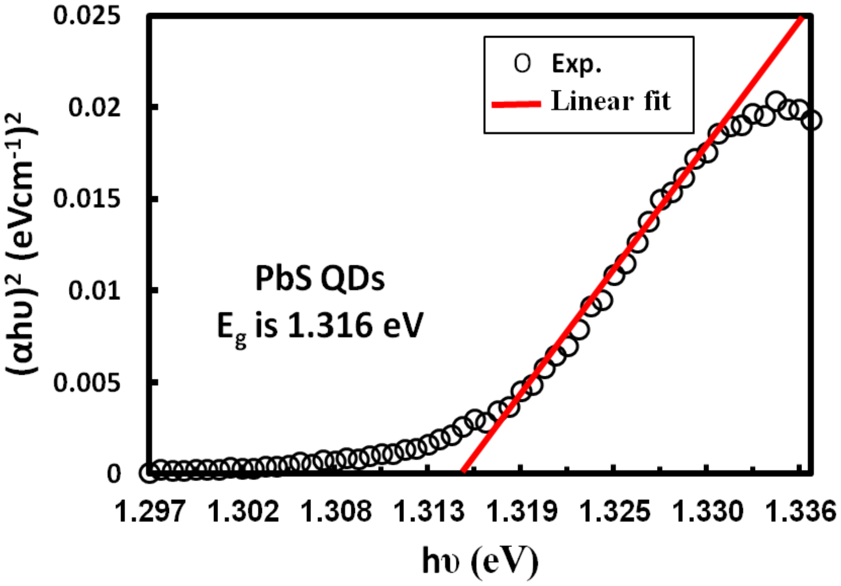

Figure 4.9 Direct bandgap estimations of PbS QDs with average size 6.6nm.

4.1.3 CuO Nanoparticles

Morphology and size distribution

Figure 4.10 shows SEM images of CuO NPs agglomerated in spherical shape crystals on a carbon-coated copper grid. The resolution limit of the SEM prohibits distinguishing individual CuO. Thus, the size of the NPs assembled into spheres can not be estimated from the observed image. Figure 4.11 shows TEM images of CuO NPs prepared by repeating the microwave cycle 30 times. The synthesized CuO NPs are crystalline and have approximately spherical shapes, as observed in the high resolution images. The average NPs size is about 4.4nm.

Figure 4.12 shows size distribution histograms for representative samples of colloidal CuO NPs with variable repeated cycles of on/off microwave heating procedures as measured using a Zeta Sizer. Figures 4.12 (a–g) show that CuO NPs have average sizes of 10.1, 6.9, 5.0, 4.4, 3.4, 2.5 and 1.2 nm for microwave repeating cycles of 20, 24, 28, 30, 32, 34 and 36 times, respectively. The figures also show that all the size distributions have narrow size distribution, and NPs become smaller with an increase in the number of microwave radiation cycles. Figure 4.12d shows that CuO NPs produced by repeating the microwave cycle 30 times have an average size of 4.4nm, which is in agreement with the measurements obtained from the TEM images (Figure 4.11).

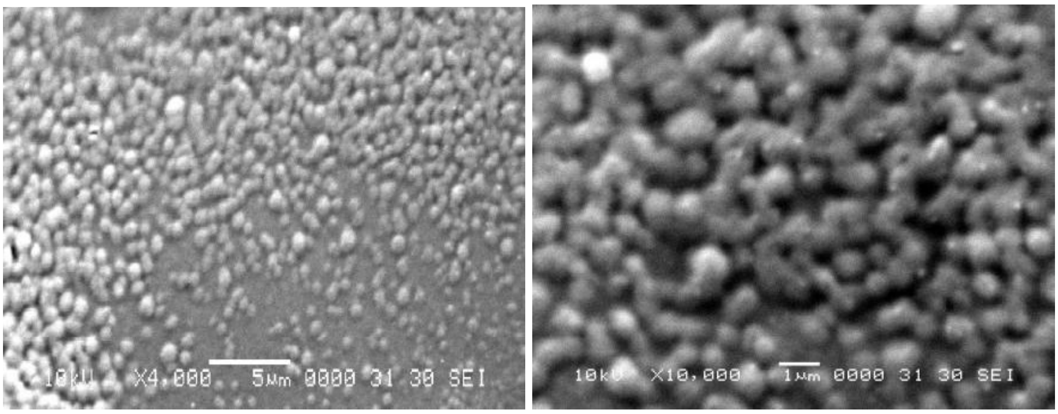

Figure 4.10 SEM images of agglomerates of CuO NPs.

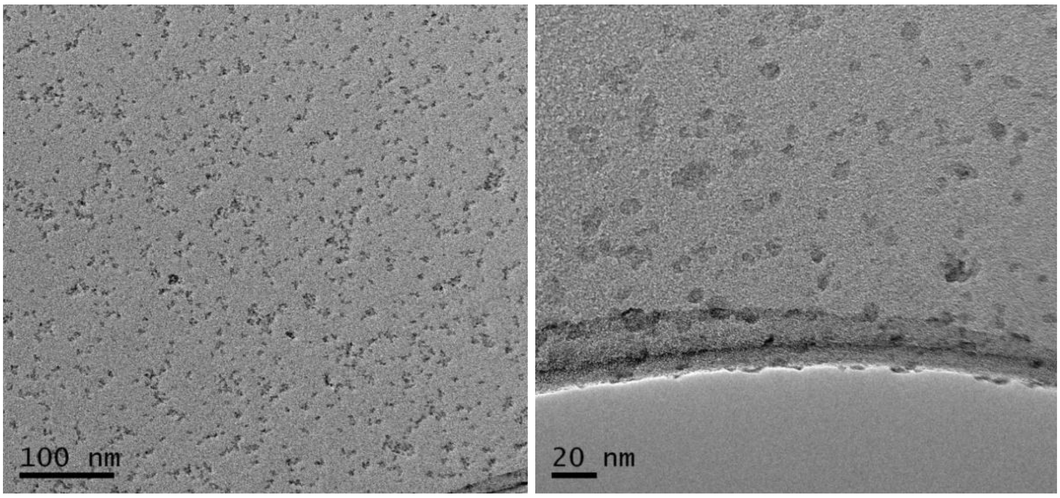

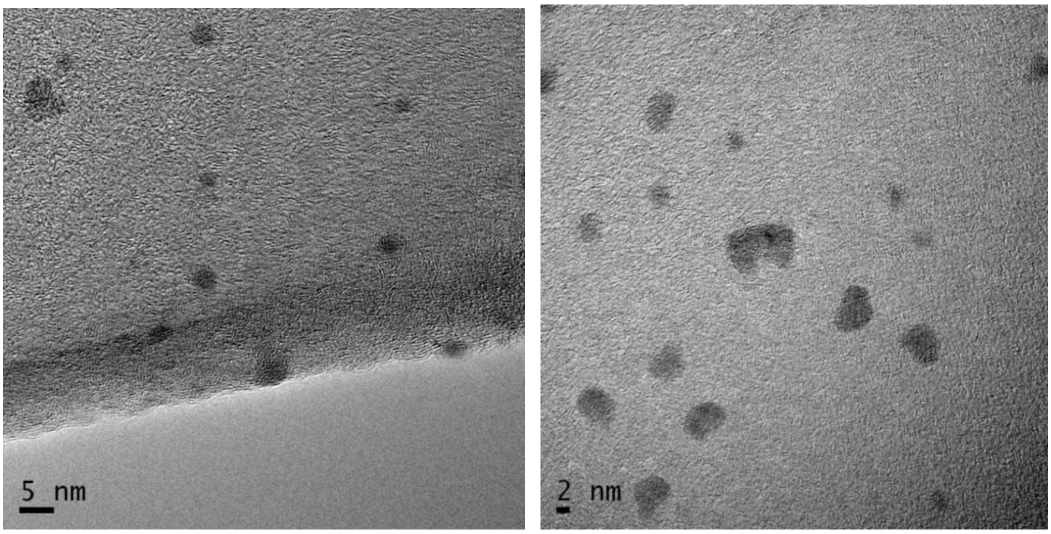

Figure 4.11 TEM images of CuO NPs.

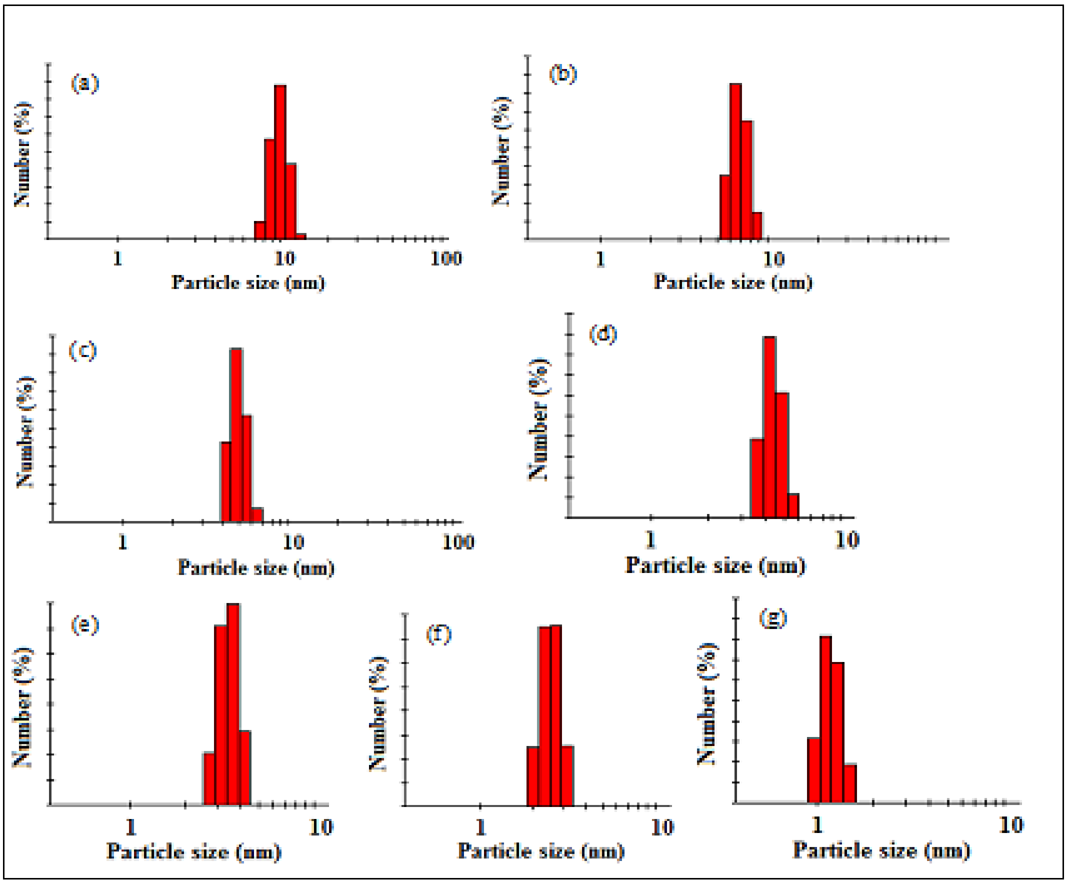

Figure 4.12 Size distribution histograms of colloidal CuO NPs, dispersed in DMF.

UV–visible absorption spectra and energy gap calculation

Figure 4.13 shows the UV-visible absorption spectra of colloidal CuO NPs with average NPs sizes of 10.1, 5.0 and 1.2 nm. The figure depicts absorption peaks at about 290, 270 and 255 nm for the three samples, respectively. The sizes of these NPs are smaller than the previously reported exciton Bohr radius for CuO, between 6.6 and 28.7 nm [372]. The peak are blue shifted compared to bulk CuO with direct band transitions of about 3.25 ± 0.05 eV [373]. The blue shift in the optical absorption spectra with particle size reduction is a clear sign of the energy gap enlargement due to the QC effects. The absorption spectra were used to estimate the energy gap of the CuO NPs. Figure 4.14 represents $(\alpha h\nu)^2$ versus $h\nu$ plots of absorption spectra for three different sizes of CuO NPs. The energy bandgap for the CuO NPs was estimated by fitting a straight line to the linear portion of the curve and E_g is the interception of the line with the $h\nu$- axis. The direct bandgap values are 3.35, 3.65 and 3.85 eV for NPs of sizes 10.1, 5.0 and 1.2 nm, respectively. Those values are larger than (3.25 ± 0.05 eV) for bulk CuO as reported by Koffyberg, et al. [373]. The increase in the direct E_g values (a blue shift) of CuO with the decrease in nanoparticle size is associated with the electron confinement effect.

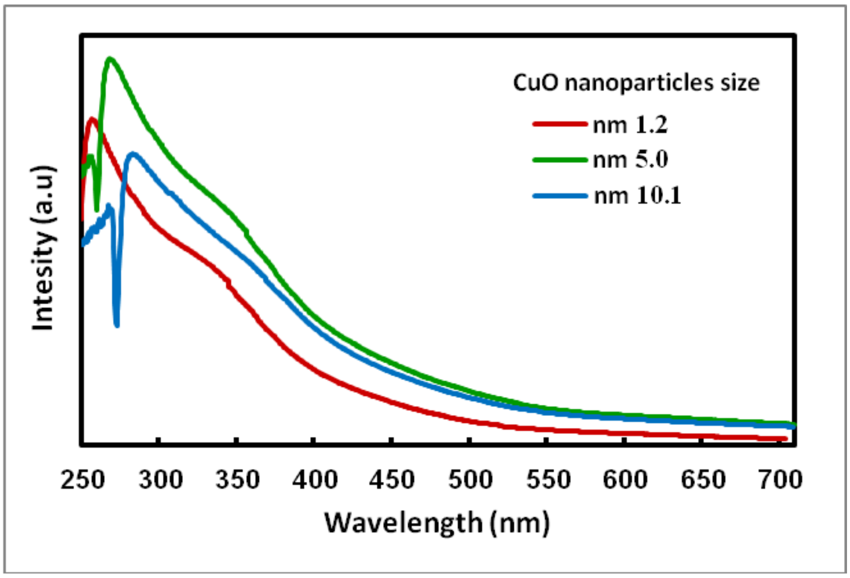

Figure 4.13 UV-Visible absorption spectra of colloidal CuO NPs, dispersed in DMF.

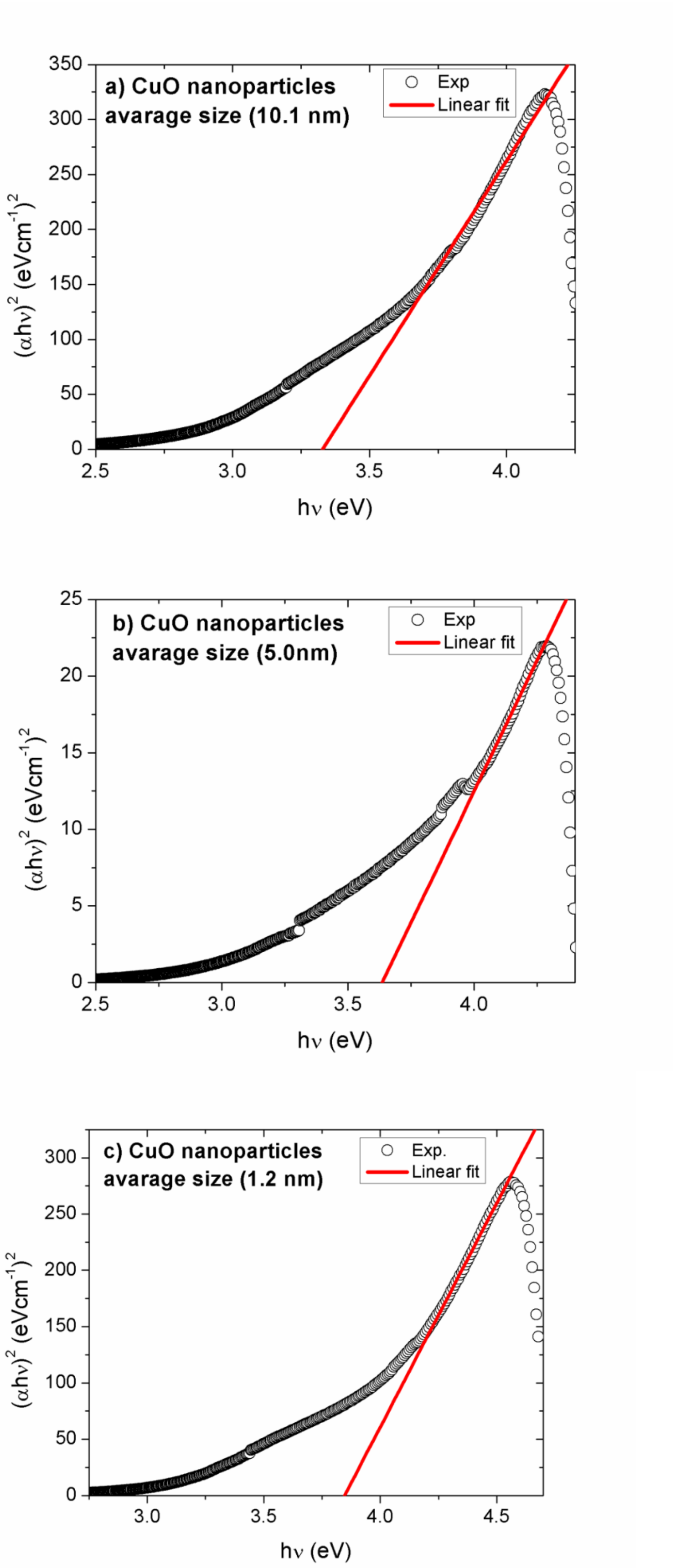

Figure 4.14 Direct band gap estimations for three different sizes of CuO NPs.

Photoluminescence spectra

The variation of the PL spectra for colloidal CuO NPs as a function of NP size and excitation wavelength is shown in Figure 4.15. Each spectrum exhibits a broad UV emission peak which is known as the near band-edge emission, and a sharp visible emission peak. The spectra in Figure 4.15 (a–c) represents CuO NPs of sizes 1.2, 5.0 and 10.1 nm and exhibits UV emission peaks, located around 350, 360 and 390nm, as well as orange emission peaks centered at about 600, 610 and 620 nm, respectively. The excitation wavelength used to produce the results in figure 3.15 (a–c) is 300 nm. The PL spectra in Figure 4.15 (d–f) represents CuO NPs of sizes 1.2, 5.0 and 10.1 nm, but excited by UV light of 320nm wavelength. As the 320 nm wavelength light has lower energy than that of 300 nm wavelength, the spectra in Figure 4.15 (d–f) exhibit an obvious red shift compared to those excited using a wavelength of 300 nm. The spectra exhibit UV emission peaks located around 380, 390 and 410 nm, and red emission peaks centered at about 635, 650 and 670 nm, respectively.

It is noticeable that all the PL spectra in Figure 4.15 exhibit an obvious blue shift with decreasing nanoparticle size because of the bandgap enlargement shown above and calculated E_g, due to the increase of QC effects. The near band-edge emission is attributed to emissions originating from the recombination of electrons and holes in the CuO free excitons which is very sensitive to particle size in the quantam-mechanical sense. The smaller the nanoparticle, the shorter the wavelength emission; for instance, the spectrum in Figure 4.15a is more blue shifted than the spectrum in Figure 4.15c. Similar phenomena can be observed when comparing Figure 4.15d with Figure 4.15f due to a reduction in nanoparticle size and increases in QC effects.

The photoluminescence spectra are useful for understanding electron transition energies within CuO NPs through determining the emission peaks and using them to estimate the corresponding electronic energy levels. Table 4.3 shows the emission peaks of different sizes of CuO NPs and their corresponding energy levels. The table demonstrates a strong blue shift of the photoluminescence peaks as the nanoparticle size decreases. The UV emission peaks correspond to the band edge emissions. The visible emission peaks (600–670 nm) are attributed to the presence of surface defects, which are expected to be of large density in NPs of small sizes. The orange emission peaks (600–620 nm) are attributed to the presence of oxygen vacancies, and the red emission peaks (635–670 nm) are due to the multiple oxidation states of copper [374].

The variation or specifically, the red-shifting of the peak with the increase of excitation wavelength from 300 nm to 320 nm does require further analysis. It is worth recalling that this observation violates Kasha's rule which states that the bandgap of any bulk material should be independent of the intrinsic defect states and excitation wavelength [375].

However, when the dimensions of a particle are reduced, to nanosize, several factors affect the electronic structure and consequently the fluorescence [376] such as: (i) The large surface-to-volume ratio induces a high-density of surface-defect states (such as vacancies and interstitials) which have their specific effects such as the creation of trap levels, which are responsible for visible emissions. To illustrate this, Figure 4.16 shows a schematic diagram of the electronic band structure showing the defect effects, where the arrows represent mechanisms of radiative and non-radiative electronic transitions that can occur under different wavelength excitations. For instance, as CuO NPs get excited at 300 nm (4.1 eV), the electrons are transferred up to a sub-band in the conduction band then either (a) relax to shallow donor levels via the non-radiative transition (thermalization), then make radiative transition to the valance band, or (b) make radiative transition to shallow acceptor states then relax to the valence band via thermalization. Thus, there are many possibilities, yielding a high probability of high-energy photon emissions. Whereas, for excitation at 320 nm (3.8 eV), matching the E_g of particle size 1.2 nm, the recombination process for excitons passes through possible combinations of thermalizations and radiative electronic transitions yielding emitted photons of lower energies. (ii) The energy interactions between the CuO NPs and the polar solvent lead to inhomogeneous broadening of the absorption spectrum. As the excitation wavelength is changed, slightly different associated nanoparticles are excited and the emission characteristic of these particles is observed. Nonetheless, the energy transfer between these energetically different particles remains inefficient due to the low concentration of these distinct particles [377], which dictates selective photo-excitation and selective recombination processes between their surface states. (iii) With the increase in excitation wavelength, the fluorescence life time (τf) decreases and transition rate increases [378, 379]. This condition reveals that it is possible to observe emissions from the unrelaxed photoexcited species more than from the lower-energy excited species. All the above factors might contribute in yielding the behavior of the excitation-wavelength dependent fluorescence in CuO NPs.

Similar cases of excitation-wavelength dependence of fluorescence in nanostructures were reported for Cu_2O nanowires [378], ZnO nanocolloids [380] and CdS NPs [381].

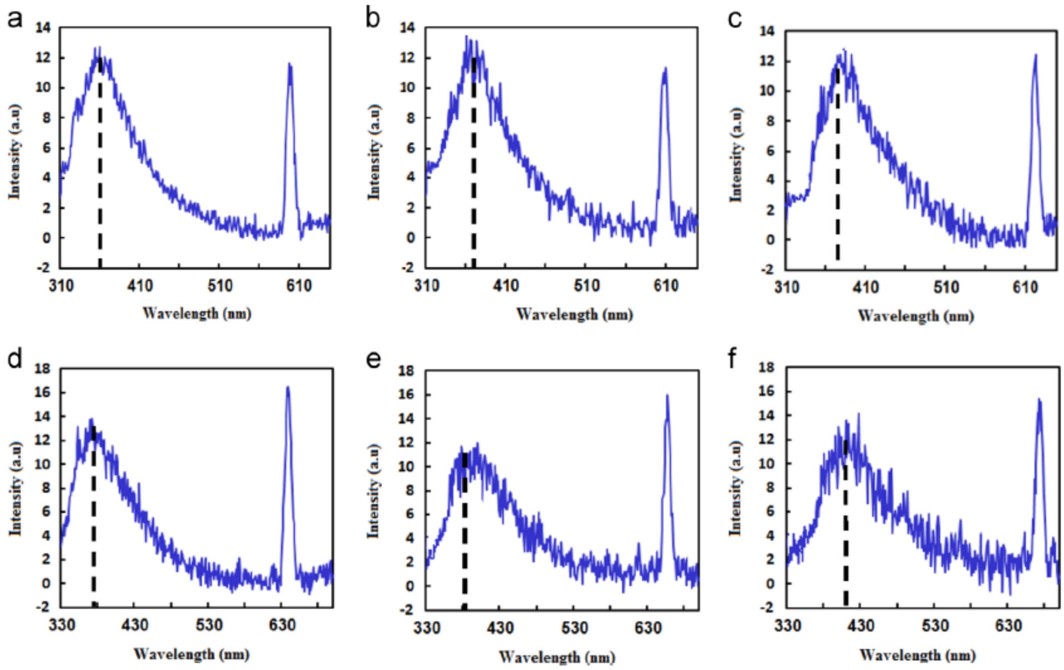

Figure 4.15 Photoluminescence spectra of colloidal CuO NPs, (a–c) excited at 300 nm for NPs of sizes 1.2, 5.0 and 10.1 nm, respectively. (d–f) Excited at 320 nm for NPs of sizes 1.2, 5.0 and 10.1 nm, respectively.

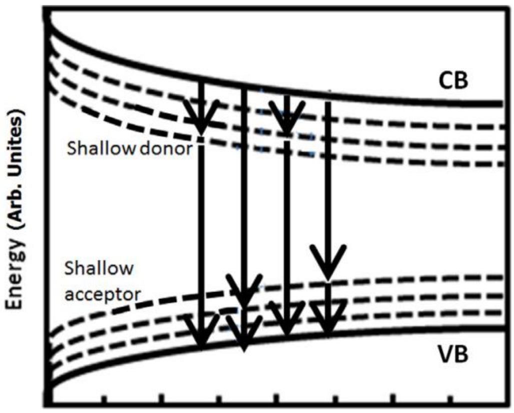

Figure 4.16 Schematic diagram of the band structure with the arrows representing mechanisms of radiative and non-radiative electronic transitions possibly to occur under different wavelength excitations.

Table 4.5 Emission peaks of different CuO nanoparticle sizes and their corresponding energy levels. Herein, λ is wavelength and E is the optical energy

	Excitation at 300 (nm)				Excitation at 320 (nm)			
	UV emission peak center		Visible emission peak center		UV emission peak center		Visible emission peak center	
Size (nm)	λ (nm)	E (eV)	λ (nm)	E (eV)	λ (nm)	E (eV)	λ (nm)	E (eV)
1.2	350	3.54	600	2.06	380	3.26	635	1.95
5.0	360	3.44	610	2.03	390	3.17	650	1.90
10.1	390	3.17	620	1.99	410	3.02	670	1.85

4.1.4 CdS Nanoparticles

Figure 4.17 shows SEM images of CdS NPs prepared on a copper grid. The figure confirms the formation of the NPs and most of the particles show an approximately cubic shape. The image reveals that CdS NPs are agglomerated.

Figure 4.18 shows the size distribution histogram of CdS NPs methanol dispersion. It is clear that it has narrow size distribution, with an average size of 20nm. That is supposed to show weak confinement effects because the NPs size is a little larger than the CdS Bohr radius (5.8nm) [382] below which is a fundamental shift in electronic and optical properties that can be observed as a function of nanoparticle size where strong QC effects are expected.

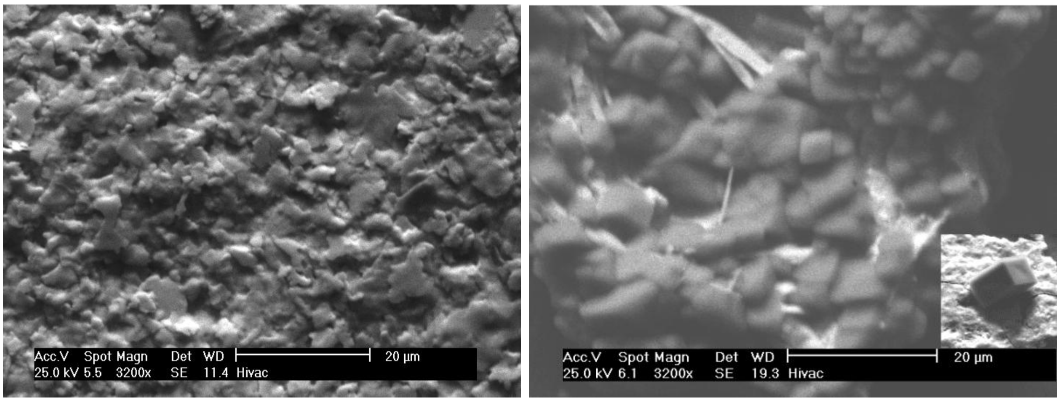

Figure 4. 17 SEM images of agglomerates of CdS NPs.

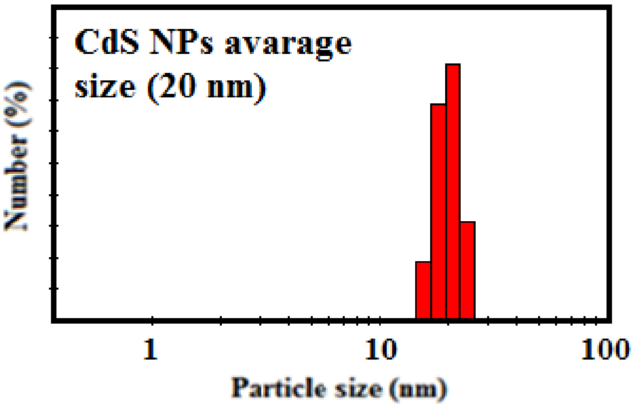

Figure 4.18 Size distribution histogram CdS (NPs), dispersed in methanol.

4.1.5 Bi_2S_3 Particles

Figure 4.19 shows SEM image of Bi_2S_3 particles prepared on a copper grid. The figure confirms the formation of the particles. The image reveals that Bi_2S_3 particles are somewhat agglomerated, thus the shape of the particles cannot be determined.

Figure 4.20 shows the size distribution histogram of Bi_2S_3 particles in water dispersion. It is clear that it has a narrow size distribution on a range of about 1 micrometer, with an average size of 1016 nm that is considered as bulk material.

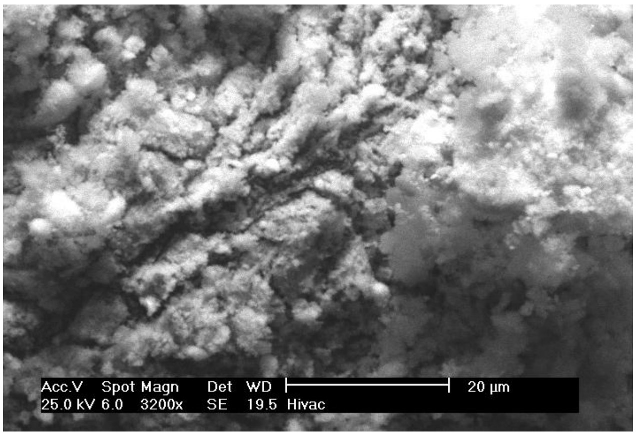

Figure 4.19 SEM image of Bi_2S_3 layer.

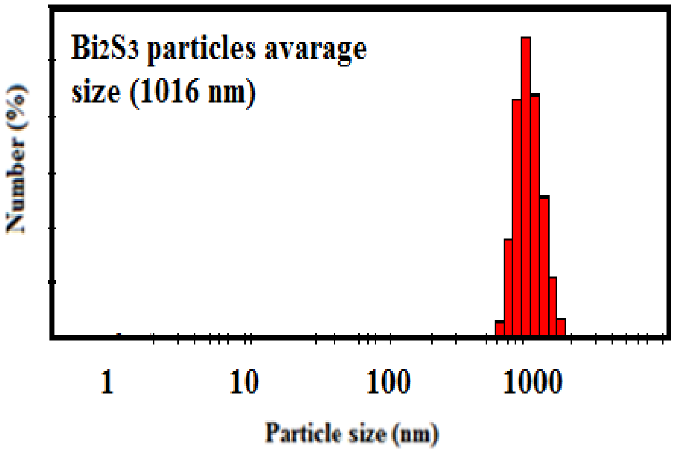

Figure 4.20 Size distribution histogram Bi_2S_3 particles, dispersed in water.

4.2 Solar Cells Characterization

4.2.1 Solar Cell of ($ZnO/TiO_2/CdS/PbS$/PEDOT: PSS)

(i) Architecture characterization

Figures 4.21 (a-d) show the FTO/ ZnO/ TiO_2/ CdS/ PbS/ PEDOT:PSS/Au solar cell structure, its equilibrium E_g diagram, the cross-sectional SEM view of the cell and a photograph of the same cell of $1cm^2$ area. The ZnO/ TiO_2 layer can effectively invert the polarity of the cell, since ZnO/ TiO_2 accept electrons from the active layer, transport them to the FTO electrode and block hole transfers. This is owing to its high electron affinity and mobility resulting from its low conduction band level. The CdS layer enhances the transfer of photgenerated electrons from PbS and CdS to the ZnO/TiO_2 layer through gradual energy alignment. On the other hand, PEDOT: PSS accepts holes from the active layer, transports them to the Au electrode and blocks electron transfer in this direction due to its high conduction and valance band levels (see Figure 4. 21b).

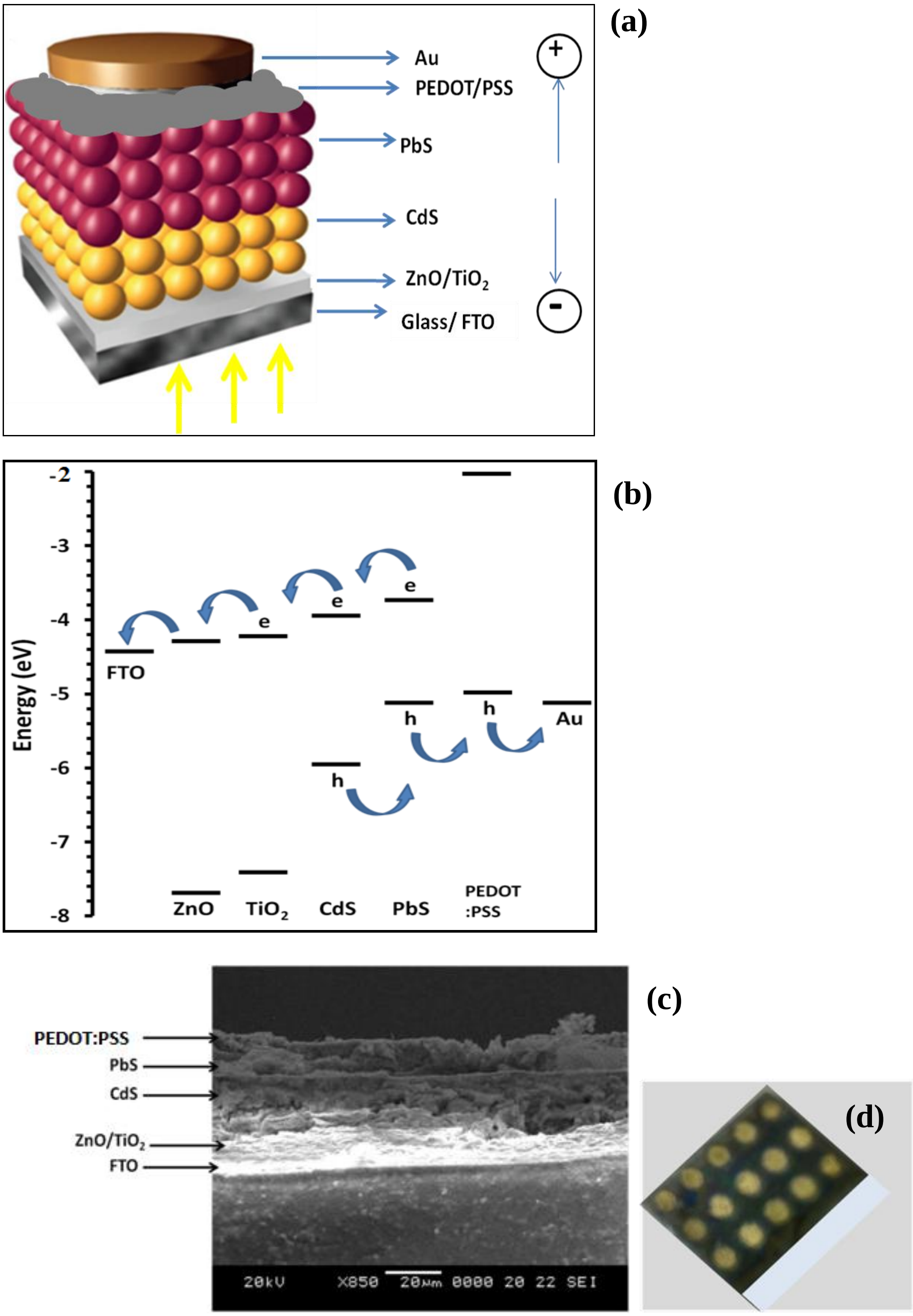

Figure 4.21 (a) Schematic structure of FTO/ ZnO/ TiO_2/ CdS/ PbS/ PEDOT:PSS/ Au solar cell. (b) Energy level diagram of the same device. (c) Cross-sectional SEM image of the same device. (d) Photograph of a typical device (substrate dimensions, 1cm× 1cm).

(ii) Performance characterization

Figure 4.22 reveals the semi-log current–voltage (I–V) characteristic graph of the cell with structure: FTO/ZnO/TiO_2/ CdS/PbS/PEDOT:PSS/ Au, and a circular cell active area of 0.785mm^2, under dark and 1 sun illumination with voltage varying from -1V to +1V. The graph shows a high slope which indicates high resistance.

Figure 4.23 shows the current density - voltage (J–V) characteristics for ZnO/TiO_2/CdS/PbS/PEDOT:PSS/Au solar cell structure under 1 sun illumination, at voltage intervals between 0V and 0.6V. The cell yielded a short-circuit current density (J_{SC}) of 24.2 mA/cm^2, an open circuit voltage (V_{OC}) of 544 mV, a fill factor (FF) of 38.2% and a power conversion efficiency (PCE) of 5.04%. The characteristic resistance of the solar cell can be indicated through the inverse of the slope of the graph which is estimated by dividing the V_{OC} by the short-circuit current (2860 Ω or 22.5 Ω cm^2).

Figure 4.24 shows the obtained PCE values of four cells, which have been synthesized with the same cell structure: FTO/ZnO/TiO_2/CdS/PbS/ PEDOT: PSS/Au. 10 readings of the PV parameters for each cell were recorded. The average PCEs for each one of the four cells were 5.02 ± 0.028, 4.95 ± 0.033, 4.92 ± 0.042 and 4.88 ± 0.033, with their total average as 4.94 ± 0.034. Each cell performance was tested in ambient air at room temperature and under 1sun illumination.

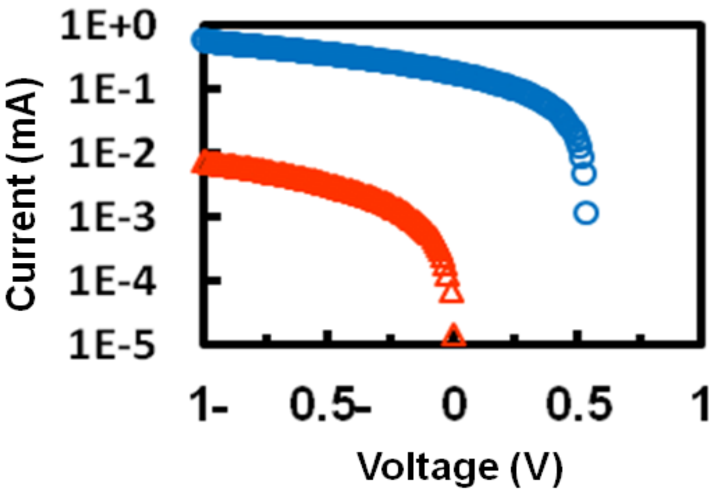

Figure 4.22 Semi-log scale to the base 10 of the I−V characteristic of the solar cell with structure: FTO/ZnO/TiO_2/CdS/PbS/PEDOT:PSS/Au, in dark (triangle symbols) and under 1 sun illumination (circle symbols).

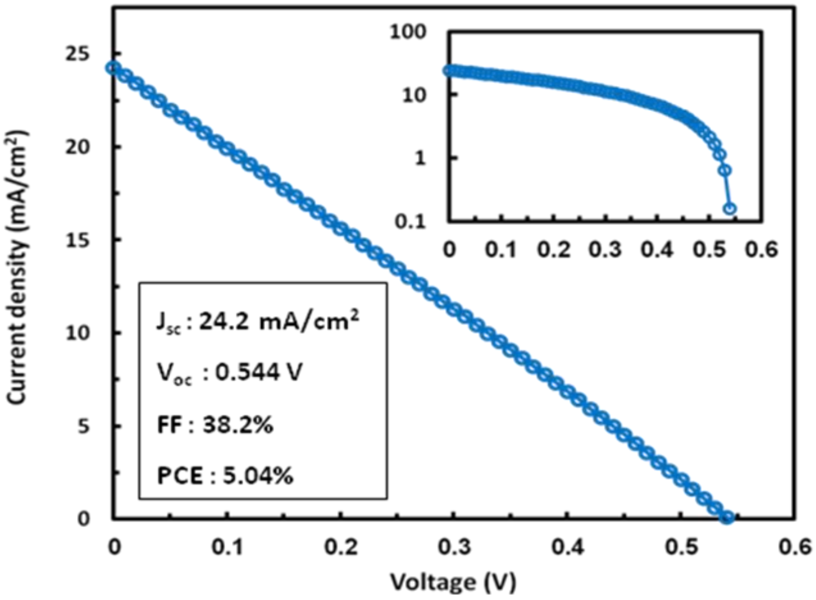

Figure 4.23 J−V characteristic of the solar cell with the structure: FTO/ZnO/TiO_2/CdS/PbS/PEDOT:PSS/Au, the inset on the top represents the semi-logarithmic scale to the base 10 of the characteristic graph, the inset on the bottom represents the PV performance of the cell. The cell performance is measured under AM1.5G simulated solar illumination.

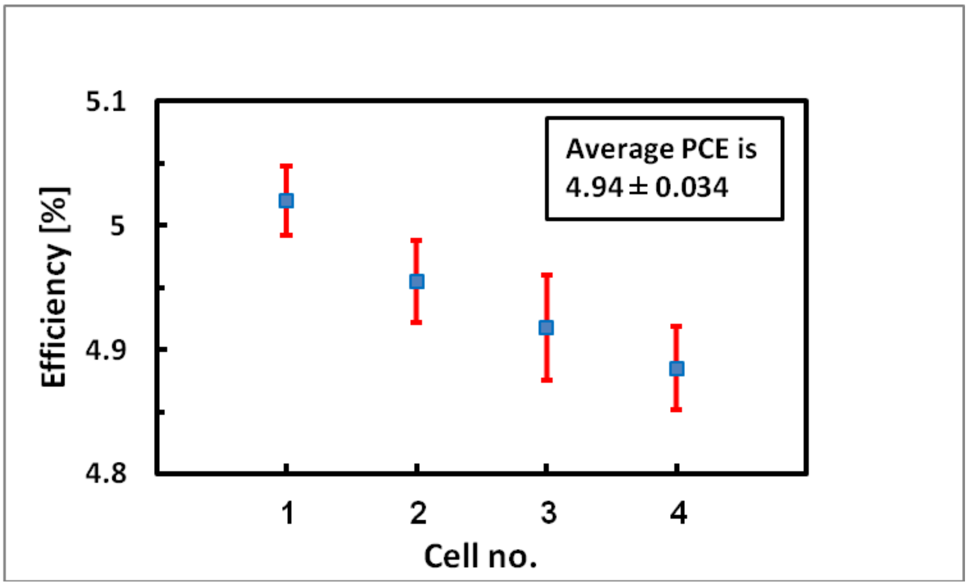

Figure 4.24 The average PCE values for 10 readings and their standard deviation for each one of the four cells with the structure: FTO/ZnO/TiO_2/CdS/PbS/ PEDOT:PSS/Au.

(iii) Stability characterization

The stability of the cells was tested over a period of approximately six weeks when the cells were stored in a dark box at room temperature without applying any inert gases and tested in air under 1sun illumination. Figures 4.25 (a – e) shows the results of this testing. Figure 4.25a represents every one of the cell parameters using arbitrary units for comparison. The graphs show good stability over six weeks with only minor changes over the whole testing period. The short circuit current exhibits a gradual initial decrease and then saturates after about sixteen days. The V_{OC} and FF exhibit an initial increase in the first 12 days then a gradual decline with a partial recovery after 16 days. The PCE was almost unaffected in the first 12 days and then started to decrease with partial recovery after 16 days, as indicated in Figures 4.25 (b–e).

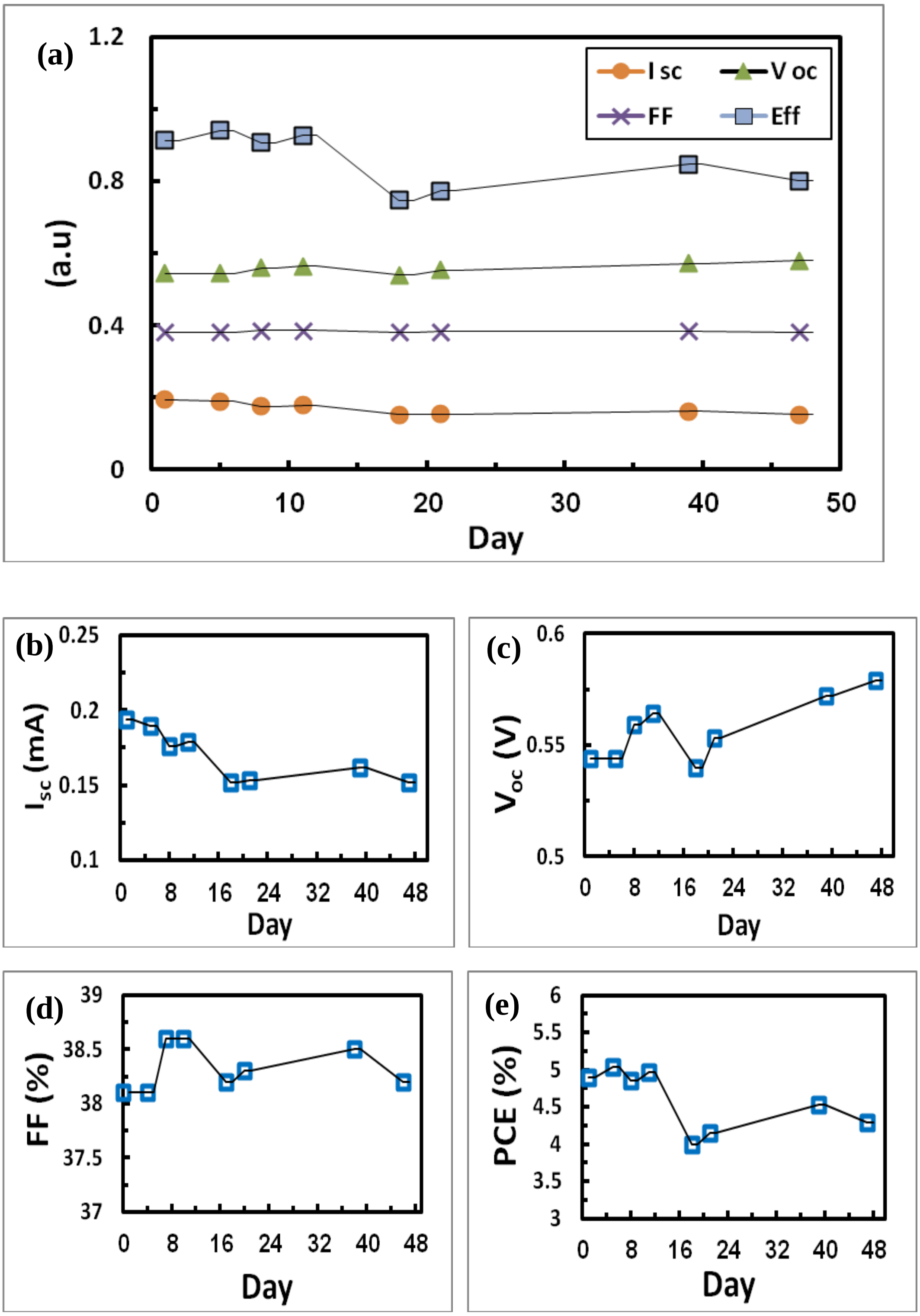

Figure 4.25 Stability testing of solar cell with the structure: FTO/ ZnO/ TiO_2/ CdS/ PbS/ PEDOT:PSS/ Au.

4.2.2 Effect of Employing Different Electron Transport Layers (ETL)

The architecture and PV performance of the synthesized heterojunction QDSCs with various ETLs was examined. The ETLs were: ZnO/TiO_2, TiO_2, and ZnO/TiO_2/GO.

(i) Architecture characterization

Figure 4.26 shows SEM images with different magnifying scales for the surface morphology of ZnO NP layers which are the first layers on top of the FTO glass coated substrate. It can be noticed that the ZnO NPs layer surface appeared to cover all the regions of the substrate very well without the presence of voids, pinholes or cracks. The roughness of the surface can be observed. Figure 4.27 shows the SEM images for the surface morphology of the TiO_2 NPs layer which was applied on top of the previous layer (ZnO). This revealed that the substrate surface was influenced by employing TiO_2 NPs since it has a uniform surface morphology over the entire substrate and a significant reduction in the roughness of the surface, with small particles and some gatherings. Thus Figure 4.27 represents the surface morphology of the ZnO/TiO_2 structure that is being employed as the ETL for most of the synthesized hetrojunction QDSCs in this study.

Figure 4.28 shows the SEM images for the surface morphology of the reduced GO layer which was applied on top of the previous layer (TiO_2). A significant increase in the roughness of the surface is noticed due to the addition of a reduced GO layer. It covers the entire substrate without the presence of voids, pinholes or cracks. Figure 4.28 (a, b) shows the GO layer after annealing at 200ºC for 1 hour and Figure 4.28 (c, d) shows another sample of a GO layer after annealing at 300ºC for 1 hour and reveals a decrease in the roughness of the surface as the annealing temperature increases. The GO is thermal treated in an N_2 environment to reduce GO by removing functional groups and extra oxygen in order to convert GO from an electrical insulator to a semiconductor.

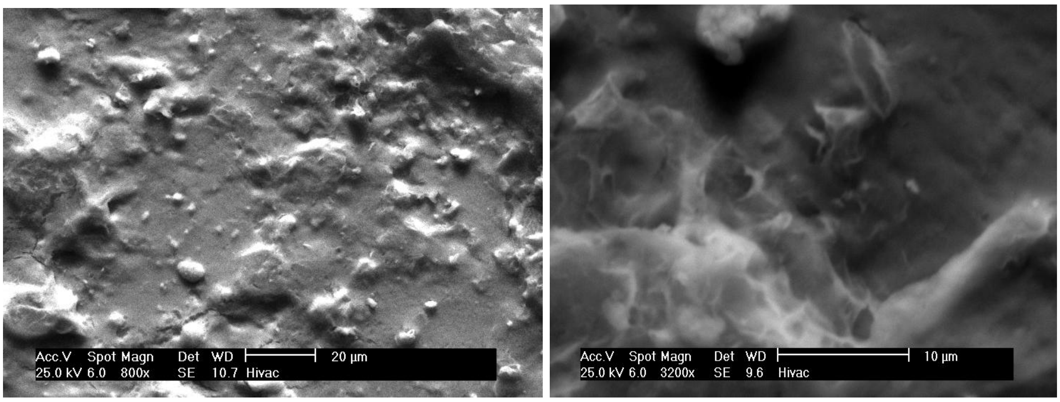

Figure 4.26 SEM image of ZnO (NPs) layer.

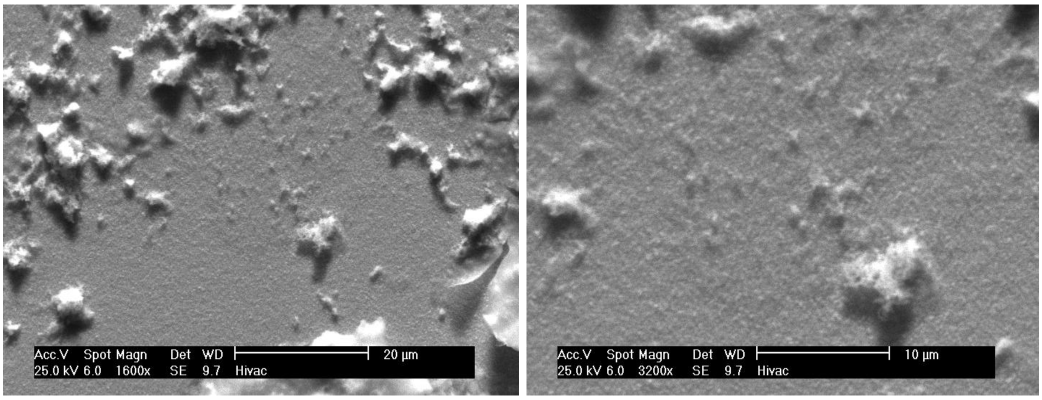

Figure 4.27 SEM image of TiO_2 (NPs) layer.

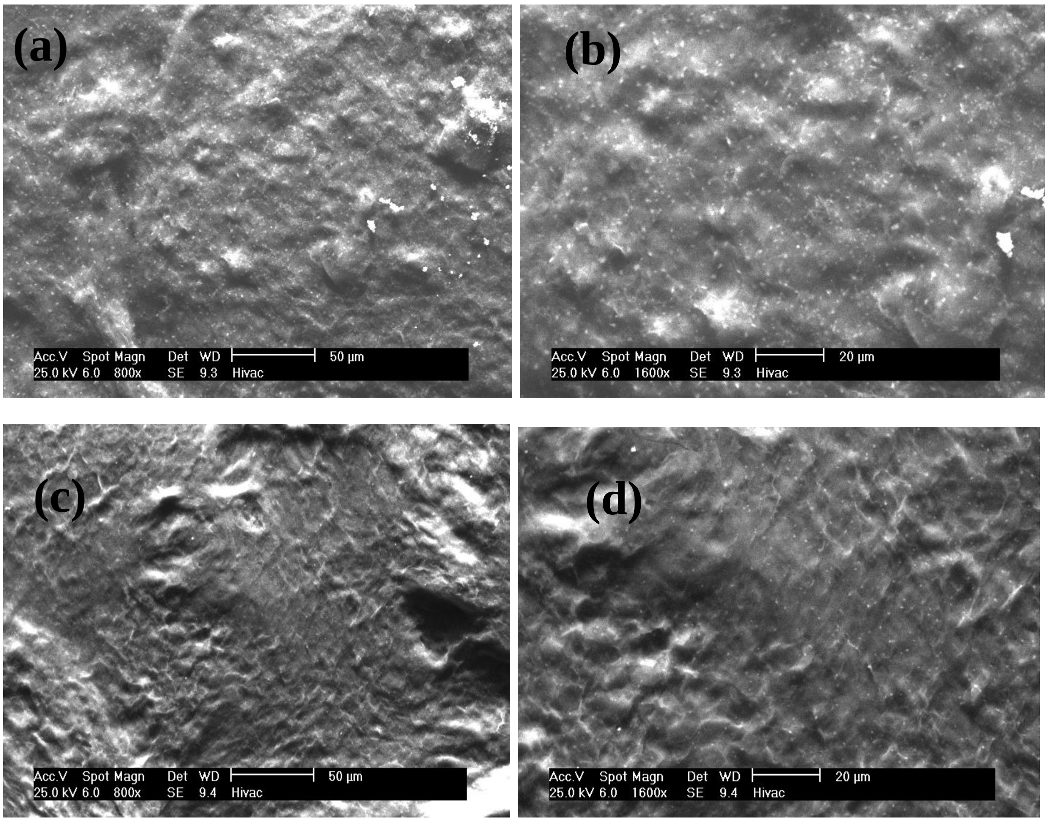

Figure 4.28 SEM image of GO; (a,b) annealed at 200ºC layer, (c,d) annealed at 300ºC layer.

(ii) Performance characterization

Figure 4.29 shows J−V characteristics for three SCs with various ETLs, under 1 sun illumination. The active area of the cells was about 0.785mm^2. As indicated by the graphs the performance has slightly decreased with the change of ETLs: ZnO/TiO$_2$, and TiO$_2$, respectively. While a major decline in PV parameters is evident. The semi-log graphs in Figure 4.29 indicate that cell ZnO/TiO$_2$/GO has the highest characteristic resistance (R$_{CH}$) as it gives the highest inverse slope and so the drop off in PCE is related to the high R$_{CH}$ of the cell.

Table 4.4 shows the PV parameters for each solar cell. ZnO/TiO$_2$ produced the highest PCE, FF, and J$_{SC}$. Very little decrease in PCE, FF, and J$_{SC}$

was observed in TiO_2 without ZnO, while a small increase in V_{OC} was obtained in TiO_2. This can be associated with the functional change in the ETL as shown in the equivalent energy level diagrams in Figure 4.30. A large reduction in PCE in the cell where a reduced GO layer was added is related to a J_{SC} reduction. The variation in PV parameters of the cells in Table 4.4 can be explained by their equivalent energy level diagrams in Figure 4.30 and the surface morphology of the layers in Figures 4.26 to 4.28**.** Since ZnO/TiO_2 has the best PCE due to its uniform surface with less roughness, thus enhancing electron transfer, and due to the presence of tiny pores in the TiO_2 layer, it improves the ability for CdS NP loading. From the equivalent energy level diagram, we can see that ZnO has more electron affinity than TiO_2, so employing ZnO/TiO_2 together utilizes a good CB and VB match between CdS NPs and the FTO layer. Whereas the use of GO increases the roughness and disturbs the energy level alignment thus hindering the charge transfer and separation.

Table 4.6 The photovoltaic parameters for PbS QDSC structures with different Electron Transport Layers (ETL).

Cell with ETL:	J_{SC} (mA/cm^2)	V_{OC} (mV)	P_{max}(mW)	FF (%)	PCE (%)
ZnO/TiO_2	24.2	544	0.0395	38.2	5.04
TiO_2	21.5	558	0.0358	38.0	4.57
ZnO/TiO_2/GO	9.89	528	0.0146	35.5	1.86

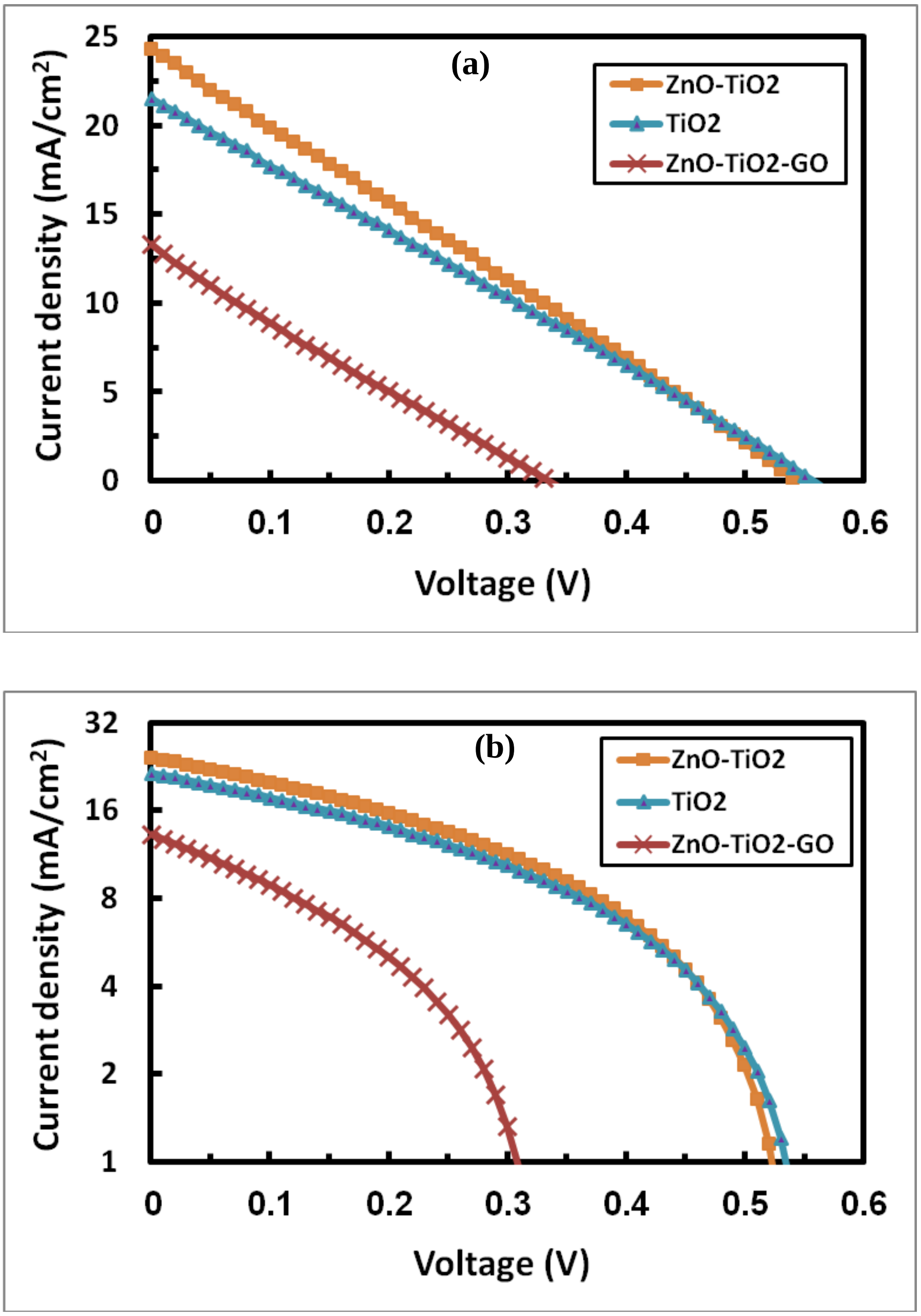

Figure 4.29 J–V characteristics for three different structures of PbS QDs based SCs with various electron transport layers (ETL), (a) linear scale (b) semi-logarithmic scale to the base 2. The cells were measured under AM1.5G simulated solar illumination.

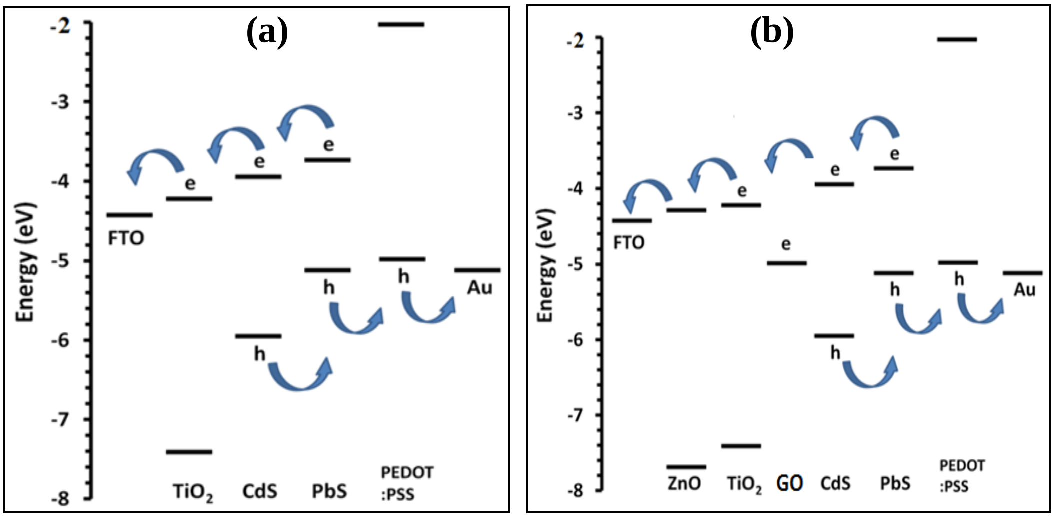

Figure 4.30 Energy level diagrams for cells with ETL as (a) TiO_2 and (b) $ZnO/TiO_2/GO$, respectively.

4.2.3 Effect of Employing Different Active Layers (AL)

The architecture and PV performance of synthesized heterojunction QDSCs with various ALs were examined. The AL was changed to CdS/PbS, Bi_2S_3/CdS/PbS and Bi_2S_3/PbS.

(i) Architecture characterization

Figure 4.31 shows SEM images with different magnifying scales for CdS NPs as deposited on top of a ZnO/ TiO_2 layer on an FTO-coated glass substrate. The sample was coated with 11 SILAR cycles of CdS NPs. The images confirm that the TiO_2 was uniformly coated with CdS NPs without cracks or pinholes and the CdS NPs film was homogenous and demonstrates a cellular network suitable for filling with with PbS QDs to form the AL of CdS/PbS. Figure 4.32 shows SEM image of a Bi_2S_3 layer as deposited on top of the ZnO/ TiO_2 layer on an FTO-coated glass substrate, the sample was coated with 7 SILAR cycles of Bi_2S_3

particles. The SEM results indicate that Bi_2S_3 is unequally covered on the substrate with small particles and some gatherings, a lot of space between Bi_2S_3 particles is available for filling with PbS QDs or CdS NPs to form the AL in cell Bi_2S_3/CdS/PbS or Bi_2S_3/PbS, respectively. Figure 4.33 shows SEM images with different magnifying scales for the surface morphology of a PbS QDs layer coated on top of CdS. It can be noticed that PbS QDs penetrates within the CdS NPs layer and covers the entire surface with roughness.

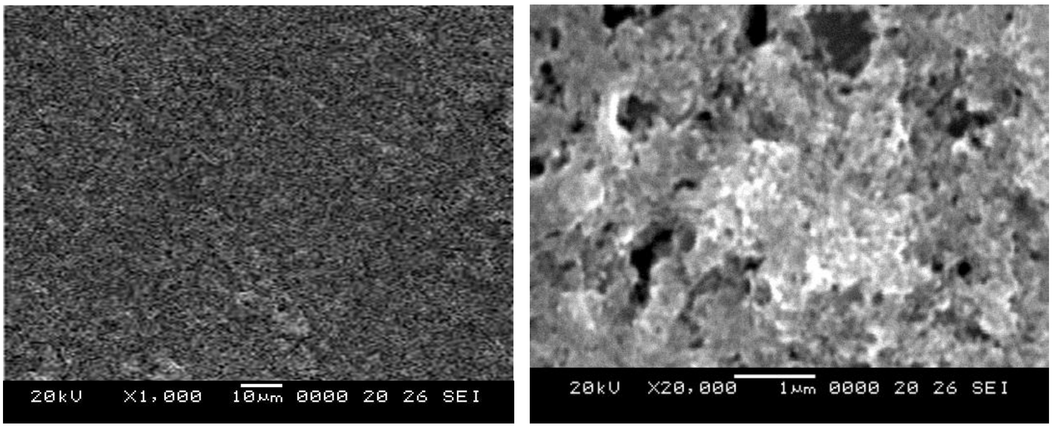

Figure 4. 31 SEM image of CdS NPs layer.

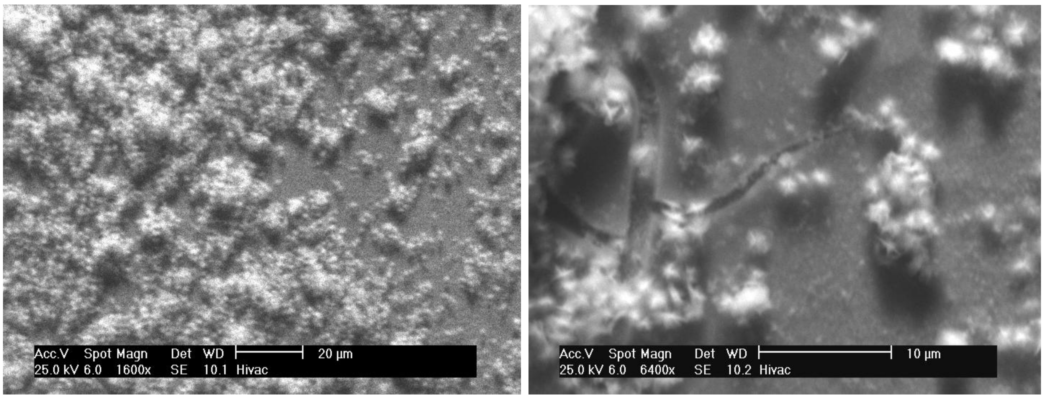

Figure 4.32 SEM image of Bi_2S_3 NPs layer on TiO_2.

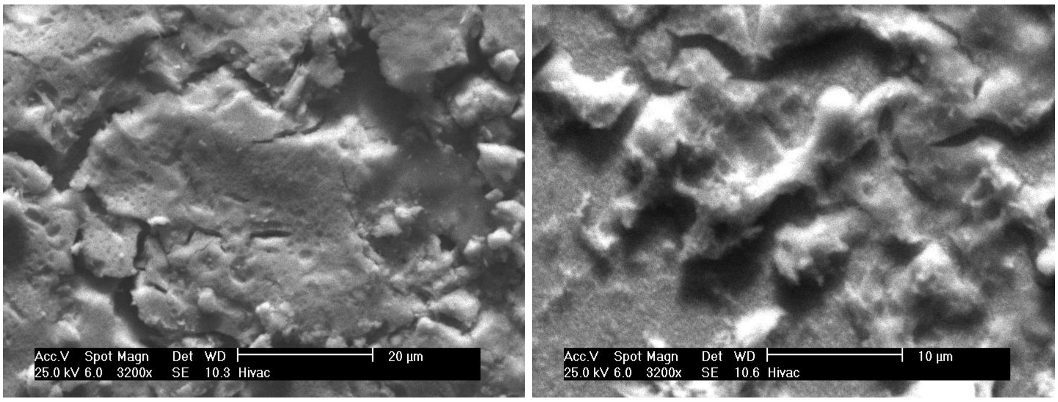

Figure 4.33 SEM image of PbS QDs layer.

(ii) Performance characterization

Figure 4.34 shows J−V characteristics for three SCs with various ALs, under 1 sun illumination: the active area of the cells was about 0.785mm^2. As indicated in the graphs the performance decreased with the change in the AL: CdS/PbS, Bi_2S_3/CdS/PbS, and Bi_2S_3/PbS, respectively. The semi-log graphs in Figure 4.34 indicate that the Bi_2S_3/PbS AL has the highest R_{CH} as it gives the highest inverse slope, so the drop off in PCE can be related to the high R_{CH} of the cell.

Table 4.5 shows the PV parameters for each solar cell: CdS/PbS yielded higher PV parameters than the other cells with a J_{SC} of 24.2mA/cm^2, a V_{OC} of 544mV, an FF of 38.2 % and a PCE of 5.04%, respectively. The PCE decreased to 2.42% by using Bi_2S_3/CdS/PbS as the AL, and a further decrease in PCE (1.27 %) was obtained by Bi_2S_3/PbS due to V_{OC} reduction (334 mV). This can be associated with the functional change in the AL as shown from the equivalent energy level diagrams in Figure 4.35 as the CB of Bi_2S_3 is lower than that of CdS.

Figure 4.35a shows the equivalent energy level diagrams of Bi_2S_3/CdS/PbS where the Bi_2S_3 layer is applied between the TiO_2 and CdS layers and the CB is well matched between them. Figure 4.35b shows the equivalent energy level diagrams for Bi_2S_3/PbS, where Bi_2S_3 is applied instead of a CdS NPs layer that is well matched with the PbS QDs energy levels. The variation in PV parameters of the cells in Table 4.5 can be explained by their equivalent energy level diagrams in Figure 4.35 and the surface morphology of the layers as shown in Figures 4.31 to 4.33**.** CdS/PbS has better PCE than those of Bi_2S_3/CdS/PbS and Bi_2S_3/PbS, which is related to lack of uniform coating of the Bi_2S_3 layer with voids that hinder the charge transfer.

Table 4.7 The PV parameters for PbS QDSCs structures with different active layers (AL).

Cell with AL:	J_{SC} (mA/cm^2)	V_{OC} (mV)	P_{max}(mW)	FF (%)	PCE (%)
CdS/PbS	24.2	544	0.0395	38.2	5.04
Bi_2S_3/CdS/PbS	13.6	527	.0703	33.7	2.42
Bi_2S_3/ PbS	13.3	334	0.0115	33.1	1.47

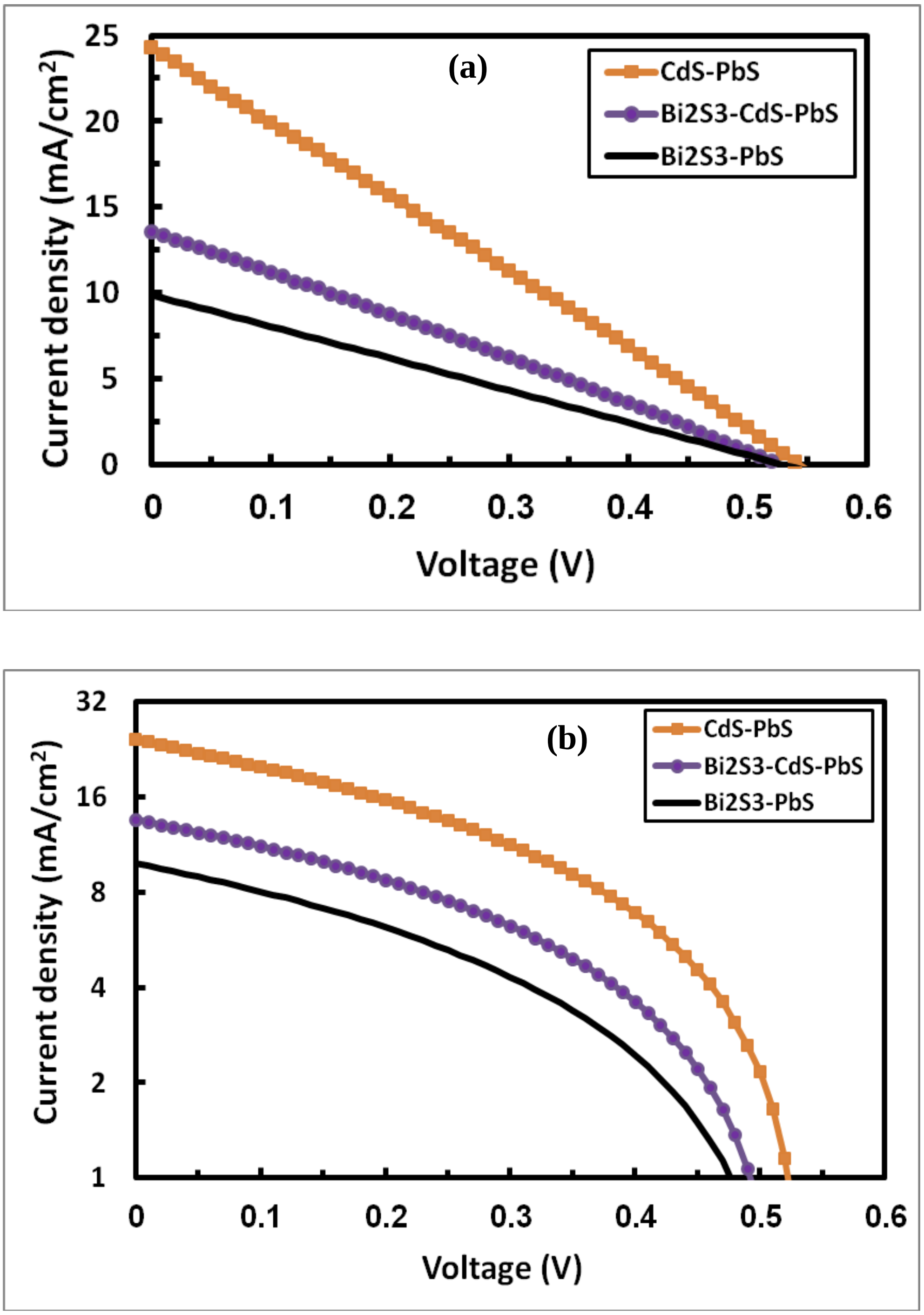

Figure 4.34 J–V characteristics for three different structures of PbS QDs based SCs with various active layers (AL), (a) linear scale (b) semi-logarithmic scale to the base 2. The cells were measured under AM1.5G simulated solar illumination.

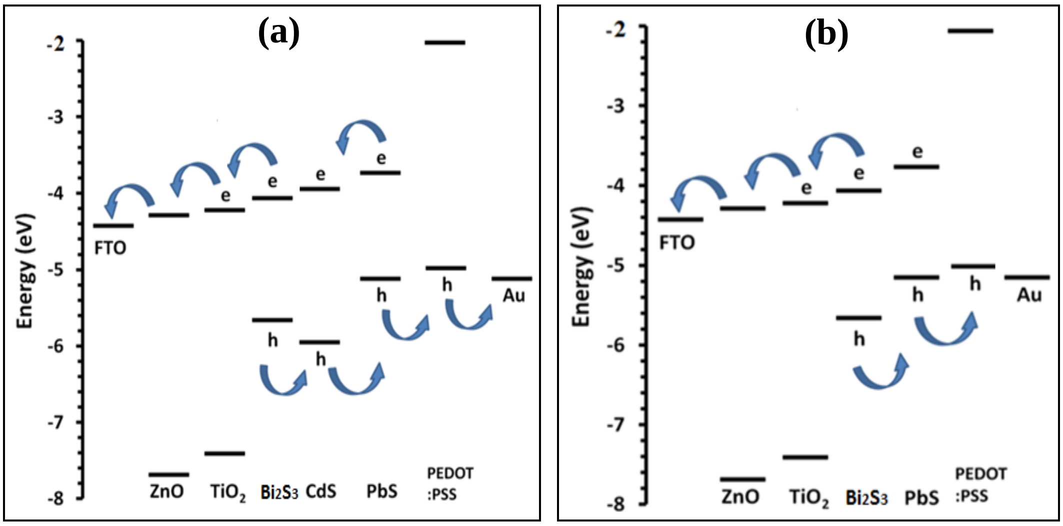

Figure 4.35 Energy level diagrams for cells with AL as (a) Bi_2S_3/ CdS/ PbS and (b) Bi_2S_3/PbS, respectively.

4.2.4 Effect of Employing Different Hole Transport Layers (HTL)

The architecture and PV performance of the synthesized heterojunction QDSCs with various HTL were examined. The HTL was changed to PEDOT:PSS, GO/PEDOT:PSS, GO, CuO, without HTL.

(i) Architecture characterization

Figure 4.36 shows SEM images of PEDOT: PSS layers as deposited on top of a PbS QDs layer. The SEM results indicate the smoothness of the surface which is homogenous and without any cracks which is extremely important for efficient charge transfer (holes to Au electrode). Figure 4.37 shows SEM images with different magnifying scales for the surface morphology of CuO NPs as deposited on top of a PbS QDs layer. Some spherical shape grains and gatherings were noticed on top of the PbS layer indicating that the CuO NPs were spread over the entire surface with large spaces between the CuO NPs spherical shape agglomerates. The presence of voids or pinholes hinders the efficient charge transfer to the Au electrode.

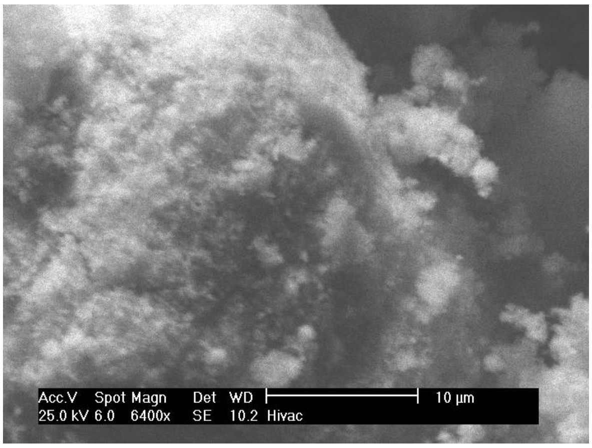

Figure 4.36 SEM image of PEDOT:PSS NPs layer.

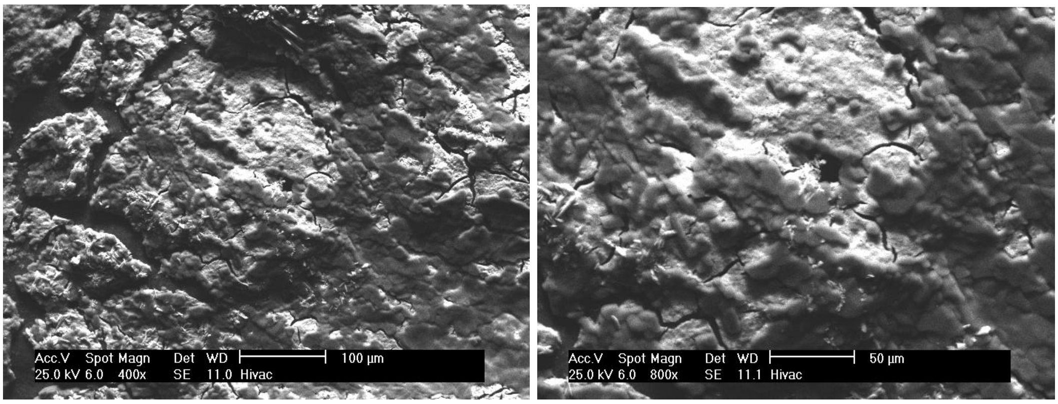

Figure 4.37 SEM image of CuO NPs layer on PbS QDs.

(ii) Performance characterization

Figure 4.38 shows J–V characteristics for three SCs with various HTLs, under 1 sun illumination: the active area of the cells was about 0.785mm^2. As indicated from the graphs the performance decreased with the change in HTL to PEDOT:PSS, GO/PEDOT:PSS, GO, CuO, without HTL. The semi-log graphs in Figure 4.38 give an indication of the cells resistance from the slopes of the graphs.

Table 4.6 shows the PV parameters for each solar cell. PEDOT:PSS yielded the highest J_{SC}, V_{OC}, FF and PCE. The PCE decreased to 3.95% when using GO/PEDOT: PSS as the HTL, while using a GO layer alone as the HTL yielded a PCE of 1.22% and the lowest FF (33%). A drop of PCE (0.85%) was obtained by applying a CuO NPs layer. The lowest J_{SC} (2.2mA/cm^2), V_{OC} (412mV) and PCE (0.38 %) were obtained by the cell where no transport layer was applied.

Figure 4.39a shows the equivalent energy level diagrams for GO/PEDOT: PSS where a reduced GO layer was used beneath a PEDOT: PSS layer, which has a work function of about 5eV: close to the work function of gold (~5.2 eV) and matching the VB of PEDOT: PSS (~5.1 eV). Therefore, holes can be injected from the VB of PEDOT: PSS to GO. Figure 4.39b shows the equivalent energy level diagrams of the cells where GO is the only HTL. Figure 4.39c shows the equivalent energy level diagrams of the cell where the CuO NPs layer was applied as HTL, with E_g ~3.6 eV and a very high CB that blocks the electron transfer to the Au electrode. Figure 4.39d shows the equivalent energy level diagrams of the cell where no HTL was applied. The variation in PV parameters of the cells in Table 4.6 can be explained by their equivalent energy level diagrams in Figure 4.39 and the surface morphology of the layers in Figures 4.28, 4.36 and 4.37**.** PEDOT: PSS has a better PCE than the other cells because the addition of PEDOT: PSS on top of PbS smoothes the surface which facilitates the hole transfer to the Au electrode. Additionally, a high CB for PEDOT: PSS makes it hole attractive and provides an electron blocking layer. The PEDOT: PSS layer stops any migration of Au atoms to PbS or any oxidation of the PbS layer. So in the case where no HTL is applied a large drop in the PV performance is noticed. The decrease in the PCE in the case of employing GO can be attributed to an incomplete reduction process. GO was also annealed at 200 ºC where higher temperetures were required, but high temperatures affect the NPs crystalinity and consequently, their PV performance. The decrease in PCE in cases employing CuO can be related to the lack of a uniform coating of the CuO NPs layer leaving voids that hinder the charge transfer.

Table 4.8 The PV parameters for PbS QDSCs structures with different hole transport layers (HTL).

Cell no.	J_{SC} (mA/cm^2)	V_{OC} (mV)	P_{max}(mW)	FF (%)	PCE (%)
PEDOT:PSS	24.2	544	0.0395	38.2	5.04
GO/PEDOT:PSS	19. 2	540	0.0310	38.1	3.95
GO	7.25	509	0.00955	33.0	1.22
CuO	5.68	426	0.0067	35.3	0.854
None	2.2	412	0.00305	37.8	0.388

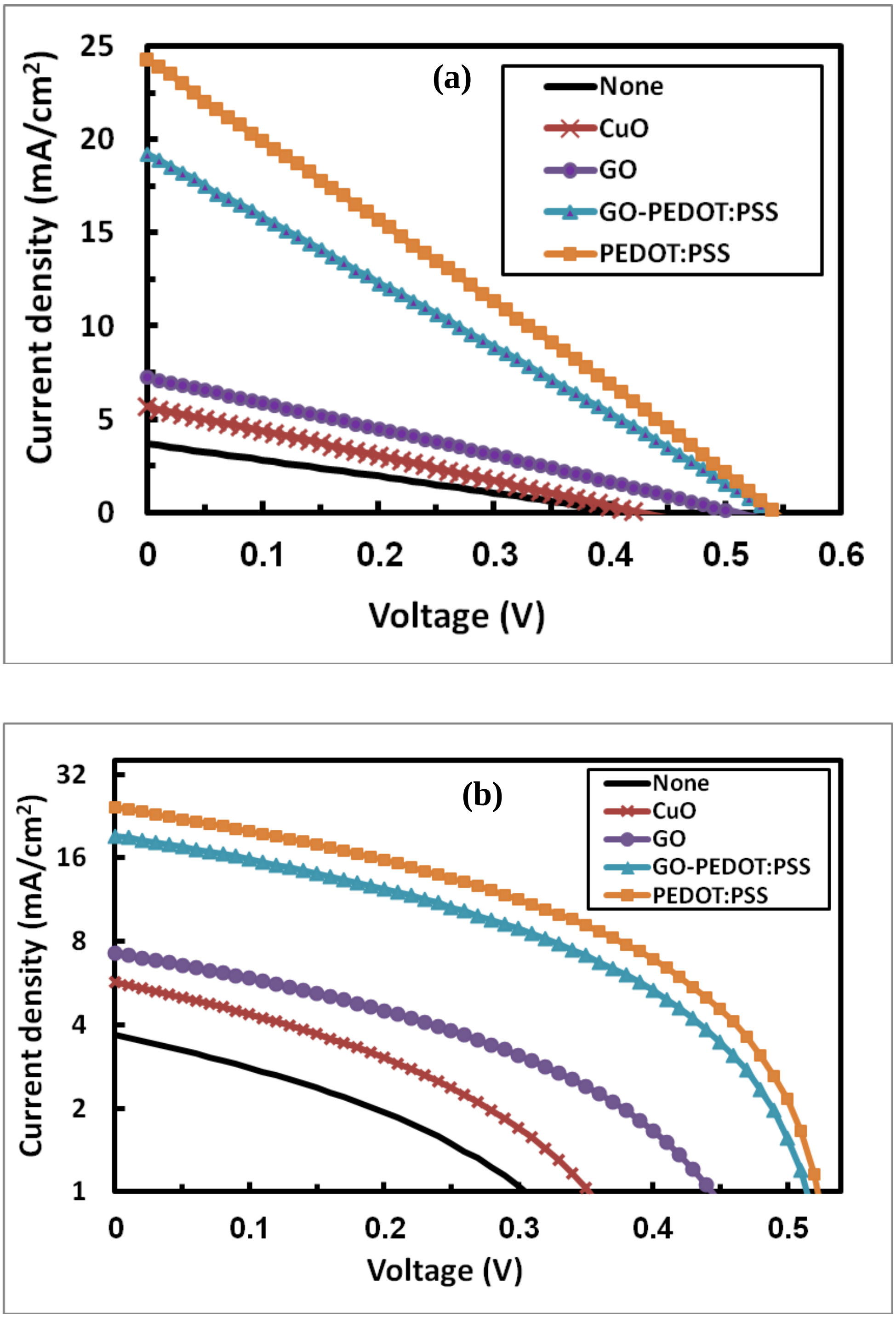

Figure 4.38 J−V characteristics for five different structures of PbS QDs based SCs with various hole transport layers (HTL), (a) linear scale, (b) semi-logarithmic scale to the base 2. The cells were measured under AM1.5G simulated solar illumination.

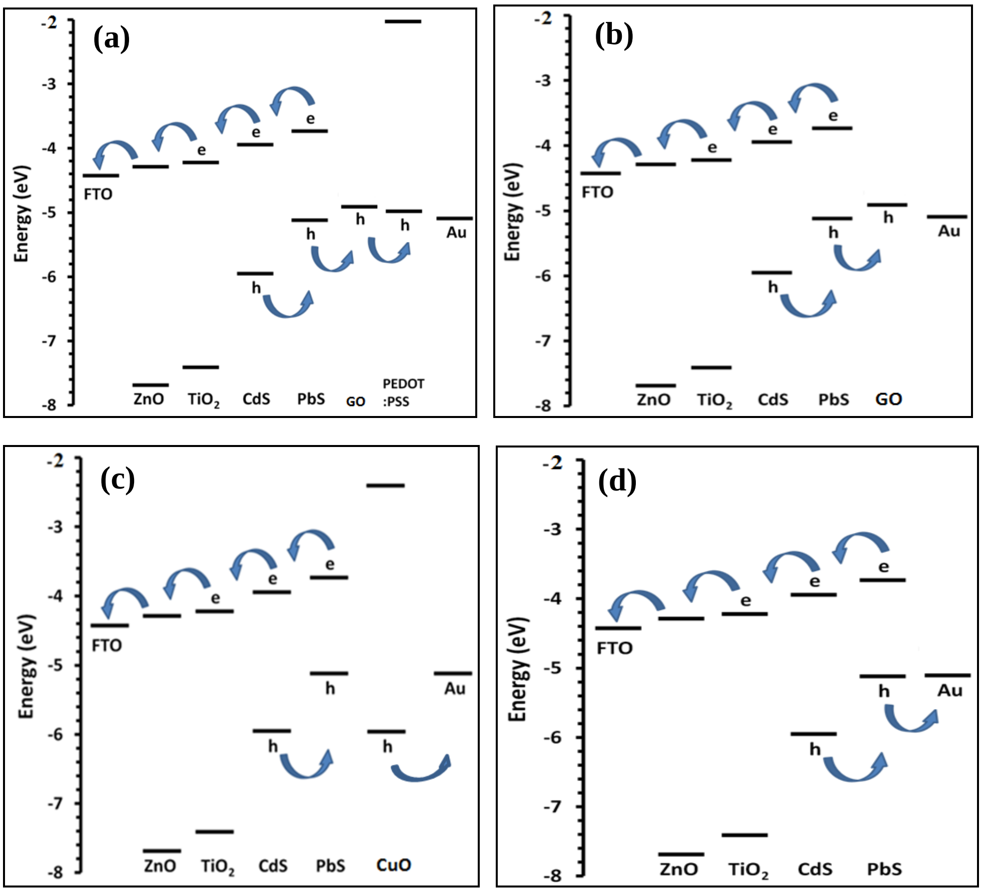

Figure 4.39 (a-d) Energy level diagrams for cells as (a) GO/ PEDOT:PSS, (b) GO, (c) CuO, (d) Non, respectively.

4.2.5 Effect of Active Layer Thickness

The archeticture and PV performance of synthesized heterojunction QDSCs with various AL thicknesses have been examined. The AL thickness was changed to CdS(11)/PbS(6), CdS(6)/PbS(6), CdS(11)/Blend(2)/PbS(4), CuO and CdS(11)/Blend(4)/PbS(4). Here the numbers next to the NPs denote the number of SILAR cycles or spin-coated repetitions.

(i) Architecture characterization

Figure 4.40 shows SEM images of the surface morphology of PbS and CdS blended on top of a PbS QDs layer. Since CdS NPs have a bigger size than

PbS QDs, CdS cubic shape crystals are distinguished within the PbS QDs layer. It can be noticed that the surface of CdS and PbS when blended do not appear to be uniform and the CdS NPs are distributed unequally within the PbS QDs layer.

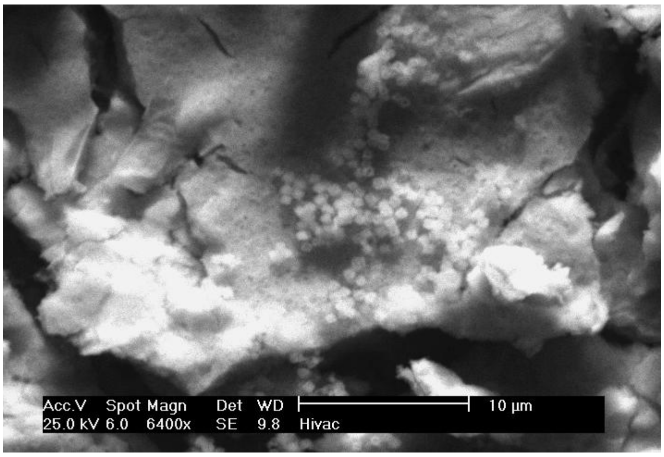

Figure 4.40 SEM image of blend of CdS and PbS NPs layer.

(ii) Performance characterization

Figure 4.41 shows J−V characteristics for five SCs with different active layer thicknesses under 1 sun illumination: the active area of the cells was about 0.785mm^2. The graphs show the thickness of CdS NPs reduced by decreasing the number of CdS NPs SILAR cycles from 11 to 0 SILAR cycles. The performance decreased noticeably. Also applying a blend layer of CdS and PbS reduced the performance and a further reduction was noticed when increasing the thickness of the blended layer. The semi-log graphs in Figure 4.41 indicate that the cell where a thick blended layer of CdS and PbS was applied between the CdS NPs layer and the PbS QDs layer had the highest resistance as it gives the highest inverse slope. The cell where the thickness of CdS was reduced from 11SILAR cycles to 6 SILAR cycles, gives the lowest resistance as it gives the lowest inverse slope and the decrease in PCE is due to a V_{OC} reduction. Also more than 11SILAR cycles of CdS NPs were examined and resulted in a decrease in PCE. Thus 11SILAR cycles produce a suitable layer thickness for charge transfer and reach the heterojunction interface without recombination.

Table 4.7 shows the PV parameters for each solar cell. The first cell yielded the highest PV parameters J_{SC} (24.2 mA/cm^2), V_{OC} (544 mV), FF (38.2%) and PCE (5.04%), where 11 SILAR cycles were applied. The cell with 6 SILAR cycles yielded a J_{SC} of 18.8mA/cm^2, a V_{OC} of 310mV, an FF of 34.3% and a PCE of 2.01%. The cell without a CdS NPs layer yielded a lower J_{SC} (15.2 mA/cm^2) and PCE (1.69%). In the case of applying the blended layer twice the cell yielded a J_{SC} of 17.7 mA/cm^2, a V_{OC} of 555 mV, an FF of 37.8% and a PCE of 3.71%. In the case of the cell where the thickness of the blended layer was 2 times that of the previous cell the resulting PCE (0.937%) was reduced to about 1/4. The drop off in the PCE is attributed to the fall in the J_{SC} (6.6 mA/cm^2). The decrease in PCE for the cells with blended layers can be attributed to the unequal distribution of PbS and CdS NPs within the layers in the solar cell structure, and as the thickness of the blended layer increases the charge separation and transfer is hindered.

Table 4.9 The PV parameters for PbS QDSCs structures with different AL thickness.

Cell with AL:	J_{SC} (mA/cm^2)	V_{OC} (mV)	P_{max}(mW)	FF (%)	PCE (%)
CdS(11)/PbS(6)	24.2	544	0.0395	38.2	5.04
CdS(6)/PbS(6)	18.8	310	0.0157	34.3	2.01
CdS(0)/PbS(6)	15.2	315	0.0133	35.4	1.69
CdS(11)/Blend(2) /PbS(4)	17.7	555	0.0291	37.8	3.71
CdS(11)/Blend(4) /PbS(4)	6.61	398	0.00735	35.6	0.937

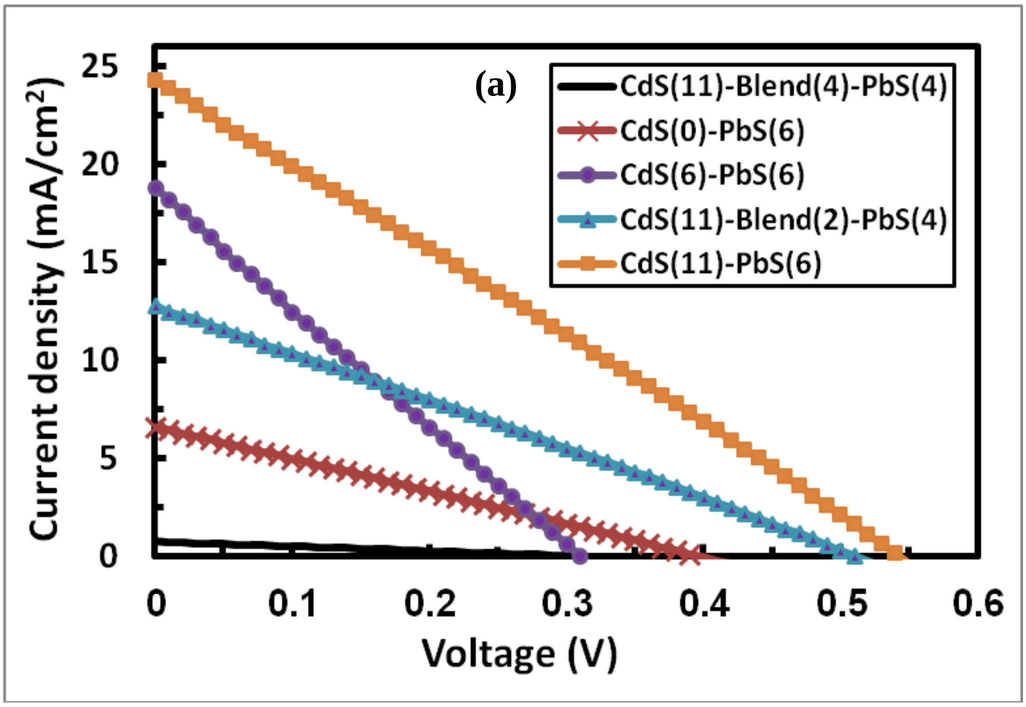

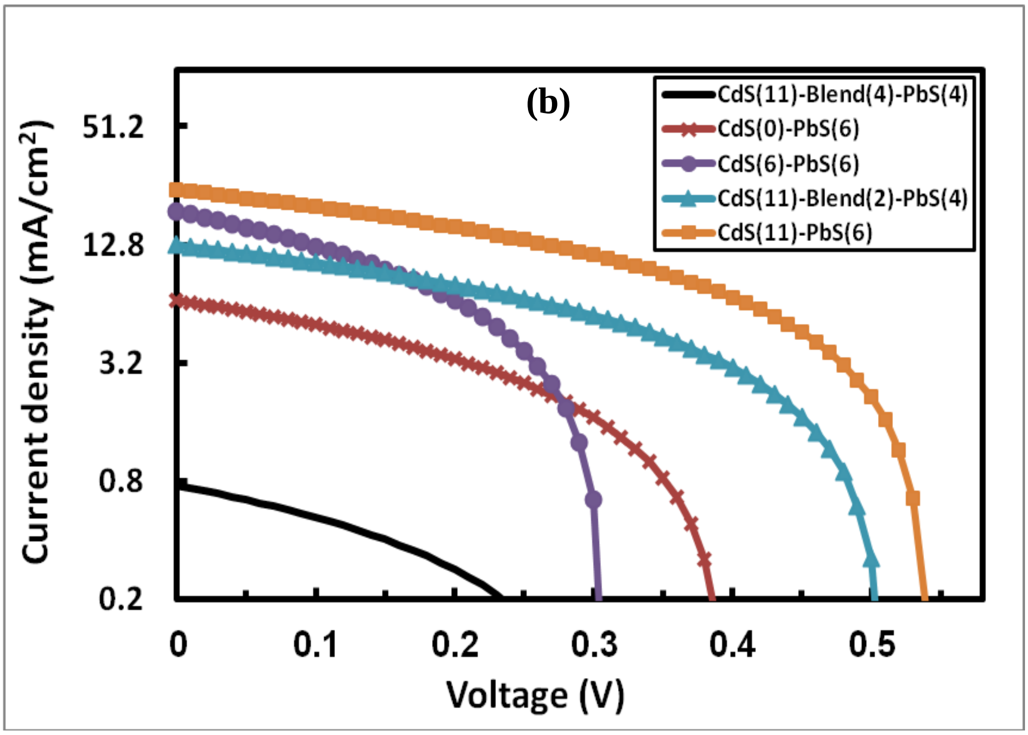

Figure 4.41 J–V characteristics for 5 different structures of PbS QDs based SCs with different active layer thickness, (a) linear scale, (b) semi-logarithmic scale to the base 2. The cells were measured under AM1.5G simulated solar illumination.

Summary of Results:

Table 4.10 shows some characteristic parameters for the synthesized NPs in this study, which were utilized in QDSCs structures. The synthesis method, size, wavelength at maximum absorption (λ_{max}), and the estimated E_g value of the NPs are displayed in the table below. Table 4.11 shows the structures of the synthesized QDSCs with the PCE for each cell. That makes the performance comparison of the QDSCs much easier.

Table 4.12 Characteristics of the synthesized nanoparticles.

NPs	Synthesis method	Size (nm)	λ_{max} (nm)	E_g (eV)
ZnO	Thermal chemical process	5.3	318	3.81
TiO_2	Decomposition of $TiCl_4$, and calcination		UV	> 3.2
PbS	Thermal chemical process	6.6	912	1.32
CuO	Colloid microwave- thermal process	1.2	255	3.85
CdS	SILAR	20	visible	> 2.42

Table 4.13 Heterojunction QDSCs based on PbS QDs with their efficiencies.

Solar cell structure	PCE (%)
FTO/ZnO/TiO_2/CdS/PbS/PEDOT:PSS/Au	5.04
FTO/TiO_2/CdS/PbS/PEDOT:PSS/Au	4.57
FTO/ZnO/TiO_2/GO/CdS(11)/PbS(6)/PEDOT:PSS/Au	1.86
FTO/TiO_2/ Bi_2S_3/CdS/PbS/PEDOT:PSS/Au	2.24
FTO/ZnO/TiO_2/Bi_2S_3/PbS/PEDOT:PSS/Au	1.47
FTO/TiO_2/CdS/PbS/ GO/PEDOT:PSS/Au	3.95
FTO/ZnO/TiO_2/ /CdS/PbS/ GO/Au	1.22
FTO/ZnO/TiO_2/CdS/PbS/CuO/Au	0.854
FTO/ZnO/TiO_2/CdS/PbS/Au	0.388
FTO/ZnO/TiO_2/CdS(6)/PbS(6)/PEDOT:PSS/Au	2.01
FTO/ZnO/TiO_2/ PbS/ PEDOT:PSS /Au	1.69
FTO/ZnO/TiO_2/CdS(11)/Blend(2)/PbS(4)/PEDOT:PSS/Au	3.71
FTO/ZnO/TiO_2/CdS(11)/Blend(4)/PbS(4)/PEDOT:PSS/Au	0.937

CHAPTER FIVE

CONCLUSIONS

5.1 Quantum Dots

The synthesized PbS QDs have a narrow size distribution: their average size is 6.6nm. The UV-visible absorption spectra of the PbS QDs showed absorption in the IR region with a maximum peak of 912nm that corresponds to an E_g of 1.36eV, that is much larger than the bulk.

The size of ZnO NPs is controlled by changing the NaOH concentration in the main solution of zinc acetate in ethanol. The smallest average NP size obtained was 5.3nm at 3.18mmol of NaOH concentration. By increasing or reducing this concentration the size of the particles increased: the other parameters remained fixed. Size distribution results confirm that a narrow size distribution can be obtained for ZnO NPs prepared via the wet chemical method. Absorption spectra show peaks in UV region and shifts towards shorter wavelengths by decreasing the particle size which indicates increases in both structural quality and QC effects. The PL spectra show highly intense visible emission peaks for every sample related to different ZnO defects. Low intensity UV emission peaks appeared for two samples related to excitonic emissions. These peaks were blue shifted as the particle size was reduced. The yellow emission for each sample can be hindered by introducing an N_2 environment instead of ambient air or the already prepared ZnO NPs in ethanol. The yellow emissions are attributed to electronic from deep-donor states, caused by intrinsic defects such as oxygen vacancies, to shallow acceptor states. The role of nitrogen gas is to passivate the dangling bonds of the defects and to introduce more shallow acceptor states. Consequently, N_2 bubbling yields emissions with shorter wavelengths (blue to violet) due to electronic transitions taking place between shallow donor and shallow acceptor states. After stopping N_2 bubbling, oxygen dominated all bonding to zinc defect states and yellow emissions returned from deep donor states (such as oxygen vacancies) to valence bands or to shallow acceptor states. Furthermore, the quick return of the yellow colour after stopping N_2 bubbling may reveal that the defects concerned are mostly located in the surface layer of the ZnO NPs.

CuO NPs were successfully prepared using the colloid thermal method involving microwave radiation. Using this technique, the NPs produced possessed narrow size distributions. The particle size was found to decrease as the microwave processing cycles increased. The preparation was efficient and economic while yielding high controls on the desired particle size, ranging in size from microns to 1nm with well-tailored bandgaps and specific optical properties. In UV–visible absorption, a blue shift in E_g was observed with decreasing nanoparticle size due to the QC effect. This is also in agreement with the direct E_g calculation based on the absorption spectra which showed higher values for smaller nanoparticle size. The PL spectra as a function of CuO NPs size are blue shifted with decreasing nanoparticle size due to the QC effect. This corroborates the results of the UV–visible spectra. Furthermore, the analysis of PL spectra as a function of the excitation wavelength showed that the peak emission wavelength can be red-shifted by increasing the excitation wavelength from 300nm to 320nm. This phenomenon was attributed to the selective recombination processes of excitons in the CuO NPs resulting from several factors such as the existence of a distribution of energetically different molecules having different defect densities and levels, the interactions between NPs and the polar solvent, and the decrease of the life time of the fluorescence associated with the increase of the transition rate. The CuO NPs in this study have a diversity of potential applications in the fields of photovoltaic, energy-selective luminescent devices, spintronics, catalysis and biomedicine.

5.2 Quantum Dot Solar Cells

The surface morphology of the solar cell has a major effect on charge transfer and separation. The surface has to be uniform over all regions thereby covering the substrate, without the presence of voids, pinholes or cracks. A good contact between the cell layers: the particles of each layer matching the particles of other layers is required to ensure the charge transfer at the interface between the n-type and p-type layers. By providing a path for the charge to reach the opposite electrodes, recombination of the charge is hindered and series resistance reduced.

Determining the right energy band alignment of the semiconductors is extremely important in order to arrange and synthesize the layers of the solar cell structure. The synthesized heterojunction QDSC structure benefits from gradual energy level alignment. The n-type and p-type QDs (CdS/PbS) as ALs, and the high hole mobility of organic semiconductors can be used as hole transport layers

(PEDOT: PSS). Also the high electron affinity of TiO_2 can be used as an electron transport layer.

In QDSSCs (where a liquid electrolyte is used) CdS NPs are loaded on the $TiO_{2.}$ We extended this idea to our solid (p-n) heterojunction QDSC, since ZnO/TiO_2/CdS is a promising structure for use in a heterojunction QDSC. (ZnO/TiO_2/CdS/PbS QDs /PEDOT: PSS/Au) achieved a PCE of 5% since ZnO/TiO_2 accepted electrons from the AL, transported them to the FTO electrode, and blocked hole transferd, owing to its high electron affinity and mobility and due to its low CB level. A CdS layer enhanced the transfer of photgenerated electrons from the PbS and CdS to the ZnO/TiO_2 layer through gradual energy alignment. On the other hand PEDOT: PSS accepted holes from the AL, transported them to the Au electrode and blocked electron transfer in this direction, owing to its high CB and VB.

Recommendations for future work:

- Optimize the surface morphology of the NP layers, by trying other deposition methods such as sputtering.

- Use other organic and inorganic short ligands for PbS QDs passivation and study their effects on PV performance.

- Use other efficient hole extraction layers such as molybdenum oxide (MoO_x) and vanadium oxide (V_2O_x) to be applied beneath the metal electrode instead of PEDOT:PSS, and study their effects on PV performance.

REFERENCES

1. T. Markvat, *Solar electricity*. 2nd edition, J. W. Sons. 2000, UK.

2. T. Oku, K. Kumada, A. Suzuki, K. Kikuchi, *Effects of germanium addition to copper phthalocyanine/fullerene-based solar cells.* Central European Journal of Engineering, 2012. **2**(2): p. 248-252.

3. A. Luque, S. Hegedus, *Handbook of photovoltaic science and engineering*. 1st edition, J. W. Sons. 2003, Ltd, Chichester.

4. A.D. Upadhyaya, V. Yelundur, A. Rohatgi, *High efficiency mono-crystalline solar cells with simple manufacturable technology,* Smartech, Georgia Institute of Technology. 2006, USA.

5. B. Westenhaus, *Thin film solar cell efficiency continues to improve,* New Energy & Fuel, 2013. **22**(35).

6. *First solar sets thin-film module efficiency world record of 17.0 percent,* I.N. FSLR, First solar business wire. 2014, New York

7. L. Han, A. Islam, H. Chen, C. Malapaka, B. Chiranjeevi, S. Zhang, X. Yang, M. Yanagida, *High efficiency dye-sensitized solar cell with a novel co-adsorbent.* Energy & Environmental Science, 2012. **5**(3): p. 6057-6060.

8. A. Yella, H.W. Lee, H.N. Tsao, C. Yi, A.K. Chandiran, M.K. Nazeeruddin, E. Diau, C.Y. Yeh, M.G. Zakeeruddin, *Porphyrin-sensitized solar cells with cobalt (II/III)–based redox electrolyte exceed 12 percent efficiency*. Science, 2011. **334**(6056): p. 629-634.

9. Z. He, C. Zhong, S. Su, M. Xu, H. Wu, Y. Cao, *Enhanced power-conversion efficiency in polymer solar cells using an inverted device structure.* Nature Photonics, 2012. **6**(7): p. 591.

10. L. Dou, J. You, J. Yang, C. Chen, H. He, S. Murase, T. Moriarty, K. Keith Emery, G. Li, Y. Yang, *Tandem polymer solar cells featuring aspectrally matched low-bandgap polymer.* Nature Photonics, 2012. **6**(180): p. 5.

11. X. Guo, N. Zhou, S. Lou, J. Smith, J. Hennek, J. López Navarret, S. Li, j. Strzalka, L. Chen, R. Chang, A. Facchetti, T. Marks, *Polymer solar cells with enhanced fill factors*. Nat Photonics, 2013. **7**(10): p. 825–833.

12. W. Li, K. Hendriks, C. Roelofs, K. Kim, M. Wienk, R. Janssen, *Efficient small bandgap polymer solar cells with high fill factors for 300 nm thick films.* Advanced Materials, 2013. **25**(6): p. 182.

13. S.R. Heliatekcon, *solidates its technology leadership by establishing a new world record for organic solar technology with a cell efficiency of 12%,* 2013.

14. *Konarka Power Plastic reaches 8.3% efficiency,* National Energy Renewable Laboratory. 2011, UK.

15. A. Facchetti, *π-Conjugated polymers for organic electronics and photovoltaic cell applications.* Chemistry of Materials, 2010. **23**(58): p. 733.

16. U. Zhokhavets, T. Erb, G. Gobsch, M. Al-Ibrahim, O. Ambacher, *Relation between absorption and crystallinity of poly(3-hexylthiophene)/fullerene films for plastic solar cells.* Chemcal Physics Letters, 2006. **50**(418): p. 347.

17. T. Ameri, N. Li, C. Brabec, *Highly efficient organic tandem solar cells: A follow up review.* Energy & Environmental Science, 2013. **413**(6): p. 2390.

18. P.R. Brown, R.R. Lun, N. Zhao, T.P. Osedach, D.D. Wanger, L.Y. Chang, M.G. Bawendi, V. Bulović, *Improved current extraction from ZnO/PbS quantum dot heterojunction photovoltaics using a* MoO_3 *interfacial layer.* Nano Letters, 2011. **11**(7): p. 2955-2961.

19. B.R. Hyun, J.J. Choi, K.L. Seyler, T. Hanrath, F.W. Wise, *Heterojunction PbS nanocrystal solar cells with oxide charge-transport layers.* ACS Nano, 2013. **7**(12): p. 10938-10947.

20. H. Park, P. Sehoon, J. Jean, J. Cheng, P. Araujo, M.S. Wang, M. Bawendi, M. Dresselhaus, V. Bulovic, K. Kong, S. Gradecak, *Graphene cathode-based ZnO nanowire hybrid solar cells.* Nano Letters, 2012. **13**(1): p. 233-239.

21. A.H. Ip, S.M. Thon, S. Hoogland, O. Voznyy, D. Zhitomirsky, L. Levina, L.R. Rollny, G.H.A. Fischer, K.W. Kemp, I.J. Kramer, Z. Ning, A.J. Labelle, K.W. Chou, A. Amassian, E.H. Sargent, Carey *Hybrid passivated colloidal quantum dot solids.* Nature Nanotechnology Letter, 2012. **7**(9): p. 577-582.

22. J. Tang, X. Wang, L. Brzozowski, D.A. Barkhouse, R. Debnath, L. Levina, E.H. Sargent, *Schottky quantum dot solar cells stable in air under solar illumination.* Advanced Materials, 2010. **22**(12): p. 1398-1402.

23. M. Ulfa, *Performance optimization of solar cells based on colloidal lead sulfide nanocrystals.* AIP Conference Proceedings, 2014. **1586**(1): p. 191-197.

24. N. Zhao, T.P. Osedach, L.Y. Chang, S.M. Geyer, D. Wanger, M.T. Binda, A.C. Arango, M.G. Bawendi, V. Bulovic. *Colloidal PbS quantum dot solar cells with high fill factor.* ACS Nano, 2010. **4**(7): p. 3743-3752.

25. H. Fu, S.W. Tsang, Y. Zhang, J. Ouyang, J. Lu, K. Yu, Y. Tao, *Impact of the growth conditions of colloidal PbS nanocrystals on photovoltaic device performance.* Chemistry of Materials, 2011. **23**(7): p. 1805-1810.

26. K.W. Johnston, A.G. Pattantyus-Abraham, J.P. Clifford, S.H. Myrskog, S. Hoogland, H. Shukla, E.J. Klem, L. Levina, E.H. Sargent, *Efficient schottky-quantum-dot photovoltaics: The roles of depletion, drift, and diffusion.* Applied Physics Letters, 2008. **92**(12): p. 278-282.

27. W. Yoon, J.E. Boercker, M.P. Lumb, D. Placencia, E. Foos, J.G. Tischler, *Enhanced Open-circuit voltage of PbS nanocrystal quantum dot solar cells.* Scientific Reports, 2013. **3**(2225): p. 1-7.

28. J. Tang, L. Brzozowski, D.A. Barkhouse, X. Wang, R. Debnath, R. Wolowiec, E. Levina, A.G. Pattantyus-Abraham, D. Jamakosmanovic, E.H. Sargent, *Quantum dot photovoltaics in the extreme quantum confinement regime: The surface-chemical origins of exceptional air-and light-stablity.* ACS Nano, 2010. **4**(2): p. 869-878.

29. G. Kim, B. Walker, H.B. Kim, J.Y. Kim, E.H. Sargent, J. Park, *Inverted colloidal quantum dot solar cells.* Advanced Materials, 2014. **26**(20) : p. 3321–3327.

30. A.G. Pattantyus-Abraham, I.J. Kramer, A.R. Barkhouse, X. Wang, G. Konstantatos, R. Debnath, L. Levina, I. Raabe, M.K. Nazeeruddin, M. Grätzel, E.H. Sargent, *Depleted-heterojunction colloidal quantum dot solar cells.* ACS Nano, 2010. **4**(6): p. 3374-3380.

31. W.K. Kemp, A.J. Labelle, S.M. Thon, A.H. IP, I.J. Kramer, S. Hoogland, E.H. Sargent, *Interface recombination in depleted heterojunction photovoltaics based on colloidal quantum dots.* Advanced Energy Materials, 2013. **3**(7): p. 917–922.

32. H. Wang, T. Kubo, J. Nakazaki, T. Kinoshita, H. Segawa, *PbS quantum dot-based heterojunction solar cells utilizing ZnO nanowires for high external quantum efficiency in the near-infrared region.* The Journal of Physical Chemistry Letters, 2013. **4**(15): p. 2455-2460.

33. T. Ju, R.L. Graham, G. Zhai, Y.W. Rodriguez, A.J. Breeze, L. Yang, G.B. Alers, S.A. Carter, *High efficiency mesoporous titanium oxide PbS quantum dot solar cells at low temperature.* Applied Physics Letters, 2010. **97**(4): p. 43106.

34. J.M. Luther, J. Gao, M. T. Lloyd, O.E. Semonin, M.C. Beard, A.J. Nozik, *Stability assessment on a 3% bilayer PbS/ZnO quantum dot heterojunction solar cell.* Advanced Materials, 2010. **22**(33): p. 3704–3707.

35. D.A.R. Barkhouse, R. Debnath, I.J. Kramer D. Zhitomirsky, A.G.Pattantyus-Abraham, L. Levina, L. Etgar, M. Grätzel, E.H. Sargent, *Depleted bulk heterojunction colloidal quantum dot photovoltaics.* Advanced Materials, 2011. **23**(28): p. 3134-3138.

36. X. Wang, G. Koleilat, A. Fischer, J. Tang, R. Debnath, L. Levina, E.H. Sargent, *Enhanced open-circuit voltage in visible quantum dot*

photovoltaics by engineering of carrier-collecting electrodes. ACS Applied Materials & Interfaces, 2011. **3**: p. 3792-3795.

37. H. Liu, J. Tang, I.J. Kramer, R. Debnath, G.I. Koleilat, X. Wang, A. Fisher, R. Li, L. Brzozowski, L. Levina, E.H. Sargen, *Electron acceptor materials engineering in colloidal quantum dot solar cells.* Advanced Materials, 2011. **23**(33): p. 3832-3837.

38. K.P. Fritza, S. Guenes, J. Luther, S. Kumar, N.S. Sariciftci, G.D. Scholes, *IV–VI nanocrystal polymer solar cells.* Journal of Photochemistry and Photobiology A: Chemistry, 2008. **195**(1): p. 39-46.

39. S.W. Tsang, H. Fu, R. Wang, J. Lu, K. Yu, Y. Tao, *Highly efficient cross-linked PbS nanocrystal/C60 hybrid heterojunction photovoltaic cells.* Applied Physics Letters, 2009. **95**(18): p. 183505-183508.

40. K.M. Noone, E. Strein, N.C. Anderson, P.T. Wu, S.A. Jenekhe, D.S. Ginger, *Broadband absorbing bulk heterojunction photovoltaics using low-bandgap solution-processed quantum dots.* Nano Letters, 2010. **10**(7): p. 2635-2639.

41. S.W. Tsang, H. Fu, J. Ouyang, Y. Zhang, K. Yu, J. Lu,Y. Tao, *Self-organized phase segregation between inorganic nanocrystals and PC61BM for hybrid high-efficiency bulk heterojunction photovoltaic cells.* Applied Physics Letters, 2010. **96**(24): p. 243104-243107.

42. S. Dayal, N. Kopidakis, D.C. Olson, D.S. Ginley, G. Rumbles, *Photovoltaic devices with a low band gap polymer and CdSe nanostructures exceeding 3% efficiency.* Nano Letters, 2009. **10**(1): p. 239-242.

43. S.H. Im, H.J. Kim, S. Kim, S.W. Kim, S. Seok, *Improved air stability of PbS-sensitized solar cell by incorporating ethanedithiol during spin-assisted successive ionic layer adsorption and reaction.* Organic Electronics, 2012. **13**(11): p. 2352-2357.

44. V. Gonzalez-Pedro, C. Sima, G. Marzari, P.P. Boix, S. Giménez, Q. Shen, T. Dittrich, I. Mora-Seró, *High performance PbS quantum dot sensitized solar cells exceeding 4% efficiency: The role of metal precursors in the electron injection and charge separation.* Physical Chemistry Chemical Physics, 2013. **15**(33): p. 13835-13843.

45. Y. Li, L. Wei, X. Chen, R. Zhang, X. Sui, Y. Chen, J. Jiao, L. Mei, *Efficient PbS/CdS co-sensitized solar cells based on TiO_2 nanorod arrays.* Nanoscale Research Letters, 2013. **8**(1): P. 67.

46. C. Justin Raj, S.N. Karthick, S. Park, K.V. Hemalatha, S.K. Kim, K. Prabakar, H.J. Kim, *Improved photovoltaic performance of CdSe/CdS/PbS quantum dot sensitized ZnO nanorod array solar cell.* Journal of Power Sources, 2014. **248**: p. 439-446.

47. J. Jiao, Z.J. Zhou,W.H. Zhou, S.X. Wu, *CdS and PbS quantum dots co-sensitized TiO_2 nanorod arrays with improved performance for solar cells application.* Materials Science in Semiconductor Processing, 2013. **16**(2): p. 435-440.

48. N. Zhou, G. Chen, X. Zhang, L. Cheng, Y. Luo, D. Li, Q. Meng, *Highly efficient PbS/CdS co-sensitized solar cells based on photoanodes with hierarchical pore distribution.* Electrochemistry Communications, 2012. **20**(0): p. 97-100.

49. A. Henglein, *Small-particle research: physicochemical properties of extremely small colloidal metal and semiconductor particles.* Chemical Reviews, 1989. **89**(8): p. 1861-1873.

50. T. Trindade, P. O'Brien, N.L. Pickett, *Nanocrystalline semiconductors: Synthesis, properties, and perspectives.* Chemistry of Materials, 2001. **13**(11): p. 3843-3858.

51. S. Kuchibhatla, A.S. Karakoti, D. Bera, S. Seal, *One dimensional nanostructured materials.* Progress in Materials Science, 2007. **52**(5): p. 699-913.

52. D. Bera, S.C. Kuiry, S, Seal, *Synthesis of nanostructured materials using template-assisted electrodeposition.* JOM, 2004. **56**(1): p. 49-53.

53. D. Bera, L. Qian, T.K. Tseng, P.H. Holloway, *Quantum dots and their multimodal applications: A review.* Materials, 2010. **3**(4): p. 2260-2345.

54. V.I. Klimov, *Mechanisms for photogeneration and recombination of multiexcitons in semiconductor nanocrystals: implications for lasing and solar energy conversion.* The Journal of Physical Chemistry B, 2006. **110**(34): p. 16827-16845.

55. D.J. Griffiths, *Introduction to quantum mechanics.* 2nd edition, Prentice-Hall. 1995, New Jersey.

56. K. Tvrdy, P.V. Kamat, *Quantum dot solar cells in comprehensive nanoscience and technology*, ed. D.L. Andrews, G.D. Scholes, and G. P. Wiederrecht. 2011, Oxford: Academic Press.

57. D.V. Talapin, C.B. Murray, *PbSe nanocrystal solids for n- and p-channel thin film field-effect transistors.* Science, 2005. **310**(5745): p. 86-89.

58. Y. Dong, C. Wang, B.L. Wehrenberg, P. Guyot-Sionnest, *Variable range hopping conduction in semiconductor nanocrystal solids.* Physical Review Letters, 2004. **92**(21): p. 6802.

59. A. Pandey, P. Guyot-Sionnest, *Slow electron cooling in colloidal quantum dots.* Science, 2008. **322**(5903): p. 929-932.

60. J.H. Bang, P.V. Kamat, *Quantum dot sensitized solar cells. A tale of two semiconductor nanocrystals: CdSe and CdTe.* ACS Nano, 2009. **3**(6): p. 1467-1476.

61. R.D. Schaller, V.I. Klimov, *High efficiency carrier multiplication in PbSe nanocrystals: implications for solar energy conversion.* Physical Review Letters, 2004. **92**(18): p. 186601.

62. V. Sukhovatkin, S. Hinds, L. Brzozowski, E.H. Sargent, *Colloidal quantum-dot photodetectors exploiting multiexciton generation.* Science, 2009. **324**(5934): p. 1542-1544.

63. R.J. Ellingson, M.C. Beard, J.C. Johnson, P. Yu, O.I. Micic, A.J. Nozik, A. Shabaev, A.L. Efros, *Highly efficient multiple exciton generation in colloidal PbSe and PbS quantum dots.* Nano Letters, 2005. **5**(5): p. 865-871.

64. A. Smith, D. Dutton, *Behavior of lead sulfide photocells in the ultraviolet.* Journal of the Optical Society of America, 1958. **48**(12): p. 1007-1009.

65. S.J. Kim, W.J. Kim, Y. Sahoo, A.N. cartwright, P.N. Prasad, *Multiple exciton generation and electrical extraction from a PbSe quantum dot photoconductor.* Applied Physics Letters, 2008. **92**(3): p. 31107.

66. S.J. Kim, W.J. Kim, A.N. cartwright, P.N. Prasad, *Carrier multiplication in a PbSe nanocrystal and P3HT/PCBM tandem cell.* Applied Physics Letters, 2008. **92**(19): p. 191107.

67. K.H. Kim, K.C. Park, D.Y. Ma, *The physical properties of Al-doped zinc oxide films prepared by RF magnetron sputtering.* Thin Solid Films, 1997. **305**(9): p. 201-209.

68. Z. Jia, L. Yue, Y. Zheng, Z. Xu, *Rod like zinc oxide constructed by nanoparticles: synthesis, characterization and optical properties.* Materials Chemistry and Physics, 2008. **107**(1): p. 137-141.

69. Q. Wan, T.H. Wang, J.C. Zhao, *Enhanced photocatalytic activity of ZnO nanotetrapods.* Applied Physics Letters, 2005. **87**(8): p. 83105- 83108.

70. H. Yan, J. Hou, Z. Fu, B. Yang, P. Yang, K. Liu, M. Wen, Y. Chen, S. Fu, F. Li, *Growth and photocatalytic properties of one-dimensional ZnO nanostructures prepared by thermal evaporation.* Materials Research Bulletin, 2009. **44**(10): p. 1954-1958.

71. Z.X. Lin, Y.A. Zhang, Y. Ye, X.T. Zhou, T.L. Guo, *Synthesis and photoelectric properties of ZnO nanostructure with different morphologies via hydrothermal method.* Materials Technology, 2012. **27**(5): p. 350-354.

72. B. Li, Y. Wang, *Facile synthesis and enhanced photocatalytic performance of flower-like ZnO hierarchical microstructures.* The Journal of Physical Chemistry C, 2009. **114**(2): p. 890-896.

73. C.X. Xu, X.W. Sun, B.J. Chen, P. Shum, S. Li, X. Hu, *Nanostructural zinc oxide and its electrical and optical properties.* Journal of Applied Physics, 2004. **95**(2): p. 661-666.

74. F.Q. He, Y.P. Zhao, *Growth of ZnO nanotetrapods with hexagonal crown.* Applied Physics Letters, 2006. **88**(19) : p. 193113.

75. S. Dagher, A. Ayesh, N. Tit, Y. Haik, *Influence of reactant concentration on optical properties of ZnO nanoparticles.* Materials Technology, 2013. **29**(2): p. 76-82.

76. R.D.K. Misra, *Quantum dots for tumor targeted drug delivery and cell imaging.* Nanomedicine, 2008. **3**: p. 271.

77. Q. Yuan, J. Shan, S. Hein, RDK. Misra, *Controlled and extended drug release behavior of chitosan-based nanoparticle carrier.* Acta Biomaterialia, 2010. **6**: p. 1140-1148.

78. D.J. Chadi, K.J. Chang, *Theory of the atomic and electronic structure of alloys.* Physical Review Letters, 1988. **61**(7): p. 873-876.

79. A. Janotti, C.G.Van de Walle, *Native point defects in ZnO.* Physical Review B, 2007. **76**(16): p. 165202.

80. D. Dutta, B.C. Wood, S.Y. Bhide, K. Ganapathy Ayappa, S. Narasimhan, *Enhanced gas adsorption on graphitic substrates via defects and local curvature: A density functional theory study.* The Journal of Physical Chemistry C, 2014. **118**: p. 7741-7750.

81. N. Tit, S. Dagher, A. Ayesh, Y. Haik, *Bowing character in wurtzite ZnO-based ternary alloys.* Journal of Electronic Materials, 2012. **41**(11): p. 3111-3118.

82. S. Kouser, U.V. Waghmare, N. Tit, *Adsorption and splitting of H_2S on 2D-ZnO1-xNy: first-principles analysis.* Physical Chemistry Chemical Physics, 2014. **16**(22): p. 10719-10726.

83. X. XU, Z. Jin, C. Xu, J. Guo, Z. Shi, J. Pan, J. Hu, *Defect-origin and stability of visible emission in ZnO nanopillars.* Functional Materials Letters, 2012. **05**(03): p. 1240001.

84. S. Wei, J. Lian, H. Wu, *Annealing effect on the photoluminescence properties of ZnO nanorod array prepared by a PLD-assistant wet chemical method.* Materials Characterization, 2010. **61**(11): p. 1239-1244.

85. B. Lin, Z. Fu, *Green luminescent center in undoped zinc oxide films depositedon silicon substrates.* Appied Physics Letters, 2001. **79**(7): p. 943.

86. T. Kawano, H. Imai, *A simple preparation technique for shape-controlled zinc oxide nanoparticles: formation of narrow size-distributed nanorods*

using seeds in aqueous solutions. Colloids and Surfaces, A: Physicochemical and Engineering Aspects 2008. **319**(1-3): p. 130-135.

87. E.A. Meulenkamp, *Synthesis and growth of ZnO nanoparticles.* The Journal of Physical Chemistry B, 1998. **102**(29): p. 5566-5572.

88. P. Li, Y. Wei, H. Liu, X. Wang, *Growth of well-defined ZnO microparticles with additives from aqueous solution.* Journal of Solid State Chemistry, 2005. **178**(3): p. 855-860.

89. B. Liu, H.C. Zeng, *Fabrication of ZnO "dandelions" via a modified kirkendall process.* Journal of the American Chemical Society, 2004. **126**(51): p. 16744-16746.

90. B. Liu, H.C. Zeng, *Hydrothermal synthesis of ZnO nanorods in the diameter regime of 50 nm.* Journal of the American Chemical Society, 2003. **125**(15): p. 4430-4431.

91. Z. Hu, G. Oskam, P.C. Searson, *Influence of solvent on the growth of ZnO nanoparticles.* Journal of Colloid and Interface Science, 2003. **263**(2): p. 454-460.

92. R.I. Bickley, T. Gonzalez-Carreno, J.S. Lees, L. Palmisano, R. Tilley, *A structural investigation of titanium dioxide photocatalysts.* Journal of Solid State Chemistry, 1991. **92**(1): p. 178-190.

93. A. Fujishima, T.N. Rao, D.A. Tryk, *Titanium dioxide photocatalysis.* Journal of Photochemistry and Photobiology C: Photochemistry Reviews, 2000. **1**(1): p. 1-21.

94. J.M. Wu, S. Hayakawa, K. Tsuru, A. Osaka, *In vitro bioactivity of anatase film obtained by direct deposition from aqueous titanium tetrafluoride solutions.* Thin Solid Films, 2002. **414**(2): p. 275-280.

95. G. Ramakrishna, H.N. Ghosh, *Emission from the charge transfer state of xanthene dye-sensitized TiO_2 nanoparticles: A new approach to determining back electron transfer rate and verifying the marcus inverted regime.* The Journal of Physical Chemistry B, 2001. **105**(29): p. 7000-7008.

96. M. Andersson, L. Osterlund, S. Ljungstro, A. Palmqvist, *Preparation of nanosize anatase and rutile TiO_2 by hydrothermal treatment of microemulsions and their activity for photocatalytic wet oxidation of phenol.* The Journal of Physical Chemistry B, 2002. **106**(41): p. 10674-10679.

97. K. Zakrzewska, *Mixed oxides as gas sensors.* Thin Solid Films, 2001. **391**(2): p. 229-238.

98. D.K. Yi, S.J. Yoo, D.Y. Kim, *Spin-on-based fabrication of titania nanowires using a sol-gel process.* Nano Letters, 2002. **2**(10): p. 1101-1104.

99. Z. Miao, D. Xu, J. Ouyang, G. Guo, X. Zhao, Y. Tang, *Electrochemically induced sol−gel preparation of single-crystalline* TiO_2 *nanowires.* Nano Letters, 2002. **2**(7): p. 717-720.

100. J.J. Wu, C.C. Yu, *Aligned* TiO_2 *nanorods and nanowalls.* The Journal of Physical Chemistry B, 2004. **108**(11): p. 3377-3379.

101. Y., Lei, L.D. Zhang, J.C. Fan, *Fabrication, characterization and raman study of* TiO_2 *nanowire arrays prepared by anodic oxidative hydrolysis of* $TiCl_3$. Chemical Physics Letters, 2001. **338**(4): p. 231-236.

102. Y. Zhu, H. Li, Y. Koltypin, Y.R. Hacohen, A. Gedanken, *Sonochemical synthesis of titania whiskers and nanotubes.* Chemical Communications, 2001(24): p. 2616-2617.

103. G. Wang, G. Li, *Titania from nanoclusters to nanowires and nanoforks.* The European Physical Journal D-Atomic, Molecular, Optical and Plasma Physics, 2003. **24**(1): p. 355-360.

104. C. Xu, Y. Zhan, K. Hong, G. Wang, *Growth and mechanism of titania nanowires.* Solid State Communications, 2003. **126**(10): p. 545-549.

105. Y.V. Kolen'ko, K.A. Kovnir, A.I. Gavrilov, A.V. Garshev, J. Frantti, O.I. Lebedev, B.R. Churagulov, G.V. Tendeloo, M. Yoshimura. *Hydrothermal synthesis and characterization of nanorods of various titanates and titanium dioxide.* The Journal of Physical Chemistry B, 2006. **110**(9): p. 4030-4038.

106. C. Kormann, D.W. Bahnemann, M.R. Hoffmann, *Preparation and characterization of quantum-size titanium dioxide.* The Journal of Physical Chemistry, 1988. **92**(18): p. 5196-5201.

107. H. Cheng, J. Ma, Z. Zhao, L. Qi, *Hydrothermal preparation of uniform nanosize rutile and anatase particles.* Chemistry of Materials, 1995. **7**(4): p. 663-671.

108. Q. Zhang, L. Gao, J. Gao, *Effect of hydrolysis conditions on morphology and crystallization of nanosized* TiO_2 *powder.* Journal of the European Ceramic Society, 2000. **20**(12): p. 2153-2158.

109. D.S. Lee, T.K. Liu, *Preparation of* TiO_2 *Sol using* $TiCl_4$ *as a precursor.* Journal of Sol-Gel Science and Technology, 2002. **25**(2): p. 121-136.

110. K. Yanagisawa, J. Ovenstone, *Crystallization of anatase from amorphous titania using the hydrothermal technique: effects of starting material and temperature.* The Journal of Physical Chemistry B, 1999. **103**(37): p. 7781-7787.

111. A. Pottier, C. Chane´ac, E. Tronc, L. Mazerolleset, J.P. Jolivet, *Synthesis of brookite TiO_2 nanoparticles by thermolysis of TiCl in strongly acidic aqueous media.* Journal of Materials Chemistry, 2001. **11**(4): p. 1116-1121.

112. M. Addamo, V. Augugliaro, A.D. Paola, E. García-López, V. Loddo, G. Marcì, L. Palmisano, *Preparation and photoactivity of nanostructured TiO_2 particles obtained by hydrolysis of $TiCl_4$.* Colloids and Surfaces A: Physicochemical and Engineering Aspects, 2005. **265**(1–3): p. 23-31.

113. M. Gupta, V. Sharma, J. Shrivastavaet, A. Solanki, A.P. Singhal, S. Dass, R. Shrivastav, *Preparation and characterization of nanostructured ZnO thin films for photoelectrochemical splitting of water.* Bulletin of Materials Science, 2009. **32**(1): p. 23-30.

114. B.R. Hyun, Y.W. Zhong, A.C. Bartnik, L. Sun, H.D. Abruña, F.W. Wise, J.D. Goodreau, J.R. Matthews, T.M. Leslie, N.F. Borrelli, *Electron injection from colloidal PbS quantum dots into titanium dioxide nanoparticles.* ACS Nano, 2008. **2**(11): p. 2206-2212.

115. K. Gerasimos, I. Howard, A. Fischer, S. Hoogland, J. Clifford, E. Klem, L. Levina, E.H. Sargent, *Ultrasensitive solution-cast quantum dot photodetectors.* Nature, 2006. **442**(7099): p. 180-183.

116. R.S. Kane, S. Roszak, J. Leszczynski, *Theoretical study of the electronic structure of PbS nanoclusters.* The Journal of Physical Chemistry, 1996. **100**(19): p. 7928-7932.

117. A.C. Pan, C. del Cañizo, E. Cánovas, N.M. Santos, J.P. Leitão, A. Luque, *Enhancement of up-conversion efficiency by combining rare earth-doped phosphors with PbS quantum dots.* Solar Energy Materials and Solar Cells, 2010. **94**(11): p. 1923-1926.

118. L. Xu, W. Zhang, Y. Ding, W. Yu, J. Xing, F. Li, Y. Qian, *Shape-controlled synthesis of PbS microcrystals in large yields via a solvothermal process.* Journal of Crystal Growth, 2004. **273**(1–2): p. 213-219.

119. S.F. Wang, F. Gu, M.K. Lü, D.Z. Wang, Z.S. Yang, H.P. Zhang, Y.Y. Zhou, A.Y. Zhang, *Synthesis of cross-shaped PbS nanostructures by a surfactant-assisted reflux process.* Materials Letters, 2006. **60**(21–22): p. 2759-2763.

120. Y.C. Zhang, *T.* Qiao, X.Y. Hu, G.Y. Wang, X. Wu, *Shape-controlled synthesis of PbS microcrystallites by mild solvotherma l decomposition of a single-source molecular precursor.* Journal of Crystal Growth, 2005. **277**(1–4): p. 518-523.

121. S. M. Zhou, X.H. Zhang, X.M. Meng, X. Fan, S.T. Lee, S.K. Wu, *Sonochemical synthesis of large-scale single-crystal PbS nanorods.* Journal of Materials Research, 2003. **18**(05): p. 1188-1191.

122. U.K. Gautam, R. Seshadri, *Preparation of PbS and PbSe nanocrystals by a new solvothermal route.* Materials Research Bulletin, 2004. **39**(4–5): p. 669-676.

123. O.E. Semonin, J.M. Luther, S. Choi, H.Y. Chen, J. Gao, A.J. Nozik, M.C. Beard, *Peak external photocurrent quantum efficiency exceeding 100% via MEG in a quantum dot solar cell.* Science, 2011. **334**(6062): p. 1530-1533.

124. R.L. Sandberg, L.A. Padilha, M.M. Qazilbash, W.K. Bae, R.D. Schaller, J.M. Pietryga, M.J. Stevens, B. Baek, S.W. Nam, V.I. Klimov, *Multiexciton dynamics in infrared-emitting colloidal nanostructures probed by a superconducting nanowire single-photon detector.* ACS Nano, 2012. **6**(11): p. 9532-9540.

125. P.D. Cunningham, J.E. Boercker, E.E. Foos, M.P. Lumb, A.R. Smith, J.G. Tischler, J.S. Melinger, *Enhanced multiple exciton generation in quasi-one-dimensional Semiconductors.* Nano Letters, 2011. **11**(8): p. 3476-3481.

126. F.W. Wise, *Lead salt quantum dots: the limit of strong quantum confinement.* Accounts of Chemical Research, 2000. **33**(11): p. 773-780.

127. L. Cademartiri, E. Montanari, G. Calestani, A. Migliori, A. Guagliardi, G.A. Ozin, *Size-dependent extinction coefficients of PbS quantum dots.* Journal of the American Chemical Society, 2006. **128**(31): p. 10337-10346.

128. L. Bakueva, I. Gorelikov, S. Musikhin, X.S. Zhao, E.H. Sargent, E. Kumacheva, *PbS quantum dots with stable efficient luminescence in the near-IR spectral range.* Advanced Materials, 2004. **16**(11): p. 926-929.

129. H. Fu, S.W. Tsang, *Infrared colloidal lead chalcogenide nanocrystals: Synthesis, properties, and photovoltaic applications.* Nanoscale, 2012. **4**(7): p. 2187-2201.

130. M.A. Hines, G.D. Scholes, *Colloidal PbS nanocrystals with size-tunable near-infrared emission: observation of post-synthesis self-narrowing of the particle size distribution.* Advanced Materials, 2003. **15**(21): p. 1844-1849.

131. S. Maenosono, T. Okubo, Y. Yamaguchi, *Overview of nanoparticle array formation by wet coating.* Journal of Nanoparticle Research, 2003. **5**(1-2): p. 5-15.

132. J. Tang, G. Konstantatos, S. Hinds, S. Myrskog, A.G. Pattantyus-Abraham, J. Clifford, E.H. Sargent, *Heavy-metal-free solution-processed nanoparticle-based photodetectors: doping of intrinsic vacancies enables engineering of sensitivity andspeed.* Acs Nano, 2009. **3**(2): p. 331-338.

133. H.M. Haverinen, R.A. Myllylä, G.E. Jabbour, *Inkjet printing of light emitting quantum dots.* Applied Physics Letters, 2009. **94**(7): p.73108-73111.

134. M. Singh, H.M. Haverinen, P. Dhagat, G.E. Jabbour, *Inkjet printing-process and its applications.* Advanced Materials, 2010. **22**(6): p. 673-685.

135. H.M. Haverinen, R.A. Myllylä, G.E. Jabbour, *Inkjet printed RGB quantum dot-hybrid LED.* IEEE/OSA Journal of Display Technology, 2010. **6**(3): p. 87-89.

136. A.S. Sall, M. Gaye, O. Sarr, A. Caneschi, V.D. Noto, M. Vidali, *Preparation of the new binucleating ligand 2,6-bis(carboxymethylsulfanylmethyl)-4-methylphenol and its mono- and bi-nuclear complexes.* Journal of Chemical Research, Synopses, 1997. (10): p. 347-347.

137. P. Guyot-Sionnest, B. Wehrenberg, D. Yu, *Intraband relaxation in CdSe nanocrystals and the strong influence of the surface ligands.* The Journal of Chemical Physics, 2005. **123**(7): p. 74709.

138. G. Konstantatos, I. Howard, A. Fischer, S. Hoogland, J. Clifford, E. Klem, L. Levina, E.H. Sargent, *Ultrasensitive solution-cast quantum dot photodetectors.* Nature, 2006. **442**(7099): p. 180-183.

139. C. Leatherdale, C.R. Kagan, N.Y. Morgan, S.A. Empedocles, M.A. Kastner, M.G. Bawendi, *Photoconductivity in CdSe quantum dot solids.* Physical Review B, 2000. **62**(4): p. 2669-2680.

140. J.E. Murphy, M.C. Beard, A.J. Nozik, *Time-resolved photoconductivity of PbSe nanocrystal arrays.* Journal of Physical Chemistry B, 2006. **110**(50): p. 25455-25461.

141. D. Yu, C. Wang, P.G. Sionnest, *n-Type Conducting CdSe nanocrystal solids.* Science, 2003. **300**(5623): p. 1277-1280.

142. K.S. Jeong, J. Tang, H. Liu, J. Kim, A.W. Schaefer, K. Kemp, L. Levina, X. Wang, s. Hoogland, R. Debanth, L. Brzozowski, E.H. Sargent, J.B. Asbury. *Enhanced mobility-lifetime products in PbS colloidal quantum dot photovoltaics.* ACS Nano, 2011. **6**(1): p. 89-99.

143. S. Ghosh, K. Das, K. Chakrabarti, S.K. De, *Effect of oleic acid ligand on photophysical, photoconductive and magnetic properties of monodisperse SnO_2 quantum dots.* Dalton Transactions, 2013. **42**(10): p. 3434-3446.

144. T. Jiang, K.Kemp, S. Hoogland, K. Jeong, H. Liu, L. Levina, M. Furukawa, X. Wang R. Debnath, D. Cha, K. Chou, A. Amassian, J. Asbury, E.H. Sargent, *Colloidal-quantum dot photovoltaics using atomic-ligand passivation.* Nature Materials, 2011. **10**(10): p. 765-771.

145. S.Y. Sung, S.Y. Kim, K.M. Jo, J.H. Lee, J.J. Kim, S.G. Kim, K.H. Chai, S.J. Pearton, D.P. Norton, Y.W. He, *Fabrication of p-channel thin-film transistors using CuO active layers deposited at low temperature.* Applied Physics Letters, 2010. **97**(22): p. 222109.

146. J. Morales, L. Sánchez, F. Martín, J.R. Ramos-Barrado, M. Sánchez, *Use of low-temperature nanostructured CuO thin films deposited by spray-pyrolysis in lithium cells.* Thin Solid Films, 2005. **474**(1-2): p. 133-140.

147. A. Cruccolini, R. Narducci, R. Palombar, *Gas adsorption effects on surface conductivity of nonstoichiometric CuO.* Sensors and Actuators B: Chemical, 2004. **98**(2-3): p. 227-232.

148. V.R. Katti, A.K. Debnath, K.P. Muthe, M. Kaur, A.K. Dua, S.C. Gadkari, S.K. Gupta, V.C. Sahni, *Mechanism of drifts in H_2S sensing properties of SnO_2:CuO composite thin film sensors prepared by thermal evaporation.* Sensors and Actuators B-chemical, 2003. **96**(1): p. 245-252.

149. M. Frietsch, F. Zudock, J. Goschnicke, M. Bruns, *CuO catalytic membrane as selectivity trimmer for metal oxide gas sensors.* Sensors and Actuators B: Chemical, 2000. **65**(1–3): p. 379-381.

150. H. Fan, L. Yang, W. Hua, X. Wu, Z. Wu, S. Xie, B. Zou, *Controlled synthesis of monodispersed CuO nanocrystals.* Nanotechnology, 2004. **15**(1): p. 37-42.

151. J.C. Mallinson, *The foundations of magnetic recording*. Academic Press, 1987, Berkeley, CA.

152. P.O. Larsson, A. Andersson, R. Wallenberg, B. Svensson, *Combustion of CO and toluene; characterisation of copper oxide supported on titania and activity comparisons with supported cobalt, iron, and manganese oxide.* Journal of Catalysis, 1996. **163**(2): p. 279-293.

153. C.T. Hsieh, J.M. Chen, H.H. Lin, H.C. Shin, *Field emission from various Cuo nanostructures.* Applied Physics Letters, 2003. **83**(16): p. 3383-3385.

154. K. Koumoto, H. Koduka, W.S. Seo, *Thermoelectric properties of single crystal $CuAlO_2$ with a layered structure.* Journal of Materials Chemistry, 2001. **11**(2): p. 251-252.

155. S. Lee, S.U.S. Choi, S. Li, J.A. Eastman, *Measuring thermal conductivity of fluids containing oxide nanoparticles.* Journal of Heat Transfer-transactions of The Asme, 1999. **121**(2): p. 280-289.

156. Y. Jiang, S. Decker, C. Mohs, K.J. Klabunde, *Catalytic solid state reactions on the surface of nanoscale metal oxide particles.* Journal of Catalysis, 1998. **180**(1): p. 24-35.

157. A. Santos, P. Yustos, A. Quintanilla, G. Ruiz, F. Garcia-Ochoa, *Study of the copper leaching in the wet oxidation of phenol with CuO-based catalysts: Causes and effects.* Applied Catalysis B: Environmental, 2005. **61**(3–4): p. 323-333.

158. S.A. Roh, S.H. Jung, S.M. Jeong , S.D. Kim, *Selective catalytic reduction by urea in a fluidized-bed reactor.* Journal of Chemical Technology & Biotechnology, 2003. **78**(10): p. 1104-1109.

159. S. Rajagopalan, O. Koper, S. Decker, K.J. Klabunde, *Nanocrystalline metal oxides as destructive adsorbents for organophosphorus compounds at ambient temperatures.* Chemistry - A European Journal, 2002. **8**(11): p. 2602-2607.

160. K.J. Klabunde, *Introduction to nanotechnology*, in *nanoscale materials in chemistry*. 2002, John Wiley & Sons, Inc. p. 1-13.

161. K.J. Klabunde, J. Stark, O. Koper, C. Mohs, D.G. Park, S. Decker Y. Jyang, I. Lagadic, D. Zhang, *Nanocrystals as stoichiometric reagents with unique surface chemistry.* The Journal of Physical Chemistry, 1996. **100**(30): p. 12142-12153.

162. J.A. Rodriguez, M. Fernandez Garcia, *Synthesis properties and applications of oxide nanomaterials*, John Wiley and Sons. 2007, New York

163. M. Winter, D. Hmal, X. Yang, H. Kwen, D. Jones, S. Rajagopalan, K.J. Klabunde, *Defining reactivity of solid sorbents: What is the most appropriate metric?* Chemistry of Materials, 2009. **21**(12): p. 2367-2374.

164. A. Hagfeldt, M. Graetzel, *Light-induced redox reactions in nanocrystalline systems.* Chemical Reviews, 1995. **95**(1): p. 49-68.

165. H.Wang, J.Z. Xu, J.J. Zhu, H.Y. Chen, *Preparation of CuO nanoparticles by microwave irradiation.* Journal of Crystal Growth, 2002. **244**(1): p. 88-94.

166. K.J. Rao, B. Vaidhantha, m. Ganguli, P.A. Ramakrishnan, *Synthesis of inorganic solids using microwaves.* Chemistry of Materials, 1999. **11**(4): p. 882-895.

167. S. Komarneni, M.C. D'Arrigo, C. Leonelli, G.C. Pellacani, H. Katsuki, *Microwave-hydrothermal synthesis of nanophase ferrites.* Journal of the American Ceramic Society, 1998. **81**(11): p. 3041-3043.

168. S. Komarneni, R.K.Rajha, H. Katsuki, *Microwave-hydrothermal processing of titanium dioxide.* Materials Chemistry and Physics, 1999. **61**(1): p. 50-54.

169. L.S. Cavalcante, J.C. Sczancoski, R.L. Tranquilin, J.A. Varela, E. Longo, M.O. Orlandi, *Growth mechanism of octahedron-like $BaMoO_4$ microcrystals processed in microwave-hydrothermal: Experimental observations and computational modeling.* Particuology, 2009. **7**(5): p. 353-362.

170. R. Vijaya Kumar, R. Elgamiel, Y. Diamant, A. Gedanken, J. Norwig, *Sonochemical preparation and characterization of nanocrystalline copper oxide embedded in poly (vinyl alcohol) and its effect on crystal growth of copper oxide.* Langmuir, 2001. **17**(5): p. 1406-1410.

171. M.H. Chang, H.S. Liu, C.Y. Tai, *Preparation of copper oxide nanoparticles and its application in nanofluid.* Powder Technology, 2011. **207**(1–3): p. 378-386.

172. D. Das, B.C. Nath, P. Phukon, S.K. Dolui, *Synthesis and evaluation of antioxidant and antibacterial behavior of CuO nanoparticles.* Colloids and Surfaces B: Biointerfaces, 2013. **101**: p. 430-433.

173. D. Jia, J. Yu, X. Xia, *Synthesis of CuO nanometer powder by one step solid state reaction at room temperature.* Chinese Science Bulletin, 1998. **43**(7): p. 571-573.

174. W. Jisen, Y. Jinkai, S. Jinquan, B. Ying, *Synthesis of copper oxide nanomaterials and the growth mechanism of copper oxide nanorods.* Materials & Design, 2004. **25**(7): p. 625-629.

175. D. Han, H. Yang, C. Zhu, F. Wang, *Controlled synthesis of CuO nanoparticles using TritonX-100-based water-in-oil reverse micelles.* Powder Technology, 2008. **185**(3): p. 286-290.

176. S. Rehman, A. Mumtaz, S.K. Hasanain, *Size effects on the magnetic and optical properties of CuO nanoparticles.* Journal of Nanoparticle Research, 2011. **13**(6): p. 2497-2507.

177. C.L. Carnes, J. Stipp, K.J. Klabunde, *Synthesis, characterization, and adsorption studies of nanocrystalline copper oxide and nickel oxide.* Langmuir, 2002. **18**(4): p. 1352-1359.

178. A.A. Eliseev, A.V. Lukashin, A.A. Vertegel, L.I. Heifet, A.I. Zhirov, Y.D. Tretyakov, *Complexes of Cu(II) with polyvinyl alcohol as precursors for the preparation of CuO/SiO_2 nanocomposites.* Materials Research Innovations, 2000. **3**(5): p. 308-312.

179. Z.S. Hong, Y. Cao, J. Deng, *A convenient alcohothermal approach for low temperature synthesis of CuO nanoparticles.* Materials Letters, 2002. **52**(1–2): p. 34-38.

180. A. El-Trass, E. El-Shamy, I. El-Mehaseb, M. El-Kemary, *CuO nanoparticles: Synthesis, characterization, optical properties and interaction with amino acids.* Applied Surface Science, 2012. **258**(7): p. 2997-3001.

181. K. Borgohain, J.B. Singh, M.V. Rama Rao, T. Shribathi, S. Mahamuni, *Quantum size effects in CuO nanoparticles.* Physical Review B, 2000. **61**(16): p. 11093-11096.

182. M. Sahooli, S. Sabbagi, R. Saboori, *Synthesis and characterization of mono sized CuO nanoparticles.* Materials Letters, 2012. **81**(0): p. 169-172.

183. D.I. Son, C.H. You, T.W. Kim, *Structural, optical, and electronic properties of colloidal CuO nanoparticles formed by using a colloid-thermal synthesis process.* Applied Surface Science, 2009. **255**(21): p. 8794-8797.

184. S. Chandramohan, A. Kanjilal, T. Strache, J.K. Tripathi, S.N. Sarangi, R. Sathyamoorthy, T. Som, *Modifications in structural and optical properties of Mn-ion implanted CdS thin films.* Applied Surface Science, 2009. **256**(2): p. 465-468.

185. P.K. Weimer, *The TFT a new thin-film transistor.* Proceedings of the IRE, 1962. **50**(6): p. 1462-1469.

186. A.P. Odrinskii, *A critical analysis of investigation of deep levels in high-resistivity CdS single crystals by photoelectric transient spectroscopy.* Semiconductors, 2004. **38**(3): p. 298-303.

187. F. El-Tantawy, K.M Abdel-Kader, F. Kaneko, Y.K. Sung, *Physical properties of CdS-poly (vinyl alcohol) nanoconducting composite synthesized by organosol techniques and novel application potential.* European Polymer Journal, 2004. **40**(2): p. 415-430.

188. R. Mishra, K.J. Rao, *Thermal and morphological studies of binary and ternary composites of poly(vinylalcohol) with alumina and zirconia.* Ceramics International, 2000. **26**(4): p. 371-378.

189. R. Faez, I.M. Martin, M.A. De Baoli, M.C. Rezende, *Influence of processing time and composition in the microwave absorption of EPDM/PAni blends.* Journal of Applied Polymer Science, 2002. **83**(7): p. 1568-1575.

190. J. Britt, C. Ferekides, *Thin-film CdS/CdTe solar cell with 15.8% efficiency.* Applied Physics Letters, 1993. **62**(22): p. 2851-2852.

191. X. Zong, H. Yang, G. Wu, G. Ma, F. Wen, L. Wang. C. Li, *Enhancement of photocatalytic H_2 evolution on CdS by loading MoS_2 as cocatalyst under visible light irradiation.* Journal of the American Chemical Society, 2008. **130**(23): p. 7176-7177.

192. S. Zhong, L. Zhang, Z. Huang, S. Wang, *Mixed-solvothermal synthesis of CdS micro/nanostructures and their optical properties.* Applied Surface Science, 2011. **257**(7): p. 2599-2603.

193. Z.X. Yang, W. Zhong, P. Zhang, M.H. Xu, Y. Deng, C.T. Au, Y.W. Du, *Controllable synthesis, characterization and photoluminescence properties of morphology-tunable CdS nanomaterials generated in thermal evaporation processes.* Applied Surface Science, 2012. **258**(19): p. 7343-7347.

194. X. Liu, *A facile route to preparation of sea-urchinlike cadmium sulfide nanorod-based materials.* Materials Chemistry and Physics, 2005. **91**(1): p. 212-216.

195. G. Sasikala, P. Thilakan, C. Subramanian, *Modification in the chemical bath deposition apparatus, growth and characterization of CdS semiconducting thin films for photovoltaic applications.* Solar Energy Materials and Solar Cells, 2000. **62**(3): p. 275-293.

196. A.I. Oliva, R. Castro-Rodríguez, O. Solís-Canto, V. Sosaet, P. Quintana, J.L. Peña, *Comparison of properties of CdS thin films grown by two techniques.* Applied Surface Science, 2003. **205**(1–4): p. 56-64.

197. K. Ravichandran, P. Philominathan, *Investigations on microstructural and optical properties of CdS films fabricated by a low-cost, simplified spray technique using perfume atomizer for solar cell applications.* Solar Energy, 2008. **82**(11): p. 1062-1066.

198. R. Lozada-Morales, O. Zelaya-Angel, S. Jiménez-Sandoval, G. Torres-Delgado, *Extra Raman modes in CdS during cubic to hexagonal structural transformation.* Journal of Raman Spectroscopy, 2002. **33**(6): p. 460-465.

199. K. Wright, J.D. Gale, *Interatomic potentials for the simulation of the zinc-blende and wurtzite forms of* nS and CdS: Bulk structure, properties, and phase stability**.** Physical Review B, 2004. **70**(3): p. 035211.

200. E.O. Filatova, J.M. André, E.Y. Taracheva, A.J. Tvaladze, V.L. Kraizman, A.A. Novakovich, R.V. Vedrinskii, *Experimental and theoretical studies of orientational dependence of x-ray reflectivity in vicinity of S Kedge in hexagonal CdS crystal.* Journal of Physics-condensed Matter, 2004. **16**(25): p. 4597-4606.

201. C.Y. Yeh, Z.W. Lu, S. Froyen, A. Zunger, *Zinc-blende wurtzite polytypism in semiconductors.* Physical Review B, 1992. **46**(16): p. 10086.

202. K. Subba Ramaiah, V. Sundara Raja, M. Sharon, *Optical and structural investigations on spray-deposited CdS films.* Journal of Materials Science: Materials in Electronics, 1998. **9**(4): p. 261-265.

203. C.T. Tsai, D.S. Chu, G.L. Chen, S.L. Yang, *Studies of grain size effects in rf sputtered CdS thin films.* Journal of Applied Physics, 1996. **79**(12): p. 9105-9109.

204. B.S. Moon, J.H. Lee, H. Jung, *Comparative studies of the properties of CdS films deposited on different substrates by R.F. sputtering.* Thin Solid Films, 2006. **511–512**: p. 299-303.

205. H. Bayhan, C. Erçelebi, *Electrical characterization of vacuum-deposited n-CdS/p-CdTe heterojunction devices.* Semiconductor Science and Technology, 1997. **12**(5): p. 600.

206. H.C. Chou, A. Rohatgi, *The impact of MOCVD growth ambient on carrier transport, defects, and performance of CdTe/CdS heterojunction solar cells.* Journal of Electronic Materials, 1994. **23**(1): p. 31-37.

207. O. Vigil, I. Riech, M. Garcia-Rocha, O. Zelaya-Angel, *Characterization of defect levels in chemically deposited CdS films in the cubic-to-hexagonal phase transition.* Journal of Vacuum Science & Technology A, 1997. **15**(4): p. 2282-2286.

208. C. Guillén, M.A. Martinez, J. Herrero, *Accurate control of thin film CdS growth process by adjusting the chemical bath deposition parameters.* Thin Solid Films, 1998. **335**(1–2): p. 37-42.

209. Y. Li, L. Wei, X. Chen, R. Zhang, X. Sui, Y. Chen, J. Jiao, L. Mei, *Efficient PbS/CdS co-sensitized solar cells based on* TiO_2 *nanorod arrays.* Nanoscale Research Letters, 2013. **8**(1): p. 1-7.

210. R.S. Mane, B.R. Sankapal, C.D. Lokhande, *Photoelectrochemical cells based on chemically deposited nanocrystalline* Bi_2S_3 *thin films.* Materials Chemistry and Physics, 1999. **60**(2): p. 196-203.

211. A. Jana, C. Bhattacharya, S. Sinha, *Study of the optimal condition for electroplating of* Bi_2S_3 *thin films and their photoelectrochemical characteristics.* Journal of Solid State Electrochemistry, 2009. **13**(9): p. 1339-1350.

212. K. Yao, W.W. Gong, Y.F. Hu, X.L. Liang, Q. Chen, L.M. Peng, *Individual* Bi_2S_3 *nanowire-based room-temperature* H_2 *sensor.* The Journal of Physical Chemistry C, 2008. **112**(23): p. 8721-8724.

213. R.P. Panmand, U.V. Kawade, M.V. Kulkarni, S.K. Apti, B.B. Kale, S.W. Gosavi, *Synthesis and characterization of* Bi_2S_3 *nanocrystals in glass matrix.* Materials Science and Engineering: B, 2010. **168**(1–3): p. 161-163.

214. R. Madelung, *Data in science and technology: Semiconductors other than group IV elements and III-V compounds*, ed. R. Poerschke, **50**, Springer-Verlag. 1992, Berlin.

215. L.M. Peter, *The photoelectrochemical properties of anodic Bi_2S_3 films.* Journal of Electroanalytical Chemistry and Interfacial Electrochemistry, 1979. **98**(1): p. 49-58.

216. A.U. Ubale, A.S. Daryapurkar, R.B. Mankar , R.R. Raut, V.S. Sangawar, C.H. Bhosale, *Electrical and optical properties of Bi_2S_3 thin films deposited by successive ionic layer adsorption and reaction (SILAR) method.* Materials Chemistry and Physics, 2008. **110**(1): p. 180-185.

217. T. Zdanowicz, T. Rodziewicz, M. Zabkowska-Waclawek, *Theoretical analysis of the optimum energy band gap of semiconductors for fabrication of solar cells for applications in higher latitudes locations.* Solar Energy Materials and Solar Cells, 2005. **87**(1–4): p. 757-769.

218. B. Pejova, *Analysis of the shape of spectral dependence of absorption coefficient and stationary photoconductivity spectral response in nanocrystalline bismuth(III) sulfide thin films.* Materials Research Bulletin, 2008. **43**(11): p. 2887-2903.

219. C.D. Lokhande, A.U. Ubale, P.S.Patil, *Thickness dependent properties of chemically deposited Bi_2S_3 thin films.* Thin Solid Films, 1997. **302**(1-2): p. 1-4.

220. C.D. Lokhande, B.R Sankapal, R.S Mane, H.M Pathan, M Muller, M Giersig, H Tributsch, V Ganeshan, *Structural characterization of chemically deposited Bi_2S_3 and Bi_2Se_3 thin films.* Applied Surface Science, 2002. **187**(1–2): p. 108-115.

221. J.D. Desai, C.D. Lokhande, *Nonaqueous chemical bath deposition of Bi_2S_3 thin films.* Materials Chemistry and Physics, 1993. **34**(3-4): p. 313-316.

222. S.R. Gadakh, V.V. Killedar, C.D. Lokhande, C.D. Bhosale, *Effect of complexing agent on the properties of spray-deposited Bi_2S_3 thin films.* Materials Chemistry and Physics, 1998. **56**(1): p. 79-83.

223. M. Medles, N. Benramdane, A. Bouzidi, A. Nakrela, H. Tabet-Derraz, Z. Kebbab, C. Mathieu, B. Khelifa, R. Desfeux, *Optical and electrical properties of Bi_2S_3 films deposited by spray pyrolysis.* Thin Solid Films, 2006. **497**(1–2): p. 58-64.

224. N. Benramdane, M. Latreche, H. Tabet, M. Boukhalfa, Z. Kebbab, A. Bouzidi, *Structural and optical properties of spray-pyrolysed Bi_2S_3 thin films.* Materials Science and Engineering: B, 1999. **64**(2): p. 84-87.

225. S.H. Pawar, P.N. Bhosale, M.D. Uplane, S. Tamhankar, *Growth of Bi_2S_3 film using a solution-gas interface technique.* Thin Solid Films, 1983. **110**(2): p. 165-170.

226. N.S. Yesugade, C.D. Lokhande, C.H. Bhosale, *Structural and optical properties of electrodeposited Bi_2S_3, Sb_2S_3 and As_2S_3 thin films.* Thin Solid Films, 1995. **263**(2): p. 145-149.

227. V.V Killedar, C.D. Lokhande, C.H. Bhosale, *Preparation and characterization of electrodeposited Bi_2S_3 thin films prepared from non-aqueous media.* Materials Chemistry and Physics, 2000. **64**(2): p. 166-169.

228. R.S. Mane, B.R. Sankapal, C.D. Lokhande, *A chemical method for the deposition of Bi_2S_3 thin films from a non-aqueous bath.* Thin Solid Films, 2000. **359**(2): p. 136-140.

229. S. Biswas, A. Mondal, D. Mukherjee P. Pramanik, *A Chemical Method for the Deposition of Bismuth Sulfide Thin Films.* Journal of The Electrochemical Society, 1986. **133**(1): p. 48-52.

230. J.D. Desai, C.D. Lokhande, *Chemical deposition of Bi_2S_3 thin films from thioacetamide bath.* Materials Chemistry and Physics, 1995. **41**(2): p. 98-103.

231. R.R. Ahire, B.R. Sankapal, C.D. Lokhande, *Preparation and characterization of Bi_2S_3 thin films using modified chemical bath deposition method.* Materials Research Bulletin, 2001. **36**(1–2): p. 199-210.

232. C.D. Lokhande, B.R. Sankapal, H.M. Pathan, M. Giersig, H. Tributsch, *Some structural studies on successive ionic layer adsorption and reaction (SILAR) deposited CdS thin films.* Applied Surface Science, 2001. **181**(3–4): p. 277-282.

233. B.R. Sankapal, C.D. Lokhande, *Photoelectrochemical characterization of Bi2Se3 thin films deposited by SILAR technique.* Materials Chemistry and Physics, 2002. **73**(2–3): p. 151-155.

234. HC. Schniepp, J.L. Li, M.J. Mc-Allister, M. Herrera-Alonso, D.H. Adamson, R.K. Prud'homme, R. Car, D.A. Saville, I.A. Aksay, *Functionalized single graphene sheets derived from splitting graphite oxide.* The Journal of Physical Chemistry B, 2006. **110**(17): p. 8535-8539.

235. D. Pandey, R. Reifenberger, R. Piner, *Scanning probe microscopy study of exfoliated oxidized graphene sheets.* Surface Science, 2008. **602**(9): p. 1607-1613.

236. A.K. Geim, K.S. Novoselov, *The rise of graphene.* Nature Materials, 2007. **6**(3): p. 183-191.

237. P. Sungjin, S.R. Rodney, *Chemical methods for the production of graphenes.* Nature Nanotechnology, 2009. **4**(4): p. 217-224.

238. M.J. Allen, V.C. Tung, R.B. Kaner, *Honeycomb carbon: A review of graphene.* Chemical Reviews, 2009. **110**(1): p. 132-145.

239. X. Li, W. Cai, J. An, S. Kim, J. Nah, D. Yang, R. Pine, A. Velamakanni, I. Jung, E. Tutuc, S. Banerjee, L. Colombo, R. Ruoff, *Large-area synthesis of high-quality and uniform graphene films on copper foils.* Science, 2009. **324**(5932): p. 1312-1314.

240. K.S. Kim, Y. Zhao,H. Jang, S.Y. Lee, J.M. Kim, K.S. Kim, J.H. Ahn, P. Kim, J.Y. Choi, B.H. Hong, *Large-scale pattern growth of graphene films for stretchable transparent electrodes.* Nature, 2009. **457**(7230): p. 706-710.

241. S. Mao, H. Pu, J. Chen, *Graphene oxide and its reduction: modeling and experimental progress.* RSC Advances, 2012. **2**(7): p. 2643-2662.

242. T. Kuila, A.K. Mishra, P. Khanra, N.H. Kim, J.H. Lee, *Recent advances in the efficient reduction of graphene oxide and its application as energy storage electrode materials.* Nanoscale, 2013. **5**(1): p. 52-71.

243. S. Pei, H.M. Cheng, *The reduction of graphene oxide.* Carbon, 2012. **50**(9): p. 3210-3228.

244. H. Bai, C. Li, X. Wang, G. Shi, *On the gelation of graphene oxide.* The Journal of Physical Chemistry C, 2011. **115**(13): p. 5545-5551.

245. H. Zheng, C.Y. Neo, X. Mei, J. Qiu, J. Ouyang, *Reduced graphene oxide films fabricated by gel coating and their application as platinum-free counter electrodes of highly efficient iodide/triiodide dye-sensitized solar cells.* J ials Chemistry, 2012. **22**(29): p. 14465-14474.

246. H.S. Jang, J.M. Yun, D.Y. Kim, D. W. Park, S.I. Na, S.S. Kim, *Moderately reduced graphene oxide as transparent counter electrodes for dye-sensitized solar cells.* Electrochimica Acta, 2012. **81**(0): p. 301-307.

247. G. Williams, B. Seger, P.V. Kamat, *TiO_2-graphene nanocomposites. UV-assisted photocatalytic reduction of graphene oxide.* ACS nano, 2008. **2**(7): p. 1487-1491.

248. C. Chen, M. Long, H. Wu, W. Cai, *One-step synthesis of Pt nanoparticles/reduced graphene oxide composite with enhanced electrochemical catalytic activity.* Science China Chemistry, 2013. **56**(3): p. 354-361.

249. H. Wang, Y.H. Hu, *Graphene as a counter electrode material for dye-sensitized solar cells.* Energy & Environmental Science, 2012. **5**(8): p. 8182-8188.

250. L.J. Brennan, M.T. Byrne, M. Bari, Y.K. Gun'ko, *Carbon nanomaterials for dye-sensitized solar cell applications: A bright future.* Advanced Energy Materials, 2011. **1**(4): p. 472-485.

251. I.V. Lightcap, P.V. Kamat, *Fortification of CdSe quantum dots with graphene Oxide. excited state interactions and light energy conversion.* Journal of the American Chemical Society, 2012. **134**(16): p. 7109-7116.

252. J.I. Paredes, S. Villar-Rodil, A. Martínez-Alonso, J.M. Tascón, *Graphene oxide dispersions in organic solvents.* Langmuir, 2008. **24**(19): p. 10560-10564.

253. F. Zhang, A. Petr, H. Peisert, M. Knupfer, L. Dunsch, *Electrochemical variation of the energy level of poly(3,4-ethylenedioxythiophene):Poly(styrenesulfonate).* The Journal of Physical Chemistry B, 2004. **108**(45): p. 17301-17305.

254. Y. Kim, S.A. Choulis, J. Nelson, D. Bradley, S. Cook, J. Durrant, *Device annealing effect in organic solar cells with blends of regioregular poly(3-hexylthiophene) and soluble fullerene.* Applied Physics Letters, 2005. **86**(6): p. 63502.

255. K. Lee, G.A. Sotzing, *Poly(thieno[3,4-b]thiophene). A new stable low band gap conducting polymer.* Macromolecules, 2001. **34**(17): p. 5746-5747.

256. I. Mc-Culloch, M. Heeney, C. Bailey, K. Genevicius, I. Macdonald, *Liquid-crystalline semiconducting polymers with high charge-carrier mobility.* Nature Materials, 2006. **5**(4): p. 328-333.

257. Y. Xia, L. Wang, X. Deng, D. Li, X. Zhu, Y. Cao, *Photocurrent response wavelength up to 1.1μm from photovoltaic cells based on narrow-bandgap conjugated polymer and fullerene derivative.* Applied Physics Letters, 2006. **89**(8): p. 81106.

258. P. Coppo, D. Cupertino, S. Yeates, M. Turner, *Synthetic routes to solution-processable polycyclopentadithiophenes.* macromolecules, 2003. **36**(8): p. 2705-2711.

259. J. Hou, H. Chen, S. Zhang, G. Li, Y. Yang, *Synthesis, characterization, and photovoltaic properties of a low band gap polymer based on silole-containing polythiophenes and 2,1,3-benzothiadiazole.* Journal of the American Chemical Society, 2008. **130**(48): p. 16144-16145.

260. S.H. Park, M. Leclerc, A.J. Heeger, K. Lee, *High efficiency polymer solar cells with internal quantum efficiency approaching 100%*. Organic Photovoltaics, 2009. **7416:** P. 825836.

261. D. Mühlbacher, M. Scharber, M. Morana, Z. Zhu, D. Waller, R. Gaudiana, C. Brabec, *High photovoltaic performance of a low-bandgap polymer.* Advanced Materials, 2006. **18**(21): p. 2884-2889.

262. L. Bozano, S. A. Carter, J.C. Scott, G.G. Malliaras, P. J. Brock, *Temperature- and field dependent electron and hole mobilities in polymer light-emitting diodes.* Applied Physics Letters, 1999. **74**(8): p. 1132-1134.

263. A. Babel, S.A. Jenekhe, *Electron transport in thin-film transistors from an n-type conjugated polymer.* Advanced Materials, 2002. **14**(5): p. 371-374.

264. Z. Bao, A. Dodabalapur, A. Lovinger, *Soluble and processable regioregular poly(3-hexylthiophene) for thin film field-effect transistor applications with high mobility.* Applied Physics Letters, 1996. **69**(26): p. 4108-4110.

265. R.J. Kline, M.D. McGehee, E.N. Kadnikova, J. Liu, J.M.J. Fréchet, *Controlling the field-effect mobility of regioregular polythiophene by changing the molecular weight.* Advanced Materials, 2003. **15**(18): p. 1519-1522.

266. S.M. Sze, *VLSI technology*, McGraw-Hill. 1988, New York.

267. H. Sirringhaus, N. Tessler, R. Friend, *Integrated optoelectronic devices based on conjugated polymers.* Science, 1998. **280**(5370): p. 1741-1744.

268. L. Groenendaal, F. Jonas, D. Freitag, H. Pielartzik, J. Reynolds, *Poly(3,4-ethylenedioxythiophene) and its derivatives: Past, present, and future.* Advanced Materials, 2000. **12**(7): p. 481-494.

269. S. Kirchmeyer, K. Reuter, *Scientific importance, properties and growing applications of poly(3,4-ethylenedioxythiophene).* Journal of Materials Chemistry, 2005. **15**(21): p. 2077-2088.

270. K.S. Kang, Y. Chen, H.K. Lim, K.Y. Cho, K.J. Han, J. Kim, *Performance enhancement of polymer Schottky diode by doping pentacene.* Thin Solid Films, 2009. **517**(21): p. 6096-6099.

271. B.V. Zeghbroeck, *Prinipiles of semiconductor devices, Chapter 2: Semiconductor fundamentals. Online textbook*, 2011.

272. L. Groenendaal, G. Zotti, P.H. Aubert, S.M. Waybrigh, J.R. Reynolds, *Electrochemistry of poly(3,4-alkylenedioxythiophene) derivatives.* Advanced Materials, 2003. **15**(11): p. 855-879.

273. C.J. Ko, Y.K. Lin, F.C. Chen, C.Y. Chu, *Modified buffer layers for polymer photovoltaic devices.* Applied Physics Letters, 2007. **90**(6): p. 63509.

274. M.M. de Kok, M. Buechel, S.I. Vulto, P. Van de Weijer, E.A. Meulenkamp, S.H. de Winter, A.J. Mank, H.J. Vorstenbosch, C.H. Weijtens, V. van Elsbergen, *Modification of PEDOT:PSS as hole injection layer in polymer LEDs.* physica status solidi (a), 2004. **201**(6): p. 1342-1359.

275. F. Verbakel, S.C.J. Meskers, R.A.J. Janssen, *Electronic memory effects in a sexithiophene−poly(ethylene oxide) block copolymer doped with NaCl. Combined diode and resistive switching behavior.* Chemistry of Materials, 2006. **18**(11): p. 2707-2712.

276. Meskers, S.C.J., J.K.J. van Duren, R.A.J. Janssen, F. Louwet, L. Groenendaal, *Infrared detectors with poly(3,4-ethylenedioxy thiophene)/poly(styrene sulfonic acid) (PEDOT/PSS) as the active material.* Advanced Materials, 2003. **15**(7-8): p. 613-616.

277. A. Kumar, D.M. Welsh, M.C. Morvant,F. Piroux, K.A. Abboud, J.R. Reynolds, *Conducting poly(3,4-alkylenedioxythiophene) derivatives as fast electrochromics with high-contrast ratios.* Chemistry of Materials, 1998. **10**(3): p. 896-902.

278. B. Yoo, A. Dodabalapur, D.C. Lee, T. Hanrath, B.A. Korgel, *Germanium nanowire transistors with ethylene glycol treated poly(3,4-ethylenedioxythiophene):poly(styrene sulfonate) contacts.* Applied Physics Letters, 2007. **90**(7): p. 72106.

279. B. Chen, T. Cui , Y. Liu, K. Varahramyan, *All-polymer RC filter circuits fabricated with inkjet printing technology.* Solid-State Electronics, 2003. **47**(5): p. 841-847.

280. F. Jonas, W. Krafft, B. Muys, *Poly(3, 4-ethylenedioxythiophene): Conductive coatings, technical applications and properties.* Macromolecular Symposia, 1995. **100**(1): p. 169-173.

281. J.C. Scott, C.G. Malliaras, W.D. Chen, J.C. Breach, J.R. Salem, P.J. Brock, S.B. Sachs, C.E. Chidsey et al., *Hole limited recombination in polymer light-emitting diodes.* Applied Physics Letters, 1999. **74**(11): p. 1510-1512.

282. G. Greczynski, T.H. Kugler, M. Keil, W. Osikowicz, M. Fahlman, W.R. Salaneck, *Photoelectron spectroscopy of thin films of PEDOT–PSS conjugated polymer blend: a mini-review and some new results.* Journal of Electron Spectroscopy and Related Phenomena, 2001. **121**(1–3): p. 1-17.

283. A.J. Mäkinen, I.G. Hill, R. Shashidhar, N. Nikolov, Z.H. Kafafi, *Hole injection barriers at polymer anode/small molecule interfaces.* Applied Physics Letters, 2001. **79**(5): p. 557-559.

284. N. Koch, A. Khan, J. Ghijsen, J.J. Pireaux, J. Schwartz, R.L. Johnson, A. Elschner, *Conjugated organic molecules on metal versus polymer electrodes: Demonstration of a key energy level alignment mechanism.* Applied Physics Letters, 2003. **82**(1): p. 70-72.

285. P.K.H. Ho, J.S. Kim, J.H. Burroughes, H. Becker, S.F. Li, T.M. Brown, F. Cacialli, R.H. Friend, *Molecular-scale interface engineering for polymer light-emitting diodes.* Nature, 2000. **404**(6777): p. 481-484.

286. H. Frohne, S. Shaheen, C. Brabec, D. Müller, N. Sariciftci, K. Meerholz, *Influence of the anodic work function on the performance of organic solar cells.* Physical Chemistry Chemical Physic**s**, 2002. **3**(9): p. 795-799.

287. D.C. Harris, *Quantitative chemical analysis*. 6th edition, ed. W. H. Freeman, Co. Gordonsville. 2003, USA.

288. Taylor and Francis Group, *Nanotechnology for photovoltaics, Chapter1: Introduction to photovoltaic physics, applications, and technologies,* ed. L. Tsakalakos, LLC Boca Raton London. 2010, New York.

289. L S. Bobrow, *Fundamentals of electrical engineering, Chapter 6: Diodes.* 2nd edition, Oxford Univesity Press. 1996, New York.

290. F.A. Lindholm, F.L. Gainesville, J.G. Fossum, E.L. Burgess, *Application of the superposition principle to solar-cell analysis.* IEEE Transactions on Electron Devices, 1979. **26**(3): p. 165-171.

291. P. Würfel, *Frontmatter*, in *physics of solar cells*, Wiley-VCH Verlag GmbH & Co. KGaA. 2007, Weinheim, Germany: p. I-XII.

292. M.A. Green, *Accuracy of analytical expressions for solar cell fill factors.* Solar Cells, 1982. **7**(3): p. 337-340.

293. Y. Liang, D. Feng, Y. Wu, S. Tsai, G. Li, C. Ray, L. Yu, *Highly efficient solar cell polymers developed via fine-tuning of structural and electronic properties.* Journal of the American Chemical Society, 2009. **131**(22): p. 7792-7799.

294. W.A. Tisdale, K. Williams, B. Timp, D. Norris, E. Aydil, X. Zhu, *Hot-electron transfer from semiconductor nanocrystals.* Science, 2010. **328**(5985): p. 1543-1547.

295. D. Timmerman, I. Izeddin, P. Stallinga, I.N. Yassievich, T. Gregorkiewicz, *Space-separated quantum cutting with silicon nanocrystals for photovoltaic applications.* Nature Photonics, 2008. **2**(2): p. 105-109.

296. D.J. Norris, A.L. Efros, S.C. Erwin, *Doped nanocrystals.* Science, 2008. **319**(5871): p. 1776-1779.

297. M.C. Beard, K. Knutsen, P. Yu, J. Luther, O. Song, W. Metzger, R. Ellingson, A. Nozik, *Multiple exciton generation in colloidal silicon nanocrystals.* Nano Letters, 2007. **7**(8): p. 2506-2512.

298. S. Emin, A. Loukanov, M. Wakasa, S. Nakabayash, Y. Kaneko, *Photostability of water-dispersible CdTe quantum dots: Capping ligands and oxygen.* Chemistry Letters, 2010. **39**(6): p. 654-656.

299. J.P. Clifford, K.W. Johnston, L. Levina, S.E. Sargent, *Schottky barriers to colloidal quantum dot films.* Applied Physics Letters, 2007. **91**(25): p. 253117.

300. J.D. Olson, Y.W. Rodriguez, L.D. Yang, G.B. Alers, S.A. Carter, *CdTe schottky diodes from colloidal nanocrystals.* Applied Physics Letters, 2010. **96**(24): p. 242103- 242106.

301. A.G. Pattantyus-Abrah am, I.J. Kramer, A.R. Barkhouse, X. Wang, G. Konstantatos, R. Debnath, L. Levina, I. Raabe, M.K. Nazeeruddin, M. Grätzel, E.H. Sargent, *Depleted-heterojunction colloidal quantum dot solar cells.* ACS Nano, 2010. **4**(6): p. 3374-3380.

302. R. Debnath, M. Greiner, I. Kramer, A. Fischer, J. Tang, D. Barkhouse, X. Wang, L. Levina, Z. Lu, E.H. Sargent, *Depleted-heterojunction colloidal quantum dot photovoltaics employing low-cost electrical contacts.* Applied Physics Letters, 2010. **97**(2): p. 23109.

303. S.R. Ferreira, R. Davis, Y. Lee, P. Lu, J. Hsu, *Effect of device architecture on hybrid zinc oxide nanoparticle:poly(3-hexylthiophene) blend solar cell performance and stability.* Organic Electronics, 2011. **12**(7): p. 1258-1263.

304. C.P. Liu, H.E. Wang, T.W. Ng, Z.H. Chen, W.F. Zhang, C. Yan, Y.B. Tang, I. Bello, L. Martinu, W.J. Zhang, S.K. Jha, *Hybrid photovoltaic cells based on ZnO/Sb_2S_3/P3HT heterojunctions.* physica status solidi (b), 2012. **249**(3): p. 627-633.

305. J.A. Chang, J.H. Rhee, S.H. Im, Y.H. Lee, H. Kim, S. Seok, M. Nazeeruddin, M. Gratzel, et al., *High-performance nanostructured inorganic−organic heterojunction solar cells.* Nano Letters, 2010. **10**(7): p. 2609-2612.

306. S.K. Dixit, S. Madan, D. Madhwal, J. Kumar, I. Singh, C.S. Bhatia, P.K. Bhatnagar, P.C. Mathur, *Bulk heterojunction formation with induced concentration gradient from a bilayer structure of P3HT:CdSe/ZnS quantum dots using inter-diffusion process for developing high efficiency solar cell.* Organic Electronics, 2012. **13**(4): p. 710-714.

307. X. Huang, S. Huang, Q. Zhang, X. Guo, D. Li, Y. Luo, Q. Shen, T. Toyodo, Q. Meng, *A flexible photoelectrode for CdS/CdSe quantum dot-sensitized solar cells (QDSSCs).* Chemical Communications, 2011. **47**(9): p. 2664-2666.

308. P.V. Kamat, *Boosting the efficiency of quantum dot sensitized solar cells through modulation of interfacial charge transfer.* Accounts of Chemical Research, 2012. **45**(11): p. 1906-1915.

309. J.M. Luther, M. Law, M. Beard, Q. Song, M. Reese, R. Ellingson, A. Nozi, *Schottky solar cells based on colloidal nanocrystal films.* Nano Letters, 2008. **8**(10): p. 3488-3492.

310. A.J. Said, G. Poize, C. Martini, D. Ferry, W. Marine, S. Giorgio, F. Fages, J. Hocq, J. Bouclé, J. Nelson, J. R. Durrant, J. Ackermann, *Hybrid bulk heterojunction solar cells based on P3HT and porphyrin-modified ZnO nanorods.* Journal of Physical Chemistry C, 2010. **114**(25): p. 11273-11278.

311. H. Liu, J. Tang, I. Kramer, R. Debnath, G. Koleilat, X. Wang, A. Fisher, R. Li, L. Brzozowski, L. Levina, E.H. Sargent, *Electron acceptor materials engineering in colloidal quantum dot solar cells.* Advanced Materials, 2011. **23**(33): p. 3832-3837.

312. S. Ren, L.Y. Chang, S.K. Lim, J. Zhao, M. Smith, N. Zhao, V. Bulović, M. Bawendi, S. Gradecak, *Inorganic-organic hybrid solar cell: Bridging quantum dots to conjugated polymer nanowires.* Nano Letters, 2011. **11**(9): p. 3998-4002.

313. Y. Zhou, M. Eck, C. Veit, B. Zimmermann, F. Rauscher, P. Niyamakom, S. Yilmaz, I. Dumsch, S. Allard, U. Scherf, M. Krüg, *Efficiency enhancement for bulk-heterojunction hybrid solar cells based on acid treated CdSe quantum dots and low bandgap polymer PCPDTBT.* Solar Energy Materials and Solar Cells, 2011. **95**(4): p. 1232-1237.

314. D. Celik, M. Krueger, C. Veit, H. Schleiermacher, B. Zimmermann, S. Allard, I. Dumsch, U. Scherf, F. Rauscher, P. Niyamakom, *Performance enhancement of CdSe nanorod-polymer based hybrid solar cells utilizing a novel combination of post-synthetic nanoparticle surface treatments.* Solar Energy Materials and Solar Cells, 2012. **98**(0): p. 433-440.

315. N. Nicolaidis, B. Routley, J. Holdsworth, W. Belcher, X. Zhou, P. Dastoor, *Fullerene Contribution to photocurrent generation in organic photovoltaic cells.* The Journal of Physical Chemistry C, 2011. **115**(15): p. 7801-7805.

316. T. Takagahara, K. Takeda, *Theory of the quantum confinement effect on excitons in quantum dots of indirect-gap materials.* Physical Review B, 1992. **46**(23): p. 15578-15581.

317. J. Huang, Z. Huang, Y. Yang, H. Zhu, T. Lian, *Multiple exciton dissociation in CdSe quantum dots by ultrafast electron transfer to a dsorbed methylene blue.* Journal of the American Chemical Society, 2010. **132**(13): p. 4858-4864.

318. I. Gonzalez-Valls, M. Lira-Cantu, *Vertically-aligned nanostructures of ZnO for excitonic solar cells: a review.* Energy & Environmental Science, 2009. **2**(1): p. 19-34.

319. M. Wright, A. Uddin, *Organic-inorganic hybrid solar cells: A comparative review.* Solar Energy Materials and Solar Cells, 2012. **107**(0): p. 87-111.

320. B. O'Regan, M. Gratzel, *A low-cost, high-efficiency solar cell based on dye-sensitized colloidal TiO2 films.* Nature, 1991. **353**(6346): p. 737-740.

321. T. Stergiopoulos, E. Rozi, C. Karagianni, P. Falaras, *Influence of electrolyte co-additives on the performance of dye-sensitized solar cells.* Nanoscale Research Letters, 2011. **6**(1): p. 1-7.

322. M. Zukalová, A. Zukal, L. Kavan, M.K. Nazeeruddin, P. Liska, M. Grätzel, *Organized mesoporous* TiO_2 *films exhibiting greatly enhanced performance in dye-sensitized solar cells.* Nano Letters, 2005. **5**(9): p. 1789-1792.

323. J. Yu, D. Wang, Y. Huang, X. Fan, X. Tang, C. Gao**,** J. Li, D. Zou, K. Wu, *A cylindrical core-shell-like* TiO_2 *nanotube array anode for flexible fiber-type dye-sensitized solar cells*. Nanoscale Research Letters, 2011. **6**(1) : p. 94.

324. C. Wang, Z. Jiang, L. Wei, Y. Chen, J. Jiao, M. Eastman, H. Liu, *Photosensitization of* TiO_2 *nanorods with CdS quantum dots for photovoltaic applications: A wet-chemical approach.* Nano Energy, 2012. **1**(3): p. 440-447.

325. L.J. Diguna, S. Qing, J. Kobayashi, T. Toyoda, *High efficiency of CdSe quantum-dot-sensitized* TiO_2 *inverse opal solar cells.* A pplied Physics Letters, 2007. **91**(2): p. 23116.

326. M. Nanu, J. Schoonman, A. Goossens, *Nanocomposite three-dimensional solar cells obtained by chemical spray deposition.* Nano Letters, 2005. **5**(9): p. 1716-1719.

327. Y. Itzhaik, O. Niitsoo, M. Page, G. Hodes, Sb_2S_3*-sensitized nanoporous* TiO_2 *solar cells.* The Journal of Physical Chemistry C, 2009. **113**(11): p. 4254-4256.

328. M. Sun, G. Chen, Y. Zhang, Q. Wei, Z. Ma, and B. Du, et al., *Efficient degradation of Azo dyes over* Sb_2S_3/TiO_2 *heterojunction under visible light irradiation.* Industrial & Engineering Chemistry Research, 2011. **51**(7): p. 2897-2903.

329. A. Braga, S. Giménez, I. Concina, A. Vomiero, I. Mora-Seró, *Panchromatic sensitized solar cells based on metal sulfide quantum dots grown directly on nanostructured* TiO_2 *electrodes.* The Journal of Physical Chemistry Letters, 2011. **2**(5): p. 454-460.

330. J.H. Im, C.R. Lee, J.W. Lee, S.W. Park, N.G. Park, *6.5% efficient perovskite quantum-dot-sensitized solar cell.* Nanoscale, 2011. **3**(10): p. 4088-4093.

331. H. Lee, H. Leventis, S. Moon, P. Chen, S. Haque, T. Torres, F. Nüesch, T. Geiger, S. Zakeeruddin, M. Grätzel, M. Nazeeruddin, *PbS and CdS quantum dot-sensitized solid-state solar cells: "old concepts, new results".* Advanced Functional Materials, 2009. **19**(17): p. 2735-2742.

332. I.J. Kramer, L. Levina, R. Debnath, D. Zhitomirsky, E.H. Sargent, *Solar cells using quantum funnels.* Nano Letters, 2011. **11**(9): p. 3701-3706.

333. J. Tang, H. Liu, D. Zhitomirsky, S. Hoogland, X. Wang, M. Furukawa, L. Levina, E.H. Sargent, *Quantum junction solar cells.* Nano Letters, 2012. **12**(9): p. 4889-4894.

334. B. Gonfa, H. Zhao, J. Li, J. Qiu, M. Saidani, S. Zhang, R. Izquierdo, N. Wu, A. Khakani, D. Ma, *Air-processed depleted bulk heterojunction solar cells based on PbS/CdS core–shell quantum dots and* TiO_2 *nanorod arrays.* Solar Energy Materials and Solar Cells, 2014. **124**(0): p. 67-74.

335. L.Y. Chang, R. Lunt, P. Brown, V. Bulović, M. Bawendi, *Low-temperature solution-processed solar cells based on PbS colloidal quantum dot/CdS heterojunctions.* Nano Letters, 2013. **13**(3): p. 994-999.

336. K. Bhandari, P. Roland, H. Mahabaduge, N. Haugen, C. Grice, S. Jeong, T. Dykstra, J. Gao, R. Ellingson, *Thin film solar cells based on the heterojunction of colloidal PbS quantum dots with CdS.* Solar Energy Materials and Solar Cells, 2013. **117**(0): p. 476-482.

337. A.K. Rath, M. Bernechea, L. Martinez, G. Konstantatos, *Solution-processed heterojunction solar cells based on p-type PbS quantum dots and n-type* Bi_2S_3 *nanocrystals.* Advanced Materials, 2011. **23**(32): p. 3712-3717.

338. K.S. Leschkies, T.J. Beatty, M.S. Kang, D.J. Norris, E.S. Aydil, *Solar cells based on junctions between colloidal PbSe nanocrystals and thin ZnO films.* ACS nano, 2009. **3**(11): p. 3638-3648.

339. A. Stavrinadis, J. Smith, C. Cattley, A. Cook, P. Grant, A. Watt, *SnS/PbS nanocrystal heterojunction photovoltaics.* Nanotechnology, 2010. **21**(18): p. 185202.

340. G.H. Kim, B. Walker, H.B. Kim, J.Y. Kim, E.H. Sargent, J. Park, J.Y. Kim, *Inverted colloidal quantum dot solar cells.* Advanced Materials, 2014. **26**(20): p. 3321-3327.

341. J. Chen, C. Cheng, W. Chiu, C. Lee, N. Liang, *Synthesis of ZnO/polystyrene composites particles by Pickering emulsion polymerization.* European Polymer Journal, 2008. **44**(10): p. 3271-3279.

342. E. Hosono, S. Fujihara, T. Kimura, H. Imai, *Non-basic solution routes to prepare ZnO nanoparticles.* Journal of Sol-Gel Science and Technology, 2004. **29**(2): p. 71-79.

343. C.C. Li, M.H. Chang, *Colloidal stability of CuO nanoparticles in alkanes via oleate modifications.* Materials Letters, 2004. **58**(30): p. 3903-3907.

344. R.V. Kumar, Y. Diamant, A. Gedanken, *Sonochemical synthesis and characterization of nanometer-size transition metal oxides from metal acetates.* Chemistry of Materials, 2000. **12**(8): p. 2301-2305.

345. G. Eda, C. Mattevi, H. Yamaguchi, *Insulator to semimetal transition in graphene oxide.* The Journal of Physical Chemistry C, 2009. **113**(35): p. 15768-15771.

346. I. Jung, D.A. Dikin, R.D. Piner, R.S. Ruoff, *Tunable electrical conductivity of individual graphene oxide sheets reduced at "low" temperatures.* Nano Letters, 2008. **8**(12): p. 4283-4287.

347. J.M. Yun, J. Yeo, J. Kim, H. Jeong, D. Y. Kim, Y.J. Noh, S.S. Kim, B.C. Ku, S.I. Na, *Organic solar cells: Solution-processable reduced graphene oxide as a novel alternative to PEDOT:PSS hole transport layers for highly efficient and stable polymer solar cells.* Advanced Materials, 2011. **23**(42): p. 4819-4819.

348. X. Li, H. Wang, J. Robinson, H. Sanchez, G. Diankov, H. Dai, *Simultaneous nitrogen doping and reduction of graphene oxide.* Journal of the American Chemical Society, 2009. **131**(43): p. 15939-15944.

349. M.J. McAllister, J.L. Li, D. Adamson, H. Schniepp, A. Abdala, J. Liu, M. Alonso, D. Milius, R. Car, R. Prud'homme, I. Aksay, *Single sheet functionalized graphene by oxidation and thermal expansion of graphite.* Chemistry of Materials, 2007. **19**(18): p. 4396-4404.

350. Y.J. Jeon, J. Yun, D.Y. Kim, S. Na, S.S. Kim, *High-performance polymer solar cells with moderately reduced graphene oxide as an efficient hole transporting layer.* Solar Energy Materials and Solar Cells, 2012. **105**(0): p. 96-102.

351. K. Szendrei, W. Gomulya, M. Yarema, W. Heiss, M.A. Loi, *PbS nanocrystal solar cells with high efficiency and fill factor.* Applied Physics Letters, 2010. **97**(20): p. 203501.

352. C. Ratanatawanate, C.R. Xiong, K.J. Balkus, *Fabrication of PbS Quantum Dot Doped TiO_2 Nanotubes.* ACS Nano, 2008. **2**(8): p. 1682-1688.

353. T. Kawano, H. Imai, *A simple preparation technique for shape-controlled zinc oxide nanoparticles: Formation of narrow size-distributed nanorods using seeds in aqueous solutions.*Colloids and Surfaces A: Physicochemical and Engineering Aspects, 2008. **319**(1–3): p. 130-135.

354. B. Liu, H.C. Zeng, *Room temperature solution synthesis of monodispersed single-crystalline ZnO nanorods and derived hierarchical nanostructures.* Langmuir, 2004. **20**(10): p. 4196-4204.

355. P. Li, Y. Wei, H. Liu, X. Wang, *A simple low-temperature growth of ZnO nanowhiskers directly from aqueous solution containing Zn(OH)42- ions.* Chemical Communications, 2004(24): p. 2856-2857.

356. E.M. Wong, P.C. Searson, *ZnO quantum particle thin films fabricated by electrophoretic deposition.* Applied Physics Letters, 1999. **74**(20): p. 2939-2941.

357. A.K. Singh, *Synthesis, characterization, electrical and sensing properties of ZnO nanoparticles.* Advanced Powder Technology, 2010. **21**(6): p. 609-613.

358. D.H. Zhang, Z.Y. Xue, Q.P. Wang, *The mechanisms of blue emission from ZnO films deposited on glass substrate by r.f. magnetron sputtering.* Journal of Physics D: Applied Physics, 2002. **35**(21): p. 2837.

359. L.E. Brus, *Electron–electron and electron-hole interactions in small semiconductor crystallites: The size dependence of the lowest excited electronic state.* The Journal of Chemical Physics, 1984. **80**(9): p. 4403-4409.

360. *Phosphor handbook.* 2nd edition, ed. W.Y. Yen, S. Shionoya, H. Yamamoto. FL, CRC Press, 1998, Boca Raton.

361. B. Cao, W. Cai, H. Zeng, *Temperature-dependent shifts of three emission bands for ZnO nanoneedle arrays.* Applied physics letters, 2006. **88**(16): p. 161101-161104.

362. K. Lin, H. Cheng, H. Hsu, L. Lin, W. Hsieh, *Band gap variation of size-controlled ZnO quantum dots synthesized by sol–gel method.* Chemical Physics Letters, 2005. **409**(4): p. 208-211.

363. X.Q. Wei, B.Y. Man, M. Liue, C.S. Xue, H.Z. Zhuang, C. Yang, *Blue luminescent centers and microstructural evaluation by XPS and Raman in ZnO thin films annealed in vacuum, N_2 and O_2.* Physica B: Condensed Matter, 2007. **388**(1–2): p. 145-152.

364. A.B. Djurišić, Y.H. Leung, K.H. Tam, Y.F. Hsu, L. Ding, W.K. Ge, Y.C. Zhong, K.S. Wong, W.K. Chan, H.L. Tam, K.W. Cheah, W.M. Kwok, D.L. Phillips, *Defect emissions in ZnO nanostructures.* Nanotechnology, 2007. **18**(9): p. 095702.

365. K.H. Tam, C.K Cheung, Y.H. Leung, A.B. Djurisić, C.C. Ling, C.D. Beling, S. Fung, W.M. Kwok, W.K. Chan, D.L. Phillips, L. Ding, W.K. Ge, *Defects in ZnO nanorods prepared by a hydrothermal method.* The Journal of Physical Chemistry B, 2006. **110**(42): p. 20865-20871.

366. Q.X. Zhao, P. Klason, M. Willander, H.M. Zhong, W. Lu, J.H. Yang, *Deep-level emissions influenced by O and Zn implantations in ZnO.* Applied Physics Letters, 2005. **87**(21): p. 211912.

367. S. Yamauchi, Y. Goto, T. Hariu, *Photoluminescence studies of undoped and nitrogen-doped ZnO layers grown by plasma-assisted epitaxy.* Journal of Crystal Growth, 2004. **260**(1): p. 1-6.

368. S.H. Jeong, B.S. kim, B.T. Lee, *Photoluminescence dependence of ZnO films grown on Si(100) by radio-frequency magnetron sputtering on the growth ambient.* Applied Physics Letters, 2003. **82**(16): p. 2625-2627.

369. *Wikipedia, the free encyclopedia:* http://en.wikipedia.org/wiki/ Main Page.

370. N. Zhao, L. Qi, *Low-temperature synthesis of star-shaped PbS nanocrystals in aqueous solutions of mixed cationic/anionic surfactants.* Advanced Materials, 2006. **18**(3): p. 359-362.

371. S. Tsunekawa, T. Fukuda, A. Kasuya, *Blue shift in ultraviolet absorption spectra of monodisperse* CeO_{2-x} *nanoparticles.* Journal of Applied Physics, 2000. **87**(3): p. 1318-1321.

372. L.H.J. Lajunen, P. Perämäki, Spectrochemical analysis by *absorption and emission*. 2nd edition**,** Royal Society of Chemistry. 2004, Cambridge, UK: p. 332-342.

373. K. Borgohain, S. Mahamuni, *Formation of single-phase CuO quantum particles.* Journal of Materials Research, 2002. **17**(5): p. 1220-1223.

374. F.P. Koffyberg, F.A. Benko, *A photoelectrochemical determination of the position of the conduction and valence band edges of p-type CuO.* Journal of Applied Physics, 1982. **53**(2): p. 1173-1177.

375. L.S. Lanje**,** S. Sharma, R. Pode, R. Ningthoujam, *Synthesis and optical characterization of copper oxide nanoparticles.* Advances in Applied Science Research, 2010. **1**(2): p. 36-40.

376. J.R. Gispert, *Coordination chemistry*. 1st edition, Wiley-VCH. 2008, Weinheim.

377. G. Maglia, A. Jonckheer, M. Maeyer, J. Frère, Y. Engelborghs, *An unusual red-edge excitation and time-dependent Stokes shift in the single tryptophan mutant protein DD-carboxypeptidase from Streptomyces: The role of dynamics and tryptophan rotamers.* Protein Science, 2008. **17**(2): p. 352-361.

378. A.P. Demchenko, *Chapter 4 site-selective red-edge effects*, in *methods in enzymology*, ed. B. Ludwig and L.J. Michael. 2008, Academic Press. p. 59-78.

379. K. Das, S.K. De, *Optical and photoconductivity studies of* Cu_2O *nanowires synthesized by solvothermal method.* Journal of Luminescence, 2009. **129**(9): p. 1015-1022.

380. N. Tit, Z.H. Yamani, J. Graham, A. Ayesh, *Origins of visible-light emissions in hydrogen-coated silicon nanocrystals: Role of passivating coating.* Journal of Luminescence, 2010. **130**(11): p. 2226-2237.

381. L. Irimpan, B. Krishnan, A. Deepthy, V.P.N. Nampoori, P. Radhakrishnan, *Excitation wavelength dependent fluorescence behaviour of nano colloids of ZnO.* Journal of Physics D-applied Physics, 2007. **40**(18): p. 5670-5674.

382. S. Mathew, S. Ani Joseph, P. Radhakrishnan, V.P. Nampoori, C.P. Vallabhan, *Shifting of fluorescence peak in CdS nanoparticles by excitation wavelength change.* Journal of Fluorescence, 2011. **21**(4): p. 1479-1484.

383. I.H.J. Arellano, J. Mangadlao, I.B. Ramiro, K.F. Suazo, *3-component low temperature solvothermal synthesis of colloidal cadmium sulfide quantum dots.* Materials Letters, 2010. **64**(6): p. 785-788.